Assessment and Optimisation of Target Acquisition using SAR Seekers on Manoeuvrable Re-Entry Vehicles

MSc Thesis

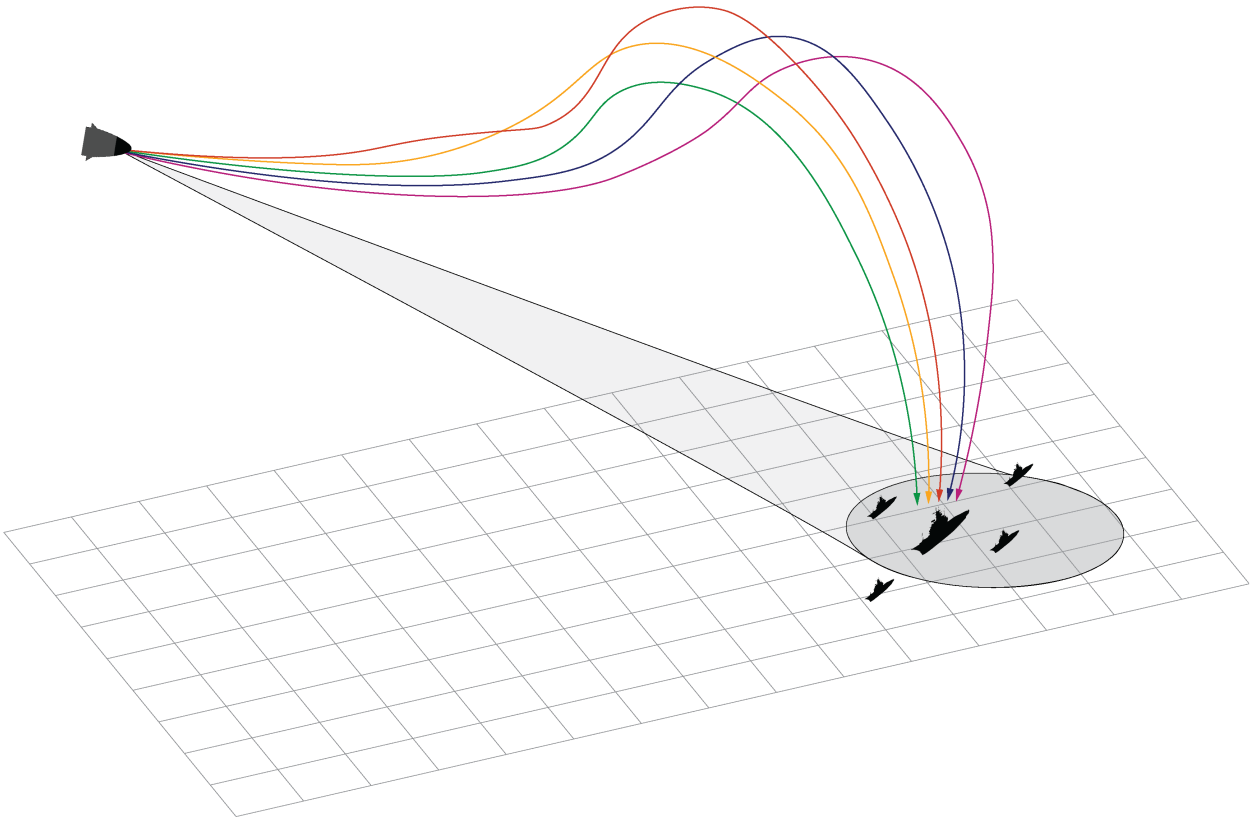

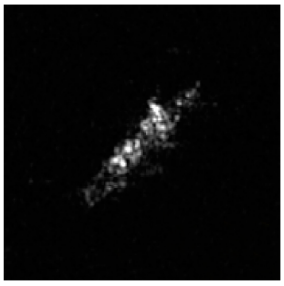

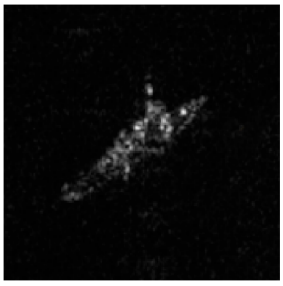

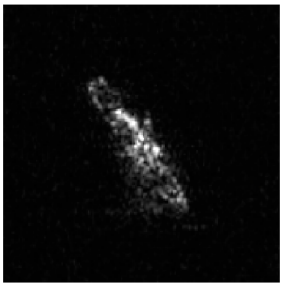

E.R. Olberts - 4736079

February 2022

Delft University Of Technology
TNO Defence, Safety and Security

TU Delft Delft University of Technology

TNO innovation for life

Assessment and Optimisation of Target Acquisition using SAR Seekers on Manoeuvrable Re-Entry Vehicles

by

E.R. Olberts

to obtain the degree of Master of Science
at the Delft University of Technology,
to be defended publicly on Friday February 25, 2022 at 10:00 AM.

Student number:	4736079	
Project duration:	March 1, 2021 - December 1, 2021	
Thesis committee:	Dr. Ir. W. van der Wal,	TU Delft, chair
	Dr. Ir. M. Snellen	TU Delft, examiner
	Ir. M.C. Naeije,	TU Delft, supervisor
	Ir. W.H.C. Halswijk,	TNO, supervisor
	Ir. M.J.C. Heiligers,	TNO, supervisor

An electronic version of this thesis is available at `http://repository.tudelft.nl/`.

Abstract

In this project, the achievable performance and limitations of a Synthetic Aperture Radar (SAR) seeker on an Anti-Ship Ballistic Missile (ASBM) for a set of parameters has been investigated. This was achieved by modelling the dynamics of an ASBM and the constraints related to the acquisition requirements of a maritime surface target in the "Generation and Improvement Algorithm for Nonlinear Trajectories" (GIANT) optimisation tool provided by TNO. The angular velocities of the ASBM were set as the control variables for the optimal control problem where the objectives were set to the minimisation and maximisation of the exposure time and vertical end velocity of the missile and the minimisation of the required time for creating one SAR image by the SAR seeker.

Three experiments were carried out to investigate the influences for different initial conditions and resolution constraints on the optimised trajectory. In the first experiment, the trajectory was optimised for initial re-entry conditions that are representative for typical ASBMs. The target was placed at the location that would match the uncorrected ballistic flight impact location of the ASBM. This allowed to compare and visualise the optimised manoeuvres of the ASBM relative to its ballistic flight trajectory. In the second experiment, the target was placed at the same location, but the initial re-entry conditions were optimised by GIANT, that provided the optimal trajectory. In the last experiment, the constraints related to the resolution of the target were lowered to analyse the maximum performance of the system.

The experiments show that a larger initial squint angle of the re-entry position of the ASBM improves the overall performance. This is because a larger squint angle allowed the missile to obtain a larger seeker look angle during the SAR phase while performing minimal manoeuvres during the re-entry phase. This permitted the dwell time of the SAR seeker and the exposure time of the missile to be as short as possible, while the missile's vertical end velocity could be maximised. It was also shown that a ground range and crossrange resolution of 1.60 m could be achieved for an average dwell time of 0.1170 s. For better resolutions, the bandwidth of the SAR seeker appeared to be the limiting factor of the system for the chosen set of parameters.

Preface

I always have been fascinated by computer simulations and flight mechanics. In addition, I also wanted to learn more about radar systems and their applications. This convinced me to dedicate my thesis to one or both of these topics. I was fortunate that TNO was able to offer me this specific project that matched my interests.

At the start of the project most of the topics were completely new to me. This, in combination with working from home for the majority of time due to the Covid-19 pandemic, made the project very challenging. Nonetheless, the past year has been very informative and I am grateful to TNO for providing me this opportunity. Besides getting acquainted with the disciplines, work atmosphere and people at TNO, I also have developed many personal skills that would help me to pursue my future career.

Accordingly, I would like to thank several people for making this possible. First of all, I would like to thank my supervisors Wouter Halswijk and Matijs Heiligers for their support, feedback and guidance during the project. Furthermore, I would like to thank my TU Delft supervisor Marc Naeije for his support, feedback and his full understanding and empathy for the challenges I have encountered during the project. A special thanks to my temporary colleague Michiel Bergsma for his availability, help and suggestions during my project. Finally, I would like to thank my brother for his feedback on this paper.

E.R. Olberts
Delft, February 2022

Contents

List of Tables

List of Figures

List of Abbreviations

ASBM	Anti-Ship Ballistic Missile
BVP	Boundary-Value Problem
CG	Center Of Gravity
CNR	Clutter-to-Noise Ratio
CPI	Coherent Processing Interval
DCM	Direction Cosine Matrix
FNBW	First Null Beam Width
GIANT	Generation and Improvement Algorithm for Nonlinear Trajectories
HPBW	Half Power Beam Width
ISR	Intelligence, Surveillance and Reconnaissance
LFM	Linear Frequency Modulation
LOS	Line-Of-Sight
NLP	Nonlinear Programming
NRL	Naval Research Laboratory
OCP	Optimal Control Problem
PRF	Pulse Repetition Frequency
PRI	Pulse Repetition Interval
RCS	Radar Cross Section
SAR	Synthetic Aperture Radar
SCR	Signal-to-Clutter Ratio
SNR	Signal-to-Noise Ratio
SQP	Sequential Quadratic Programming

List of Symbols

Latin Symbol	Definition	Unit
A	Cross sectional area of the missile	m^2
A_a	Physical area of the antenna	m^2
a_D	Drag acceleration	m/s^2
A_e	Effective area of the antenna	m^2
a_L	Lift acceleration	m/s^2
A_t	The area of the target	m^2
BC_0	Ballistic coefficient at a zero angle-of-attack	rad/deg
B	Bandwidth	Hz
B_D	Doppler bandwidth	Hz
C	Quaternion rotation matrix	-
c	Speed of light	m/s
C_D	Drag coefficient	-
C_L	Lift coefficient	-
C_{D_0}	Zero-Lift drag coefficient	-
C_{L_α}	Lift coefficient w.r.t. the angle-of-attack	-
DT	Dwell Time	s
D	Full displacement of maritime surface target	kton
d_c	Duty cycle	%
f_c	Center operating frequency	Hz
f_D	Doppler shift	Hz
F_D	Drag force	N
F_L	Lift force	N
F_n	Noise figure	dB
F_{g_0}	Gravitational force	N
$\mathscr{F}_b$	Body fixed frame	-
$\mathscr{F}_n$	Local North-East-Down (NED) frame	-
$\mathscr{F}_s$	Line-Of-Sight (LOS) frame	-
$\mathscr{F}_t$	Trajectory frame	-
$\mathscr{F}_{nv}$	Vehicle-carried NED frame	-
G	Antenna gain	dB
g_0	Gravitational acceleration at sea level	m/s^2
G_a	Crossrange processing gain	dB
G_r	Range processing gain	dB
k_B	Boltzmann constant	m^2kg/s^2K
l_a	Physical length/width of the antenna	m
L_{atmos}	Atmospheric loss factor	dB
L_a	Reduction in gain due to non-ideal crossrange filtering	dB
L_{radar}	Radar loss factor	dB

L_r	Reduction in gain due to non-ideal range filtering	dB
m	Mass of the missile	kg
N	Total amount of pulses	-
N_L	Lift acceleration vector	-
PRF	Pulse Repetition Frequency	Hz
PRF_{nadir}	Pulse Repetition Frequency to avoid echoes originating from the nadir	Hz
PRF_{max}	Maximum Pulse-Repetition-Frequency	Hz
PRF_{min}	Minimum Pulse-Repetition-Frequency	Hz
p	Roll rate	rad/s
P_p	Peak transmitted power	W
P_r	Received power by the antenna from the target	W
$P_{\text{r,clutter}}$	Received power by the antenna from the sea clutter	W
$\overline{P}$	Average transmitted power	W/s
q	Pitch rate	rad/s
R	Distance from antenna to point target	m
r	Yaw Rate	rad/s
r_{search}	Search area radius	m
$R_{\text{max}}^{\text{0dB}}$	Maximum range to the edge of the 0dB beam footprint	m
$R_{\text{min}}^{\text{0dB}}$	Minimum range to the edge of the 0dB beam footprint	m
$R_{\text{max}}^{\text{-3dB}}$	Maximum range to the edge of the -3dB beam footprint	m
$R_{\text{min}}^{\text{-3dB}}$	Minimum range to the edge of the -3dB beam footprint	m
R_g	Ground range between the missile and target	m
R_s	Slant range between the missile and target	m
R_x	Distance to target in x-direction	m
R_y	Distance to target in y-direction	m
R_z	Distance to target in z-direction	m
$R_{(3)\rightarrow(4)}$	Range between third and fourth boundary	-
SCR	Signal-To-Clutter Ratio	dB
SNR	Signal-To-Noise Ratio	dB
SS	Sea state	dB
t	Time	s
t_{TOF}	Time Of Flight	s
T	Pulse Repetition Interval	Hz
T_0	Nominal reference temperature	K
$T_{(2)\rightarrow(3)}$	Time between second and third boundary	-
$\vec{u}_{LOS}$	Unit Line-Of-Sight Vector	s
$\vec{u}_v$	Unit Velocity Vector	-
V	Missile Velocity	m/s
x_m	Missile coordinate in North-direction	m
x_t	Target coordinate in North-direction	m
x_{bx}	Unit vector of x_b in x_{nv} direction	-
x_{by}	Unit vector of x_b in y_{nv} direction	-
x_{bz}	Unit vector of x_b in z_{nv} direction	-
y_m	Missile coordinate in East-direction	m
y_t	Target coordinate in East-direction	m
y_{bx}	Unit vector of y_b in x_{nv} direction	-
y_{by}	Unit vector of y_b in y_{nv} direction	-

y_{bz}	Unit vector of y_b in z_{nv} direction	-
z_m	Missile coordinate in Down-direction	m
z_t	Target coordinate in Down-direction	m
z_{bx}	Unit vector of z_b in x_{nv} direction	-
z_{by}	Unit vector of z_b in y_{nv} direction	-
z_{bz}	Unit vector of z_b in z_{nv} direction	-

Greek Symbol	Definition	Unit
α	Angle-of-attack	rad/deg
$\beta_{-3\text{dB}}$	-3dB beamwidth	rad/deg
$\beta_{0\text{dB}}$	0dB beamwidth	rad/deg
γ	Flight path angle	rad/deg
Γ_{DT}	Scaling factor for the dwell time	-
Γ_{pqr}	Scaling factor for the angular velocities	-
$\Gamma_{t_{\text{end}}}$	Scaling factor for exposure time	-
$\Gamma_{V_{\text{D,end}}}$	Scaling factor for vertical end velocity	-
ζ	Seeker look angle	rad/deg
η_{ap}	Aperture efficiency of the antenna	%
θ	Pitch angle	rad/deg
θ_{sq}	Squint angle	rad/deg
λ_c	Center operating wavelength	m
Λ	Vertical angle between $\vec{u}_v$ and $\vec{u}_{LOS}$	rad/deg
Ξ	Horizontal angle between $\vec{u}_v$ and $\vec{u}_{LOS}$	rad/deg
ρ	Atmospheric density	kg/m^3
$\rho_{\text{cr,max}}^{\text{-3dB}}$	Maximum crossrange resolution within the -3dB beam footprint	m
$\rho_{\text{gr,max}}^{\text{-3dB}}$	Maximum ground range resolution within the -3dB beam footprint	m
ρ_{cr}	Crossrange resolution	m
$\rho_{cr}^{270°}$	Approximation worst crossrange resolution in search area	m
$\rho_{cr}^{90°}$	Approximation best crossrange resolution in search area	m
ρ_{cr}^{BS}	Crossrange resolution at boresight	m
ρ_{f_D}	Doppler resolution	m
ρ_{gr}	Ground range resolution	m
$\rho_{gr}^{0°}$	Approximation best ground range resolution in search area	m
$\rho_{gr}^{180°}$	Approximation worst ground range resolution in search area	m
ρ_{gr}^{BS}	Ground range resolution at boresight	m
σ_c^0	Normalised sea clutter Radar-Cross-Section	dBm^2/m^2
$\sigma_{\text{c,max}}$	Maximum received normalised sea clutter Radar-Cross-Section	dBm^2/m^2
σ_t	Total target Radar-Cross-Section	dBm^2
σ_t^0	Normalised target Radar-Cross-Section per m^2	dBm^2/m^2
τ	Pulse width	s
τ_c	Compressed pulse width	s
ϕ	Roll angle	rad/deg
Φ	Lagrange term in cost function	-
χ	Heading angle	rad/deg
ψ	Yaw angle	rad/deg
$\psi_{\text{g,max}}^{\text{-3dB}}$	Maximum grazing angle of the -3dB beam footprint	rad/deg

$\psi_{g,min}^{-3dB}$	Minimum grazing angle of the -3dB beam footprint	rad/deg
$\psi_{g,max}^{0dB}$	Maximum grazing angle of the 0dB beam footprint	rad/deg
$\psi_{g,min}^{0dB}$	Minimum grazing angle of the 0dB beam footprint	rad/deg
ψ_g	Squint angle	rad/deg
Ψ	Mayer term in cost function	-
Ω	Total angle between $\vec{u}_v$ and $\vec{u}_{LOS}$	rad/deg

Subscript	Definition	Unit
0	Initial	-

1

Introduction

This research is designed and conducted in collaboration with the Weapon Systems and Radar Technology departments at TNO Defence, Safety and Security. The results of this research will provide TNO an insight of the capabilities of Synthetic Aperture Radar (SAR) seekers on ASBMs. Follow-up investigations may eventually lead to the development of appropriate defence systems.

1.1. Project Motivation

An Anti-Ship Ballistic Missile (ASBM) is a military ballistic missile that is used to destroy a moving maritime surface target. Like traditional ballistic missiles, an ASBM has an initial powered boost phase which is followed by a ballistic trajectory to a predetermined area. However, because a maritime surface target is moving and generally accompanied by other ships forming a naval fleet, an ASBM requires manoeuvrability, target acquisition and terminal guidance as illustrated in Figure 1.1.

The manoeuvrability of an ASBM can be controlled by its aerodynamic flaps, while the terminal guidance can be achieved by a radar homing system. The target acquisition is generally provided by other military vehicles such as satellites, unmanned aircraft or aircraft systems, usually referred as Intelligence, Surveillance and

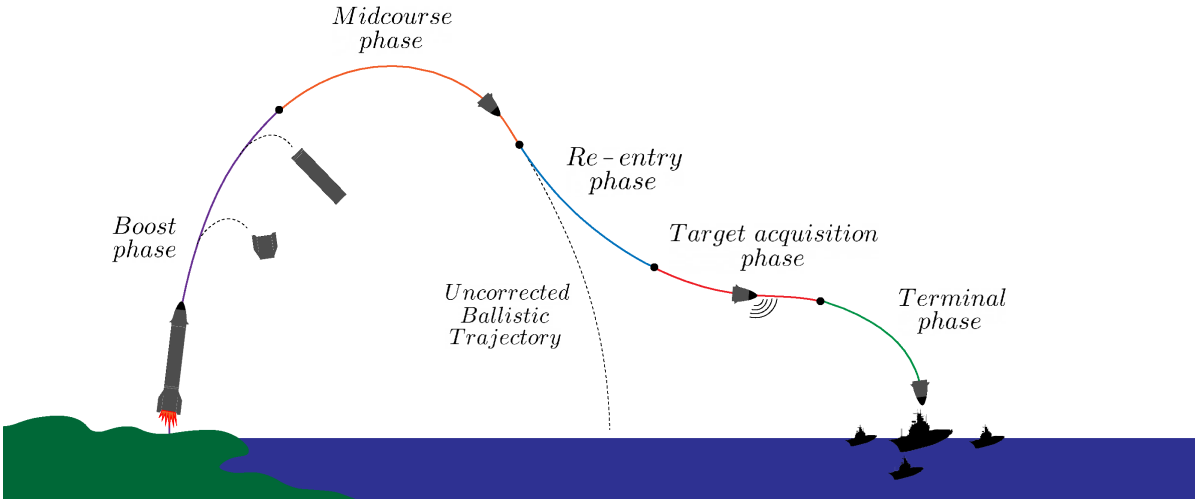

Figure 1.1: Schematic illustration of an ASBM trajectory divided into five different phases (not to scale).

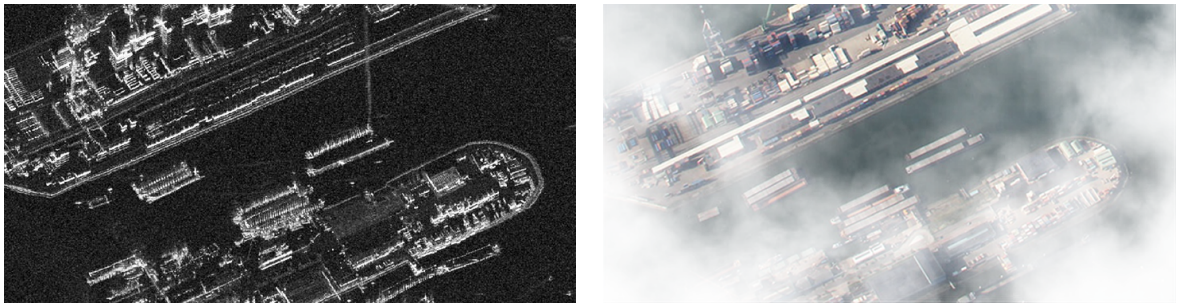

(a) (b)

Figure 1.2: (a) SAR image in X-band with an resolution of 0.25 x 0.25 meter. (b) The same image in the optical wavelength domain. [5].

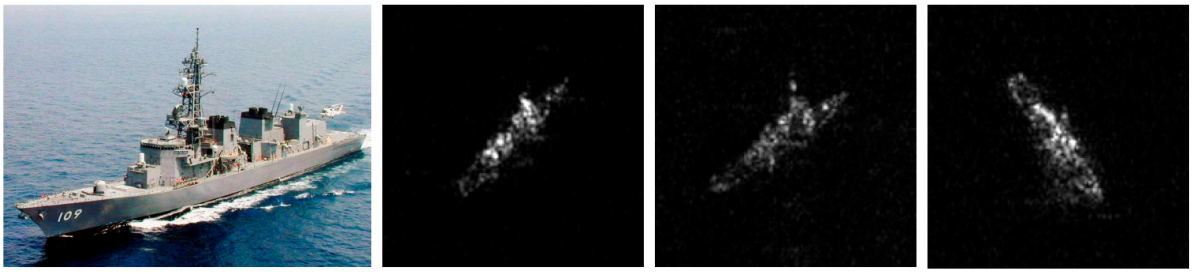

Figure 1.3: SAR images of the JS Ariake (DD-109) destroyer from different view angles [6].

Reconnaissance (ISR). However, such ISR is not always available, is complex and expensive. Therefore, an on-board target acquisition system could extend the capabilities of an ASBM.

There are indications that several countries develop such systems that make use of the imaging capabilities of SAR in recent years [10–12]. SAR is a coherent remote sensing technique that uses radiofrequency radiation and the linear motion of the radar to synthesize a large virtual aperture that is much longer than its physical antenna length. Hence, its name 'synthetic aperture' radar. This allows to obtain high resolution images at great distances. In addition, it is able to provide all-weather and day-night imaging capabilities. A comparison of a SAR image and an image in the optical wavelength domain is shown in Figure 1.2.

SAR systems are usually mounted on satellites or aircraft and used in a wide range of civil applications. However, the improving imaging capabilities of SAR and the fact that maritime surface targets are relatively easy to identify on a flat sea background, as shown in Figure 1.3, make SAR an interesting technique to be used on ASBMs.

However, compared to traditional SAR systems, an ASBM has a high non-linear velocity and a non-straight motion. In addition, SAR systems generally only work for stationary targets, while in ASBM applications the motion of a maritime surface target is unpredictable and cause the target to be defocused in the SAR image that complicates the target acquisition. To minimise the amount of defocus and satisfy the constraints related to the manoeuvrability of an ASBM, the imaging requirements for the acquisition of a target and the constraints of SAR, the trajectory of an ASBM can be optimised. By performing such simulations, the capabilities of this application of SAR can be investigated.

1.2. Research Objective

The objective of this research is to create a simulation model that optimises the trajectory of a SAR seeker on a manoeuvering ballistic re-entry vehicle that provides an insight to the achievable performance of this

system. The imaging capabilities should satisfy the predetermined acquisition requirements of a maritime surface target. This objective leads to the main research question:

What are the limitations and achievable performance of a SAR seeker on an ASBM for the acquisition of a maritime surface target?

The main research question is divided into four sub-questions which are formulated by:

1. What are the requirements for the acquisition of a maritime surface target?
2. How can these requirements be obtained by a SAR seeker?
3. How is the performance of the SAR seeker on an ASBM defined?
4. How can this performance be improved?

The 'ASBM' and 'maritime surface target' terms will be replaced by 'missile' and 'target' respectively for the remaining of this thesis.

1.3. Approach

The research question will be answered by simulating an optimised trajectory for a missile that should satisfy constraints regarding its manoeuvrability, the SAR seeker and the acquisition of a target. This will be done in the optimisation software Generation and Improvement Algorithm for Nonlinear Trajectories (GIANT), provided by TNO. The simulation input includes the dynamics of the missile, the equations related to the SAR seeker performance and the corresponding constraints. The constraints and the parameters used for the SAR seeker are chosen in consultation with TNO experts and based on values found in literature. The achievable performance of the entire system (SAR seeker and missile) will be evaluated on basis of three performance indicators. These are: the exposure time and the vertical end velocity of the missile and the required time for creating one SAR image by the SAR seeker. The limitations of the system follow from the results by changing the constraints to certain values that could improve the acquisition of a target.

1.4. Report Structure

The coordinate frames and state variables of the missile are provided as theoretical background in Chapter 2. In Chapter 3, the aspects and requirements for the acquisition of a target are discussed. The fundamentals of a SAR seeker to achieve these requirements and the corresponding parameters, equations and constraints are given in Chapter 4. An overview of the definition of the optimisation problem and its setup are given in Chapter 5, followed by the validation and verification of some equations of the input model in Chapter 6. The results, including a resolution limitation analysis, are discussed in Chapter 7. Finally, the conclusions and recommendations for future research are given in Chapter 8.

2

Theoretical Background

This chapter provides an overview of the reference frames being used in the model and the transformations between them, as discussed in Section 2.1. A description of the external forces acting on the missile is given in Section 2.2. Finally, its state variables are given in Section 2.3. The provided equations are used in the model to simulate the missile dynamics during the re-entry, acquisition and terminal.

2.1. Reference Frames

This section provides a summary of the used reference frames in the optimisation model and the transformation between them. All frames have Cartesian coordinates.

2.1.1. Reference Frames Definitions

There are a total of five reference frames used in the model. These are described below and illustrated in Figure 2.1.

1) **Local North-East-Down (NED) Frame** $\mathscr{F}_n$ (x_n, y_n, z_n):
The local NED frame is also known as the local level frame, navigation or ground coordinate system. Its origin is fixed to the Earth's surface. The x_n-axis points North, y_n-axis points East and the z_n-axis points Down to the Center Of Gravity (CG) of the Earth, along the direction of the gravitational acceleration. Coordinates in this frame are denoted with a subscript *n*.

2) **Vehicle-Carried NED Frame** $\mathscr{F}_{nv}$ (x_{nv}, y_{nv}, z_{nv})
The directions of this reference frame coincide with the directions of the F_n frame, but the origin of this reference frame is located at the missile's CG. This reference frame helps visualizing the orientation of the next reference frames relative to the $\mathscr{F}_n$ frame. Coordinates in this frame are denoted with a subscript *nv*.

3) **Trajectory Frame** $\mathscr{F}_t$ (x_t, y_t, z_t)
This reference frame describes the direction of the velocity vector relative to the $\mathscr{F}_{nv}$ frame by the flight path angle γ (-90° < γ < 90°) and heading angle χ (-180° < χ < 180°). A positive flight path angle corresponds to a velocity vector pointing up, i.e. away from the surface. A positive heading angle corresponds to a velocity vector with a component in the East-direction. The origin of this frame is located at the missile's CG. The x_t-axis points in the direction of the unit velocity vector $\vec{u}_v$, while the z_t-axis points down

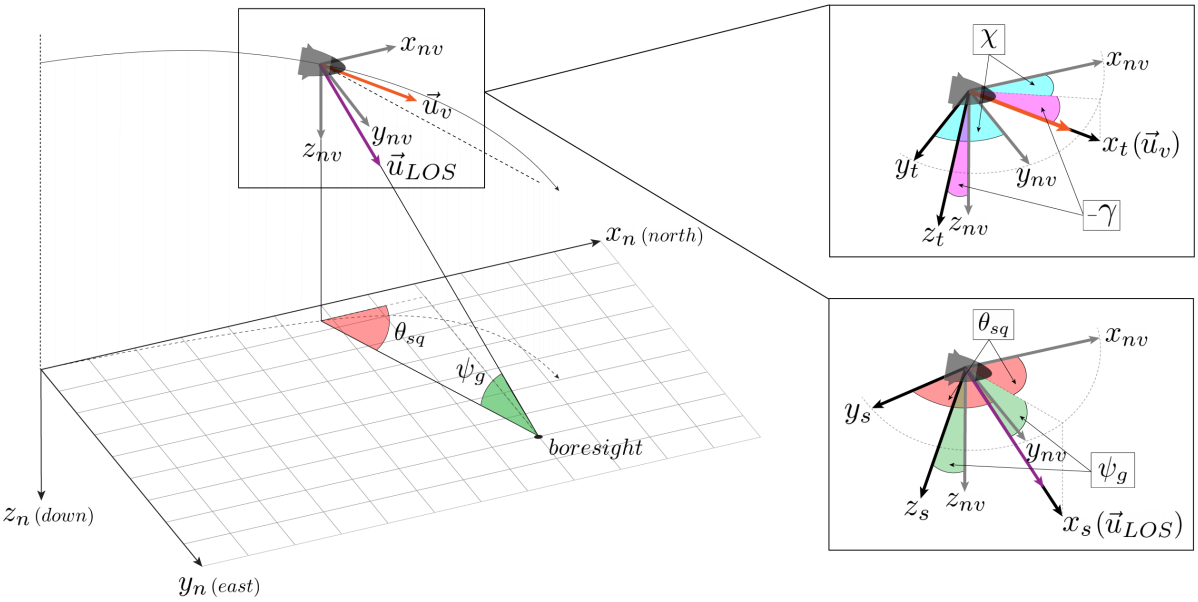

Figure 2.1: Left: the $\mathscr{F}_n$ and $\mathscr{F}_{nv}$ frame with the unit velocity vector $\vec{u}_v$, unit LOS-vector $\vec{u}_{LOS}$, squint angle θ_{sq} and grazing angle ψ_g. The boresight represents the point on the surface of the maximum antenna gain. Right: the $\mathscr{F}_t$ and $\mathscr{F}_s$ frames, including the heading angle χ and flight path angle γ.

perpendicular to x_t-axis. The y_t-axis completes the right-handed coordinate system. Coordinates in this frame are denoted with a subscript *t*.

4) **Line-Of-Sight (LOS) Frame $\mathscr{F}_s$ (x_s, y_s, z_s)**
This reference frame describes the orientation of the radar antenna relative to the $\mathscr{F}_{nv}$ frame by the squint angle θ_{sq} (-180° < θ_{sq} < 180°) and grazing angle ψ_g (0° < ψ_g < 90°). Generally, an antenna is mounted at the front of a missile, meaning that the origin of this frame should be fixed at this location. However, for the sake of convenience, it is assumed that the origin is also fixed at the missile's CG. The x_s-axis points in the direction of the unit LOS-vector $\vec{u}_{LOS}$, i.e. to the boresight (axis of maximum gain), whereas the z_b-axis points downwards perpendicular to the x_s-axis. The y_s-axis completes the right handed coordinate system. Coordinates in this frame are denoted with a subscript *s*.

5) **Body Fixed Frame $\mathscr{F}_b$ (x_b, y_b, z_b)**
This reference frame has its origin located at the missile's CG. It can be used to describe the forces acting on the missile and its rotation about its x_b-, y_b- and z_b-axis, respectively its roll- ϕ, pitch- θ and yaw angle ψ (-180° < ϕ, θ, ψ < 180°). These angles are commonly known as the Euler angles. The x_b-axis points forwards along the longitudinal axis of the missile whereas the z_b-axis points downwards along the vertical axis of the missile. The y_b-axis completes the right handed coordinate system and points along the lateral axis. Coordinates in this frame are denoted with a subscript *b*.

2.1.2. Reference Frames Transformations

The transformation from one reference frame to another can be performed by using a Direction Cosine Matrix (DCM). A DCM consist of single- or multiple unit rotations around the x-, y- or z-axis. By multiplying a sequence of individual unit rotations in consecutive order, the DCM can be represented as a single transformation matrix $\mathbf{C}_a^b$, which transforms any vector in reference frame *a* to reference frame *b* by:

$$\vec{r}_{\mathrm{b}} = \mathbf{C}_{\mathrm{a}}^{\mathrm{b}} \vec{r}_{\mathrm{a}} \tag{2.1}$$

For a reference frame transformation sequence, e.g. transforming any vector in reference frame a to reference frame c, the corresponding transformation matrix can be constructed from individual DCMs:

$$\vec{r}_{\mathrm{c}} = \mathbf{C}_{\mathrm{b}}^{\mathrm{c}} \vec{r}_{\mathrm{b}} = \mathbf{C}_{\mathrm{b}}^{\mathrm{c}} \mathbf{C}_{\mathrm{a}}^{\mathrm{b}} \vec{r}_{a} = \mathbf{C}_{\mathrm{a}}^{\mathrm{c}} \vec{r}_{\mathrm{a}} \tag{2.2}$$

where $\mathbf{C}_{\mathrm{a}}^{\mathrm{c}}$ is the DCM describing the transformation from reference frame a to reference frame c that is constructed from $\mathbf{C}_{\mathrm{b}}^{\mathrm{c}}$ and $\mathbf{C}_{\mathrm{a}}^{\mathrm{b}}$. All transformation matrices are orthonormal, implying that the inverse of a transformation matrix equals its transpose. This means that any vector from reference frame c to reference frame a can be transformed by:

$$\vec{r}_{\mathrm{a}} = \left(\mathbf{C}_{\mathrm{a}}^{\mathrm{c}}\right)^{\mathrm{T}} \vec{r}_{\mathrm{c}} = \mathbf{C}_{\mathrm{c}}^{\mathrm{a}} \vec{r}_{\mathrm{c}} \tag{2.3}$$

A rotation about a single axis with an arbitrary angle α can be described by an unit rotation matrix, where $\mathbf{C}_i$ denotes a rotation matrix around the i-axis by:

$$\mathbf{C}_x = \begin{bmatrix} 1 & 0 & 0 \\ 0 & \cos(\alpha) & \sin(\alpha) \\ 0 & -\sin(\alpha) & \cos(\alpha) \end{bmatrix} \quad \mathbf{C}_y = \begin{bmatrix} \cos(\alpha) & 0 & -\sin(\alpha) \\ 0 & 1 & 0 \\ \sin(\alpha) & 0 & \cos(\alpha) \end{bmatrix} \quad \mathbf{C}_z = \begin{bmatrix} \cos(\alpha) & \sin(\alpha) & 0 \\ -\sin(\alpha) & \cos(\alpha) & 0 \\ 0 & 0 & 1 \end{bmatrix} \tag{2.4}$$

Therefore, the transformation from the trajectory frame $\mathscr{F}_t$ to the vehicle-carried NED frame $\mathscr{F}_{nv}$ is given by:

$$\mathbf{C}_{\mathrm{t}}^{\mathrm{nv}} = \begin{bmatrix} \cos(\chi)\cos(\gamma) & -\sin(\chi) & -\cos(\chi)\sin(\gamma) \\ \sin(\chi)\cos(\gamma) & \cos(\chi) & -\sin(\chi)\sin(\gamma) \\ \sin(\gamma) & 0 & \cos(\gamma) \end{bmatrix} \tag{2.5}$$

The transformation from the LOS-frame $\mathscr{F}_s$ to the vehicle-carried NED frame $\mathscr{F}_{nv}$ is given by:

$$\mathbf{C}_{\mathrm{s}}^{\mathrm{nv}} = \begin{bmatrix} \cos(\theta_{sq})\cos(\psi_g) & -\sin(\theta_{sq}) & \cos(\theta_{sq})\sin(\psi_g) \\ \sin(\theta_{sq})\cos(\psi_g) & \cos(\theta_{sq}) & \sin(\theta_{sq})\sin(\psi_g) \\ -\sin(\psi_g) & 0 & \cos(\psi_g) \end{bmatrix} \tag{2.6}$$

Note that neither of these coordinate transformations include a rotation about the z-axis and only consist of two consecutive transformations about the x- and y-axis because they share the same z-axis. The transformation from the body frame $\mathscr{F}_b$ to the vehicle-carried NED frame $\mathscr{F}_{nv}$ is represented by a quaternion matrix that will be discussed in Section 2.3.

2.2. External Forces

This section provides a description of the models used to describe the external forces acting on the missile. In this research, the missile is considered to have no thrust during re-entry, i.e. only the lift, drag and gravitational forces are taken into account.

2.2.1. Lift and Drag

The lift force F_L is an upward-acting force on the missile, perpendicular to the incoming flow. It results from the movement of the missile through the atmosphere. The drag force F_D is the force parallel to the incoming flow direction. These forces are illustrated in Figure 2.2 and given by:

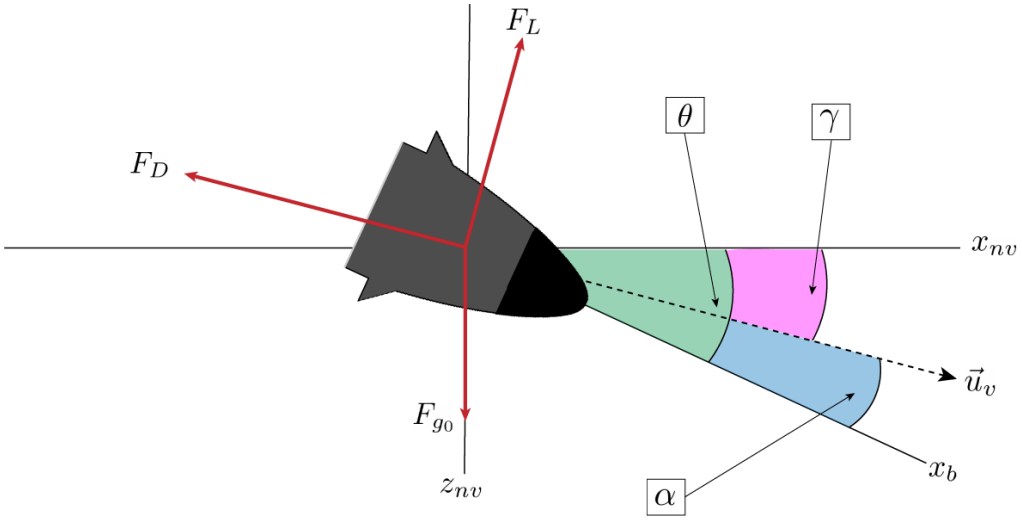

Figure 2.2: The lift F_L, drag F_D and gravitational F_{g_0} forces acting on the missile and the relationship between the angle-of-attack α, flight path angle γ and pitch angle θ.

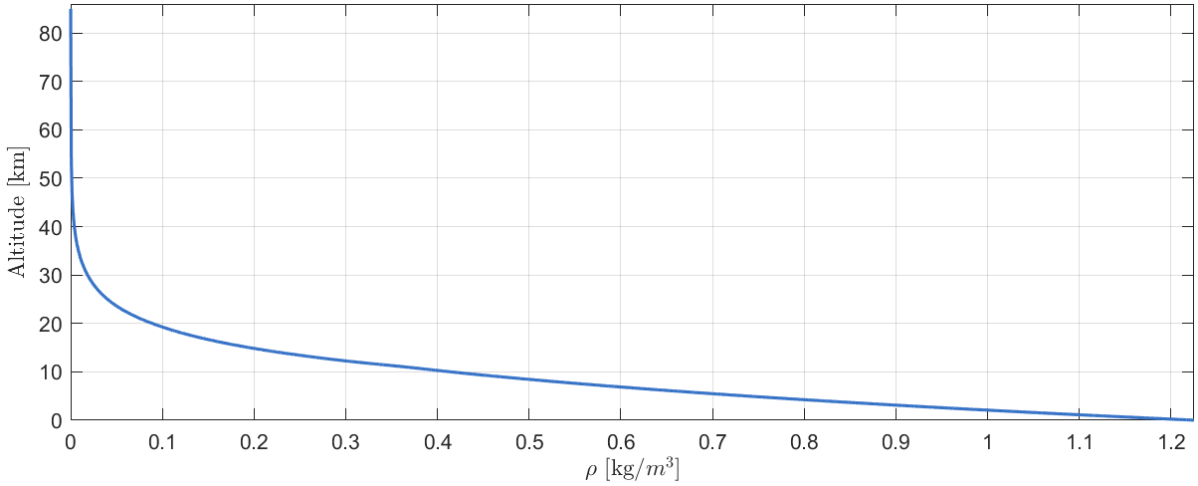

Figure 2.3: Density ρ as a function of the altitude z up to 86.00 km.

$$F_L = C_L \frac{1}{2} \rho V^2 A \tag{2.7}$$

$$F_D = C_D \frac{1}{2} \rho V^2 A \tag{2.8}$$

where C_D is the lift coefficient, C_L the drag coefficient, ρ the atmospheric density, V the absolute velocity of the missile and A its cross sectional area. The atmospheric density ρ depends on the altitude and is calculated from the atmospheric model integrated in the optimisation software GIANT. This atmospheric model is based on the US76 atmospheric model [13], where the atmosphere up to 86.00 km is divided into 7 different layers in altitude. The temperatures variation in each of these layers are analytical approximated which are used for the approximations for the densities at every altitude. Figure 2.3 shows the density as a function of these altitudes, originating from the implemented model.

The lift and drag coefficients are approximated by the principle of a 'circular aerodynamics' model, provided by TNO. This model is a simplification of a lift-drag polar [14], that provides a quick approximation of the

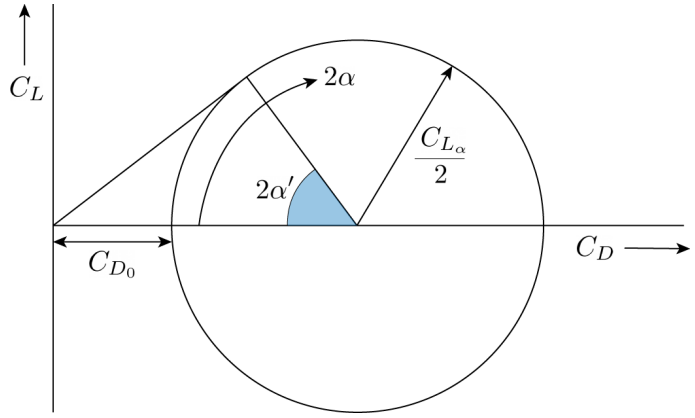

Figure 2.4: Representation of circular aerodynamics, α' represents the angle-of-attack at maximum lift over drag.

relationship between the drag of a vehicle and its lift and angle-of-attack. A simple representation for the lift and drag coefficients is used based on a circular lift-drag curve as illustrated in Figure 2.4. According to the Figure, the lift and drag coefficients are given by:

$$C_L = \frac{C_{L_\alpha}}{2}\sin(2\alpha) = C_{L_\alpha}\sin(\alpha)\cos(\alpha) \tag{2.9}$$

$$C_D = C_{D_0} + \frac{C_{L_\alpha}}{2}\left[1-\cos(2\alpha)\right] = C_{D_0} + C_{L_\alpha}\sin^2(\alpha) \tag{2.10}$$

According to this model, at $\alpha = 90°$, the lift coefficient is zero and the drag coefficient is maximised. In addition, an increase of the drag coefficient is directly related to the lift coefficient derivative, which is always the case in reality. The circular aerodynamics represent an idealised case that uses symmetry to determine the lift and drag coefficient at higher angles-of-attack. The behaviour is realistic up to $\alpha = 45°$. Validations of this model have been conducted by TNO and are therefore not given in this thesis.

Besides the dependency of the angle-of-attack α, the circular lift-drag curve has two coefficients: the lift coefficient with respect to the angle-of-attack C_{L_α} and the zero-lift drag coefficient C_{D_0}, the ratio between these values is constant. A value of $\frac{C_{L_\alpha}}{C_{D_0}} = 65$ was used for this research, provided by TNO. The ballistic coefficient of the missile describes the efficiency of the missile to overcome air resistance. The ballistic coefficient at a zero angle-of-attack, BC_0, is also a constant and given by:

$$BC_0 = \frac{m}{C_{D_0}A} \tag{2.11}$$

where m is the mass of the missile, C_{D_0} the zero-lift drag coefficient and A the cross sectional area of the missile. The drag a_D and lift a_L accelerations can be derived from Newton's second law with Equations (2.7), (2.8), (2.9), (2.10) and (2.11) to:

$$a_L = \frac{F_L}{m} = \frac{\frac{1}{2}\rho V^2}{BC_0}\left[\frac{C_{L_\alpha}}{C_{D_0}}\sin(\alpha)\cos(\alpha)\right] \tag{2.12}$$

$$a_D = \frac{F_D}{m} = \frac{\frac{1}{2}\rho V^2}{BC_0}\left[1 + \frac{C_{L_\alpha}}{C_{D_0}}\sin^2(\alpha)\right] \tag{2.13}$$

The ballistic coefficient at a zero angle-of-attack of $BC_0 = 6000$, provided by TNO, was used in this research.

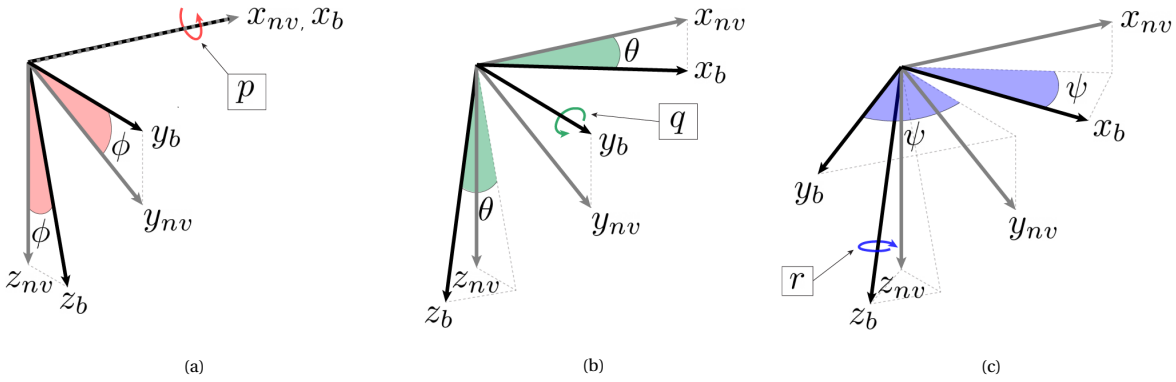

Figure 2.5: (a) The roll angle ϕ and its roll rate p. (b) The pitch angle θ and its pitch rate q. (c) The yaw angle ψ and its yaw rate r.

2.2.2. Gravity

A flat and non-rotating Earth is assumed. Therefore, a constant gravitational acceleration of $g_0 = 9.81\ \mathrm{m/s^2}$ is used [15]. The gravitational force F_{g0} acting on the missile is also illustrated in Figure 2.2.

2.3. State Variables

This section provides the equations related to the state variables of the missile, that describe its rotational and translational motion. The rotational motion defines the missile's attitude and angular rate, while the translational motion defines its position and velocity.

2.3.1. Rotational Motion

The attitude of the missile can be expressed by the Euler angles (ϕ, θ, ψ), that describe the orientation of the body frame $\mathcal{F}_b$ relative to the vehicle-carried NED Frame $\mathcal{F}_{nv}$. The rotations about the x_{nv}-, y_{nv}- and z_{nv}-axis, are expressed by the roll angle ϕ, the pitch angle θ and the yaw angle ψ respectively. The angular velocities of these angles are given by the roll rate p, pitch rate q and the yaw rate r respectively. These Euler angles and the angular velocities are illustrated in Figure 2.5.

Although Euler angles provide an intuitive physical representation and are easy to implement, they suffer from a singularity. This occurs when the pitch angle equals -90° or 90° and the roll- and yaw-axis become identical, limiting the system to rotate only in two axis in space at that particular instant, i.e. losing one degree of freedom. This can be avoided by making use of quaternions. A quaternion is a 4-dimensional hyper-complex number consisting of a real part and an imaginary vector part:

$$Q = [q_0, \mathbf{q}] = \left(q_0, q_1, q_2, q_3\right)^T \tag{2.14}$$

The elements of the quaternion are not mutually independent as they are constrained by:

$$|Q| = \sqrt{q_0^2 + q_1^2 + q_2^2 + q_3^2} = 1 \tag{2.15}$$

A single Euler angle can be converted into a quaternion by:

$$Q = \begin{bmatrix} q_0 \\ q_1 \\ q_2 \\ q_3 \end{bmatrix} = \begin{bmatrix} \cos\left(\alpha/2\right) \\ \sin\left(\alpha/2\right)\cos\left(\beta_x\right) \\ \sin\left(\alpha/2\right)\cos\left(\beta_y\right) \\ \sin\left(\alpha/2\right)\cos\left(\beta_z\right) \end{bmatrix} \tag{2.16}$$

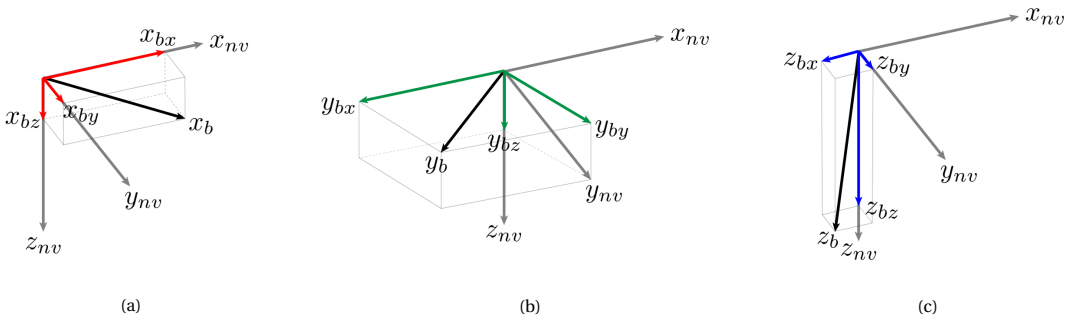

(a) (b) (c)

Figure 2.6: The components of the (a) x_b unit vector (b) y_b unit vector and (c) z_b unit vector.

where α is the Euler angle and β_x, β_y and β_z are the angles between the rotation axis and the x-, y- and z-axis from the other frame respectively. Therefore, the Euler angles ϕ, θ and ψ can be represented as a quaternion by:

$$Q_\phi = \begin{bmatrix} \cos(\phi/2) \\ \sin(\phi/2) \\ 0 \\ 0 \end{bmatrix} \qquad Q_\theta = \begin{bmatrix} \cos(\theta/2) \\ 0 \\ \sin(\theta/2) \\ 0 \end{bmatrix} \qquad Q_\psi = \begin{bmatrix} \cos(\psi/2) \\ 0 \\ 0 \\ \sin(\psi/2) \end{bmatrix} \tag{2.17}$$

Multiplying these expressions provides the quaternions that describes the attitude of the missile [16]:

$$\begin{bmatrix} q_0 \\ q_1 \\ q_2 \\ q_3 \end{bmatrix} = Q_\psi Q_\theta Q_\phi = \begin{bmatrix} \cos(\phi/2)\cos(\theta/2)\cos(\psi/2) + \sin(\phi/2)\sin(\theta/2)\sin(\psi/2) \\ \sin(\phi/2)\cos(\theta/2)\cos(\psi/2) - \cos(\phi/2)\sin(\theta/2)\sin(\psi/2) \\ \cos(\phi/2)\sin(\theta/2)\cos(\psi/2) + \sin(\phi/2)\cos(\theta/2)\sin(\psi/2) \\ \cos(\phi/2)\cos(\theta/2)\sin(\psi/2) - \sin(\phi/2)\sin(\theta/2)\cos(\psi/2) \end{bmatrix} \tag{2.18}$$

The transformation from the body frame $\mathscr{F}_b$ to the vehicle-carried NED frame $\mathscr{F}_{nv}$ is given by the quaternion rotation matrix C (= $\mathbf{C}_{\mathrm{b}}^{\mathrm{nv}}$):

$$C = \begin{bmatrix} q_0^2 + q_1^2 - q_2^2 - q_3^2 & 2(q_1 q_2 - q_0 q_3) & 2(q_0 q_2 + q_1 q_3) \\ 2(q_1 q_2 + q_0 q_3) & q_0^2 - q_1^2 + q_2^2 - q_3^2 & 2(q_2 q_3 - q_0 q_1) \\ 2(q_1 q_3 - q_0 q_2) & 2(q_2 q_3 + q_0 q_1) & q_0^2 - q_1^2 - q_2^2 + q_3^2 \end{bmatrix} \tag{2.19}$$

From this rotation matrix, the conversion from the quaternions to the Euler angles can be expressed by:

$$\phi = \tan^{-1}\left(\frac{C_{12}}{C_{11}}\right) = \tan^{-1}\left(\frac{2(q_1 q_2 + q_0 q_3)}{q_0^2 + q_1^2 - q_2^2 - q_3^2}\right) \tag{2.20}$$

$$\theta = \sin^{-1}(C_{12}) = 2\left(q_1 q_2 + q_0 q_3\right) \tag{2.21}$$

$$\psi = \tan^{-1}\left(\frac{C_{23}}{C_{33}}\right) = \tan^{-1}\left(\frac{2(q_2 q_3 + q_0 q_1)}{q_0^2 - q_1^2 - q_2^2 + q_3^2}\right) \tag{2.22}$$

The columns of the rotation matrix C represent the x_b, y_b and z_b unit vectors respectively:

$$\begin{bmatrix} x_{bx} & y_{bx} & z_{bx} \\ x_{by} & y_{by} & z_{by} \\ x_{bz} & y_{bz} & z_{bz} \end{bmatrix} = \begin{bmatrix} C_{11} & C_{21} & C_{31} \\ C_{12} & C_{22} & C_{32} \\ C_{13} & C_{23} & C_{33} \end{bmatrix} \tag{2.23}$$

The components in the x_{nv}-, y_{nv}- and z_{nv}-directions of each of these unit vectors are illustrated in Figure 2.6.

These components are used to calculate the accelerations of the missile as discussed the following subsection. Finally, the relation between the time derivative of the quaternions and the angular rates is given by [17]:

$$\begin{bmatrix} \dot{q}_0 \\ \dot{q}_1 \\ \dot{q}_2 \\ \dot{q}_3 \end{bmatrix} = \begin{bmatrix} 0 & -p & -q & -r \\ p & 0 & r & -q \\ q & -r & 0 & p \\ r & q & -p & 0 \end{bmatrix} \begin{bmatrix} q_0 \\ q_1 \\ q_2 \\ q_3 \end{bmatrix} \tag{2.24}$$

2.3.2. Translational Motion

The position of the missile is described in the Local North-East-Down (NED) Frame $\mathcal{F}_n$ (x_n, y_n, z_n). However, for the sake of convenience, these coordinates are described by the variables: x-, y- and z for the remaining of this thesis. Hence, these values correspond to a position in the North, East and Down-direction respectively. The absolute velocity V of the missile can be described by three velocity components in the North- V_N, East- V_E and Down-direction V_D. These are described by the flight path angle γ and heading angle χ by:

$$V = \begin{bmatrix} V_N \\ V_E \\ V_D \end{bmatrix} = \begin{bmatrix} V\cos(\gamma)\cos(\chi) \\ V\cos(\gamma)\sin(\chi) \\ -V\sin(\gamma) \end{bmatrix} \tag{2.25}$$

The direction of the lift accelerations N_L on the missile can be calculated by the cross product between the lateral axis of the missile y_b and its velocity vector V:

$$N_L = \begin{bmatrix} N_x \\ N_y \\ N_z \end{bmatrix} = \begin{bmatrix} y_{bx} \times V_N \\ y_{by} \times V_E \\ y_{bz} \times V_D \end{bmatrix} \tag{2.26}$$

Therefore, the accelerations of the missile in the North- (a_N), East- (a_E) and Down-direction (a_D) are given by:

$$\begin{bmatrix} a_N \\ a_E \\ a_D \end{bmatrix} = \begin{bmatrix} a_L N_x - a_D V_N \\ a_L N_y - a_D V_E \\ g_0 + a_L N_z - a_D V_D \end{bmatrix} \tag{2.27}$$

Finally, the angle-of-attack α, the flight path angle γ and the heading angle χ are given by [18]:

$$\alpha = \tan^{-1}\left(\frac{z_b \cdot V}{x_b \cdot V}\right) \tag{2.28}$$

$$\gamma = \tan^{-1}\left(\frac{-V_D}{\sqrt{V_N^2 + V_E^2}}\right) \tag{2.29}$$

$$\chi = \tan^{-1}\left(\frac{V_E}{V_N}\right) \tag{2.30}$$

3

Target Acquisition Requirements

This chapter provides an overview of the requirements for the acquisition of a maritime surface target. Firstly, a target model is chosen and its properties are given in Section 3.1. Secondly, an empirical model is presented that describes the reflections of the sea surface surrounding the target in Section 3.2. Finally, an overview of the requirements for target acquisition is given in Section 3.3.

3.1. Target Properties

For the simulation of this research, a maritime surface target model is required in order to analyse the performance of a SAR seeker. Since no unclassified literature is available about the characteristics of potential military ship targets, a model based on the former civilian Canadian Forces Auxiliary Vessel (CFAV) Quest is used. The CFAV Quest is extensively researched in various studies [19–21] and has therefore been adopted as a reference target in many other studies. Figure 3.1 shows a picture of the this vessel in the optical wavelength domain. Its most important parameters related to this research are summarised in Table 3.1.

An important parameter that describes the detectability of a target is its Radar-Cross-Section RCS. The RCS is a measure of the total amount of energy that gets reflected by a target back to the radar. The total target RCS σ_t of a target depends on many different target characteristics and environmental conditions [22]. Therefore,

Figure 3.1: The Canadian Research Vessel 'CFAV Quest' in the optical wavelength domain [7].

CFAV Quest Properties		
Displacement	2.2	kton
Length	71.63	m
Beam	12.80	m
Draft	4.82	m
Speed	7.50	m/s

Table 3.1: The CFAV Quest displacement, dimensions and speed [1].

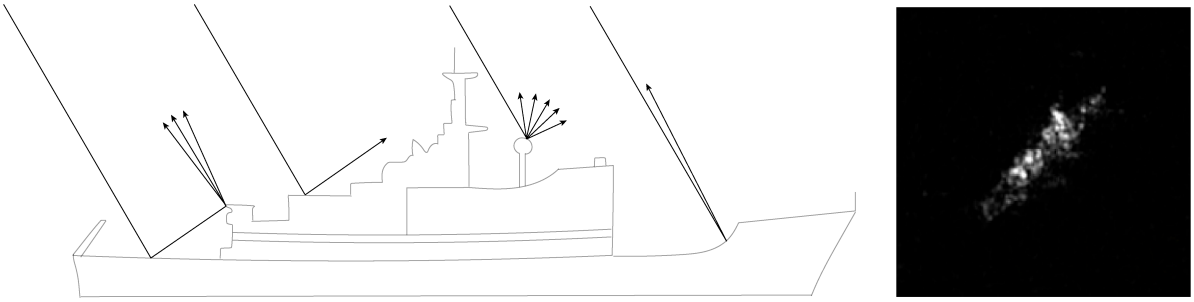

Figure 3.2: Left: Incoming transmitted signals get reflected in different directions and levels due to the target reflectively characteristics and its shape. Right: an example of a SAR image of a ship [8].

there is does not exist a simple formula for calculating this value. Hence, the RCS is typically determined by numerical simulations and experimental measurements. An empirical formula based on the analysis of a large amount of data has been extracted for approximating the total RCS of a ship target σ_t for X-, S- and L-band radar applications, given by [23]:

$$\sigma_{\text{t,total}} = 52 f^{1/2} D^{3/2} \tag{3.1}$$

where f the operating frequency of the radar and D the full displacement of the target. In this research, a center wavelength of λ_c = 0.03 m was used. This corresponds to a center frequency of f_c = 10 GHz. With this value and the full displacement of the CFAV Quest being D = 2.2 kton according to Table 3.1, a total RCS of σ_t = 42.3 dBm^2 is found.

The reflected energy from a target is not uniformly distributed over a target, since it depends on the direction of the incoming wave, its frequency, polarisation, distance from the radar to the target, shape of the target and reflectively characteristics of the target's surface. A schematic illustration of the energy of reflected signals and a SAR image are illustrated in Figure 3.2, where bright spots represent highly reflected signals measured by the radar. Because the signals are not uniformly reflected by the target, it is convenient to use a normalised RCS of the target σ_t^0, given by:

$$\sigma_t^0 = \frac{\sigma_{\text{t,total}}}{A_t} \tag{3.2}$$

where σ_t is the total target RCS and A_t the area of the target. With a total RCS of σ_t = 42.3 dBm^2 and a target area of A_t = 71.63 m × 12.80 m = 917 m^2 according to Table 3.1, a normalised RCS of σ_t^0 = 12.7 dBm^2/m^2 is found, that represents the average RCS per m^2. To detect points that are 100 times (20.0 dB) dimmer, a value of σ_t^0 = 12.7 - 20.0 = -7.3 dBm^2/m^2 has to be used. For the optimisation simulations, a normalised RCS of σ_t^0 = -10.0 dBm^2/m^2, in consultation with TNO experts, is used.

	Polarisation	
Constants	Horizontal	Vertical
c_1	-73.0	-50.79
c_2	20.78	25.93
c_3	7.351	0.7093
c_4	25.65	21.58
c_5	0.00540	0.00211

Table 3.2: Constants for Equation (4.31) for horizontal and vertical polarisation [2].

3.2. Target Environment

Besides the reflected energy of a target, the radar also detects unwanted reflected energy from its surroundings within the illuminated area, known as clutter. Clutter typically originates from the ground, sea surface, precipitation (rain, snow or hail), atmospheric turbulence or ionic atmosphere reflection. In this thesis, it is assumed that the clutter is only originating from the sea surface.

The amount of sea clutter depends on many factors, including the polarisation of the transmitted pulse, its frequency, the incoming angle, sea state and wind direction. Like the RCS of a target, the reflectivity of the sea can also be expressed as a RCS. The reflective properties of the sea surface are complex and subject of study for many decades. A number of empirical models exist that try to describe common sea clutter characteristics. The empirical formula proposed by the Naval Research Laboratory (NRL) was used in this research [2]. The NRL clutter model matches experimental results with an average absolute deviation of 2.6 dB for grazing angles ψ_g in the interval of 0.1 to 60 deg for frequencies from 0.5 GHz to 35 GHz. The expression is given by:

$$\sigma^0_{c(H,V)} = c_1 + c_2 log_{10} \sin\left(\psi_g\right) + \frac{\left(27.5 + c_3 \cdot \psi_g\right) log_{10}(f)}{(1 + 0.95\psi_g)} + c_4 \cdot (1 + SS)^{\frac{1}{2+0.085\psi_g+0.033SS}} + c_5\psi_g^2 \tag{3.3}$$

where ψ_g is the grazing angle in degrees, f_c the center operating frequency of the radar and SS the sea state. c_1, c_2, c_3, c_4 and c_5 are constants that depend on the polarisation of the transmitted wave. These constants are provided in Table 3.2.

The sea-state SS describes the condition of the sea in terms of its wave height, wind speed and wave period. Higher sea-states corresponds to higher waves, wind speeds and wave periods that increases the sea clutter RCS according to Equation (4.31). The characteristics of sea-states 0-8 are given in Table 3.3. The sea clutter RCS for the most occurring sea-states (2-7), different grazing angles, polarisations and an operating frequency of f_c = 10 GHz are shown in Figure 3.3.

A sea-state of SS = 4 is assumed because this sea-state number has the highest probability percentage according to Table 3.3. Furthermore, a vertical polarisation of the electromagnetic waves is used for this research. For this type of polarisation, higher grazing angles ψ_g result in a higher value of sea clutter σ_c according to Figure 3.3b.

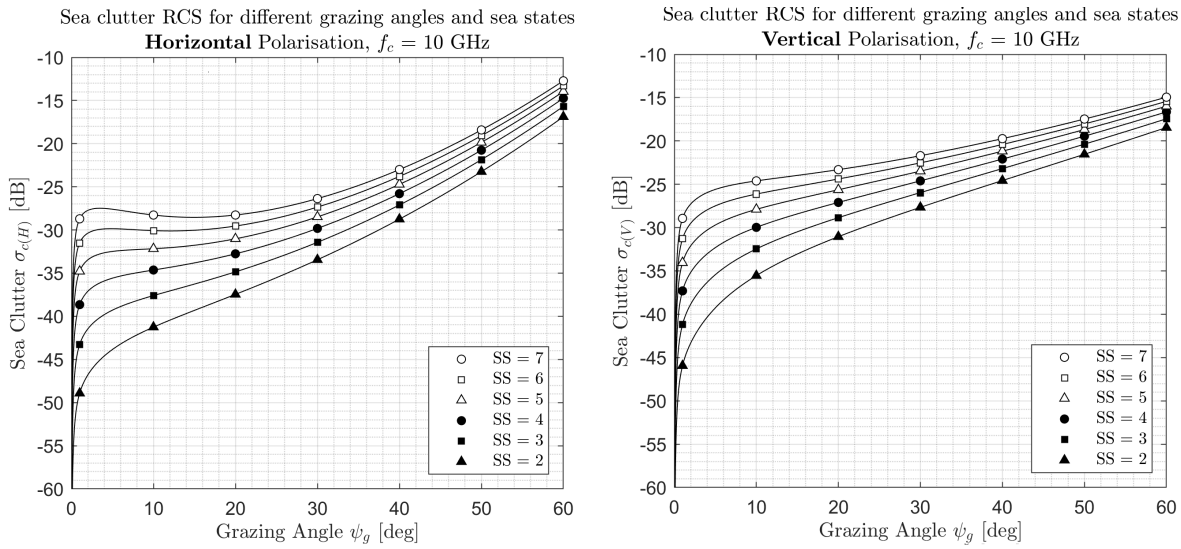

(a) Sea Clutter RCS with horizontal polarisation.

(b) Sea Clutter RCS with vertical polarisation.

Figure 3.3: Sea clutter RCS for different grazing angles and sea states for (a) horizontal and (b) vertical polarisation for a signal with a central frequency of f_c = 10 GHz for Equation (4.31).

Sea State Number	Significate Wave Height [m]	Sustained Wind Speed [kts]	Probability of Sea State [%]	Model Wave Period Range [s]	Modal Wave Period Most Probable [s]
0-1	0 - 0.1	0 - 6	0	-	-
2	0.1 - 0.5	7 - 10	7.2	3.3- 12.8	7.6
3	0.5 - 1.25	11 - 16	22.4	5.0 - 14.8	7.5
4	1.25 - 2.5	17 - 21	28.7	6.1 - 15.2	8.8
5	2.5 - 4	22 - 27	15.5	8.3 - 15.5	9.7
6	4 - 6	28 - 47	18.7	9.8 - 16.2	12.4
7	6 - 9	48 - 55	6.1	11.8 - 18.5	15.0
8	9 - 14	56 - 63	1.2	14.2 - 18.6	16.4
>8	>14	>63	<0.05	15.7 - 23.7	20.0

Table 3.3: NATO Sea States numeral table for the North Atlantic ocean [3].

3.3. Requirements for Target Acquisition

This section provides an overview of the requirements for target acquisition. In this research, these requirements consist of a search area, minimum resolution and minimum Signal-to-Noise Ratio (SNR) and Signal-to-Clutter Ratio (SCR).

3.3.1. Search Area Requirement

At a certain moment before the re-entry of the missile, it is assumed that the coordinates of a target is communicated by an allied UAV, aircraft or satellite. However, during the period between this communication and the start of the acquisition phase, the target may have changed its speed and direction. To account for these possible changes, all the requirements for target acquisition have to be satisfied within a predefined search area. The size and shape of this search area depends on the characteristics and manoeuvrability of the target. However, for the sake of convenience, it is assumed that this search area is circle shaped with a

radius of r_{search}, centered at the last communicated coordinates of the target. The value for this radius can be approximated based on the time between the moment of last provided coordinates and the start of the acquisition phase, and the magnitude of the velocity of the target. Assuming that the missile receives the coordinates of the target 4 minutes before the start of the acquisition phase, and a target velocity of 7.50 m/s according to Table 3.1, the radius is equal to approximately r_{search} = 2.00 km. At the start of the SAR, the antenna points to last provided coordinates, which is assumed to be the actual target location, denoted by [x_t, y_t, z_t].

3.3.2. Resolution Requirement

It is common that maritime surface targets are accompanied by other ships forming a naval fleet. In order to distinguish a target, a certain minimum ground range (depth) and crossrange (width) resolution within the search area has to be achieved. The exact required values for this requirement is a complicated issue. First of all, the performance of post-processing algorithms for missile-borne SAR applications, that could enhance the SAR images and automatically identify a target, is not taken into account because it does not exist yet nor publicly available. Secondly, the requirements for the resolution requirement of a target may be confidential and therefore also not available. However, there are some papers that have investigated the achievable resolution for missile-borne applications that provided an indication of the required resolutions. An example is given in Hongzhong et. al. [24], who investigated the requirements to obtain a crossrange resolution of 3.00 m. Other papers, achieved crossrange resolutions of about 1.00 m and 1.50 m [25, 26].

To investigate the difference between different resolution values, a simulation that generates SAR images of the CFAV Quest, provided by TNO, was used. Figure 3.4 shows SAR images with six different resolutions of the CFAV Quest for a center frequency of f_c = 10 GHz at an azimuth angle of 62°. Every pixel has a certain normalised RCS that depends on the direction of the incoming signal and the characteristics of the CFAV Quest. According to these Figures, lower resolution values provides better image quality that could improve the target acquisition performance. However, as mentioned before, the performance of post-processing algorithms are not taken into account. In addition, during the acquisition phase, the angle between the target and SAR seeker changes over time that causes SAR images to be taken from different azimuth angles. Therefore, in consultation with TNO experts, a minimum resolution of 2.00 x 2.00 m is assumed in this thesis that will provide enough detail for the acquisition algorithms to identify a target.

3.3.3. Target Detectability Requirement

To overcome the power noise originating from the radar internal circuits and the environment, the power of the reflected signals of the target has to be strong enough in order to detect the target. The ratio between these power values is given by the Signal-To-Noise Ratio (SNR). In addition, the power of the reflected signals also have to overcome the background power noise originating from the sea clutter. The ratio between these power values is given by the Signal-To-Clutter Ratio (SCR). The minimum required ratio for the SNR and SCR also depends on performance of post-processing algorithms and other factors that were not taken into account in this research.

Figure 3.5 shows six different SAR images for a resolution of 2.00 x 2.00 m for different SNR values. The sea clutter was not modeled in this simulation and therefore no different SCR values could be illustrated. According to the Figures, a higher SNR value increases the amount of desired reflected energy that increases the chances of detecting the CFAV Quest. In consultation with TNO experts, a minimum SNR and SCR of 20.00 dB is assumed in this research that will provide enough detail for the acquisition algorithms to detect a target.

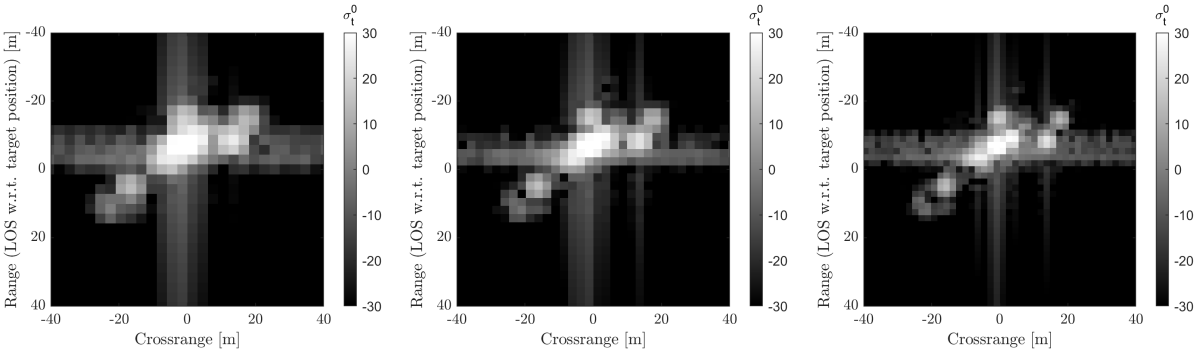

(a) Resolution: 3.00 x 3.00 m. (b) Resolution: 2.50 x 2.50 m. (c) Resolution: 2.00 x 2.00 m.

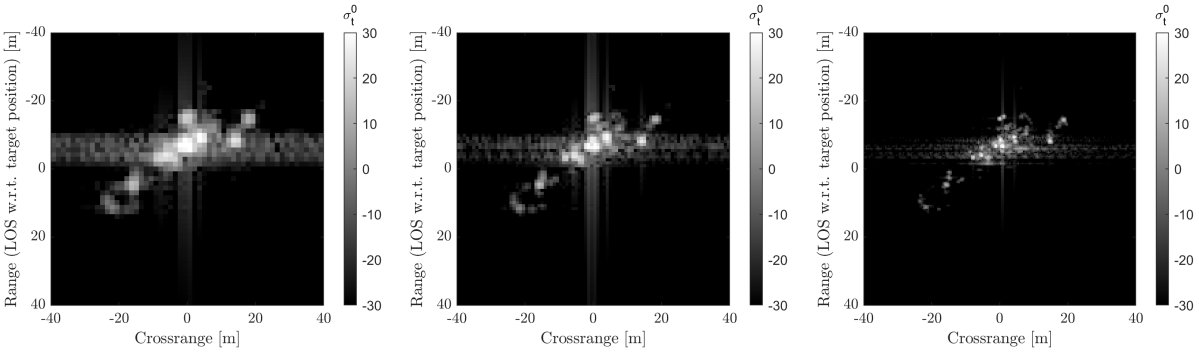

(d) Resolution: 1.50 x 1.50 m. (e) Resolution: 1.00 x 1.00 m. (f) Resolution: 0.50 x 0.50 m.

Figure 3.4: Comparison of different resolution values of the CFAV Quest. σ_t defines the RCS of the pixel.

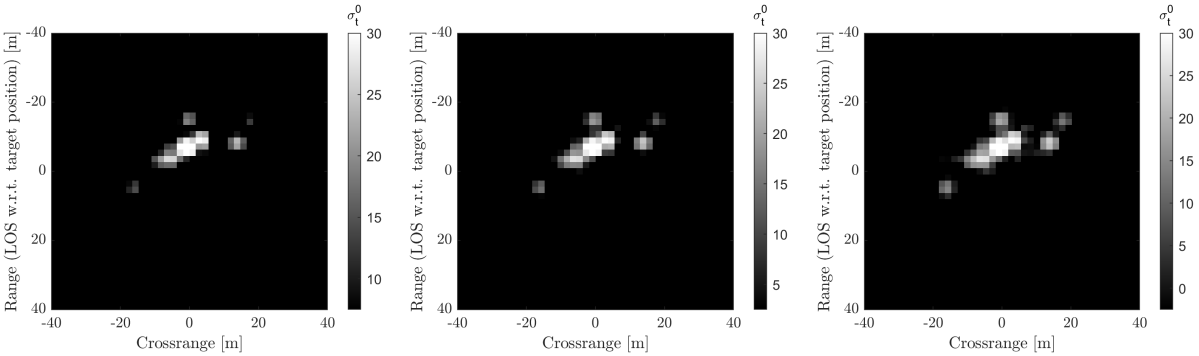

(a) SNR = 5.00 dB. (b) SNR = 10.00 dB. (c) SNR = 15.00 dB.

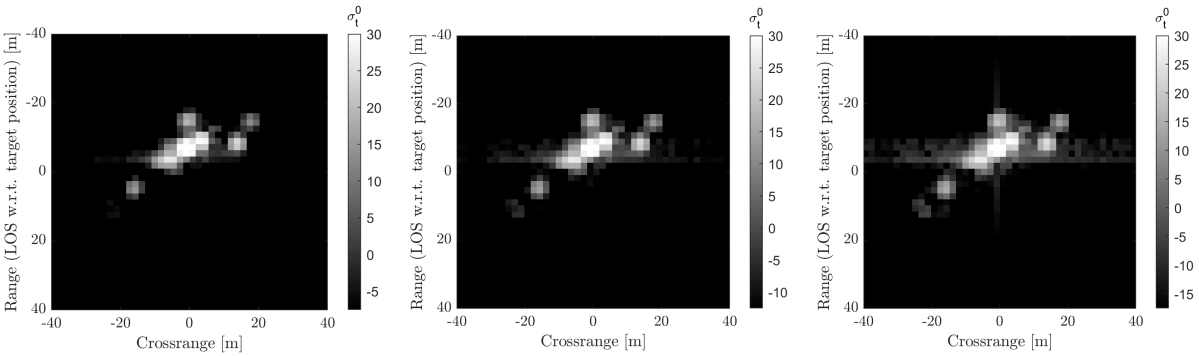

(d) SNR = 20.00 dB. (e) SNR = 25.00 dB. (f) SNR = 30.00 dB.

Figure 3.5: Comparison of different SNR values for the detectability of the CFAV Quest for a resolution of 2.00 x 2.00 m.

4

SAR Seeker Design

This chapter provides the variables, parameters and equations for a SAR seeker on an ASBM to obtain the target acquisition requirements. The geometry of the system is given in Section 4.1 and the SAR seeker design parameters are given in Section 4.2. The equations for obtaining the resolutions are discussed in Section 4.3, while in Section 4.4 the equations regarding the obtainable SNR and SCR are discussed. Finally, the constraints of the SAR seeker are given in Section 4.5.

4.1. Geometry

Figure 4.1 illustrates the geometry of a SAR seeker on an ASBM during its acquisition phase. The distances-to-go in the North-, East- and Down-coordinates from the missile coordinates $[x_m, y_m, z_m]$ to the assumed target location $[x_t, y_t, z_t]$ are given by:

$$R_x = x_t - x_m \tag{4.1a}$$

$$R_y = y_t - y_m \tag{4.1b}$$

$$R_z = z_t - z_m \tag{4.1c}$$

R_s is the slant range and represents the relative distance between the radar and target along $\vec{u}_{LOS}$:

$$R_s = \sqrt{R_x^2 + R_y^2 + R_z^2} \tag{4.2}$$

R_g is the ground range from the missile to the target on the horizontal plane $(x_n y_n)$:

$$R_g = \sqrt{R_x^2 + R_y^2} \tag{4.3}$$

The horizontal angle between the radar and target is given by the squint angle θ_{sq}. The vertical angle is given by the grazing angle ψ_g:

$$\theta_{sq} = \tan^{-1}\left(\frac{R_y}{R_x}\right) \tag{4.4}$$

$$\psi_g = \tan^{-1}\left(\frac{R_z}{R_g}\right) \tag{4.5}$$

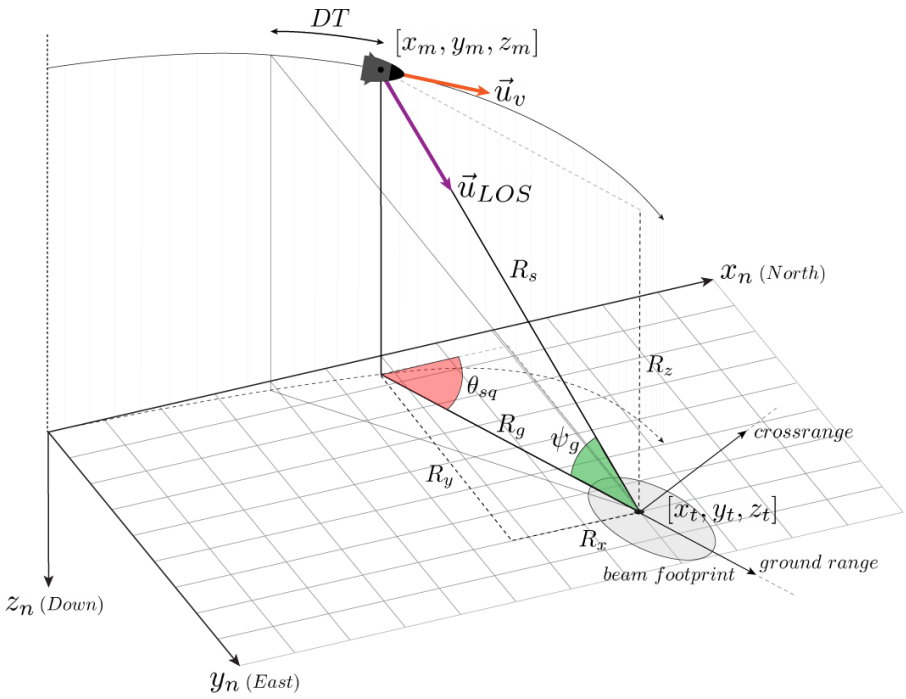

Figure 4.1: Geometry of a SAR seeker for a missile-borne application during the acquisition phase.

The duration of a Coherent Processing Interval (CPI) is given by the Dwell Time DT, also known as the integration time. The absolute velocity of the missile, and thus the SAR seeker, is denoted by V. The direction of the velocity is given by the unit velocity vector $\vec{u}_v$ and the direction of the LOS by the unit vector $\vec{u}_{LOS}$. The 'ground range' points along the direction of the $\vec{u}_{LOS}$ in the horizontal plane, while the 'crossrange' is used for the direction orthogonal to this ground range direction. These directions are used for describing the resolution dimensions in the remaining of this thesis.

4.2. SAR Design Parameters

4.2.1. Operating Frequency and Wavelength

The operating frequency is an important feature of a SAR system as it determines the signal's propagation and reflection properties. SAR systems operate in a wide variety of frequencies that range from 0.3 GHz to 30 GHz due to their atmospheric transmission capabilities as shown in Figure 4.2.

Within the range of 0.3 GHz to 30 GHz, the microwave bands are usually divided into 8 different intervals. The types of these SAR bands and their respective wavelengths and frequencies can be found in Table 4.1. Each of the individual bands have their advantages and disadvantages over each other and their usage depends on its application [27]. For military applications, the X-band is commonly used due to its high resolution imaging and target acquisition capabilities [28]. Furthermore, X-band provides a good compromise of beamwidth, power and atmospheric propagation properties. Therefore, the center operating frequency f_c of 10 GHz is used in this research, corresponding to an operating wavelength of λ_c = 0.03 m.

The propagation losses for any frequency depends on atmospheric conditions, such as the temperature or hazy atmospheric circumstances. In this research, it is assumed that the atmosphere is free of clouds and hazy atmospheric circumstances. For the sake of convenience, a constant atmospheric loss of L_{atmos} = 1 dB is used [29, 30].

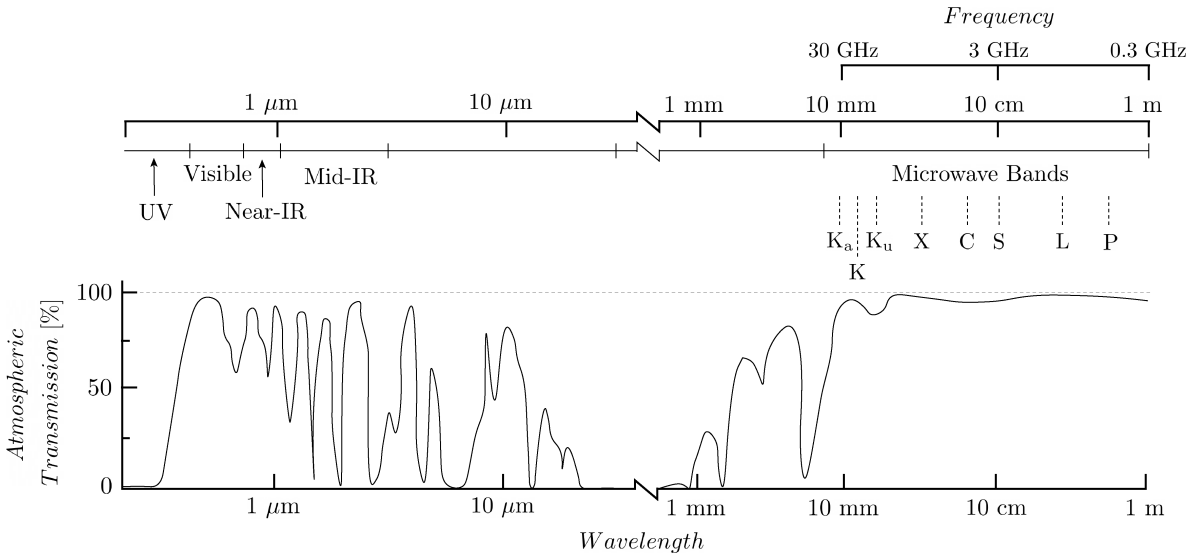

Figure 4.2: Atmospheric transmission [%] of electromagnetic waves in spectral areas of visible light and various radar bands [9].

Band	Frequency [GHz]	Wavelength [cm]
K_a	26.5 - 40.0	0.75 - 1.13
K	18.0 - 26.5	1.13 -1.67
K_u	12.5 - 18.0	1.67 - 2.4
X	8.0 - 12.5	2.4 - 3.75
C	4.0 - 8.0	3.75 - 7.5
S	2.0 - 4.0	7.5 - 15
L	1.0 - 2.0	15 - 30
P	0.3 - 1.0	30 - 100

Table 4.1: Types of SAR bands and their respective wavelengths and frequencies [4].

4.2.2. Waveforms

SAR systems use pulsed radar transmissions to provide range timing information with each pulse. This means that the radar switches between on and off for transmitting and receiving signals respectively. During the dwell time DT, the time interval between two adjacent pulses is represented by the Pulse Repetition Interval (PRI), denoted as T. The Pulse Repetition Frequency (PRF) is the rate that pulses are repeated per second and equals the inverse of the PRI. N is the total amount of pulses during a CPI that equals the DT multiplied by the PRF. The amount of energy of a single pulse is equal to the peak power P_p of the radar multiplied by its pulse duration τ. The average power $\overline{P}$ of a SAR system is the average power over a period T as illustrated in Figure 4.3.

The ratio between the time the radar is transmitting compared to its receive window, i.e. the ratio of the pulse duration τ to T, is known as the duty cycle d_c, given by:

$$d_c = \left(\frac{\overline{P}}{P_p}\right) \times 100\% = \left(\frac{\tau}{T}\right) \times 100\% \tag{4.6}$$

The duty cycle should be at least 50% in order to receive a single transmitted pulse. Conventional SAR satellites typically have a duty cycle ratio of 10% [31], this value is also used in this research in consultation with TNO experts.

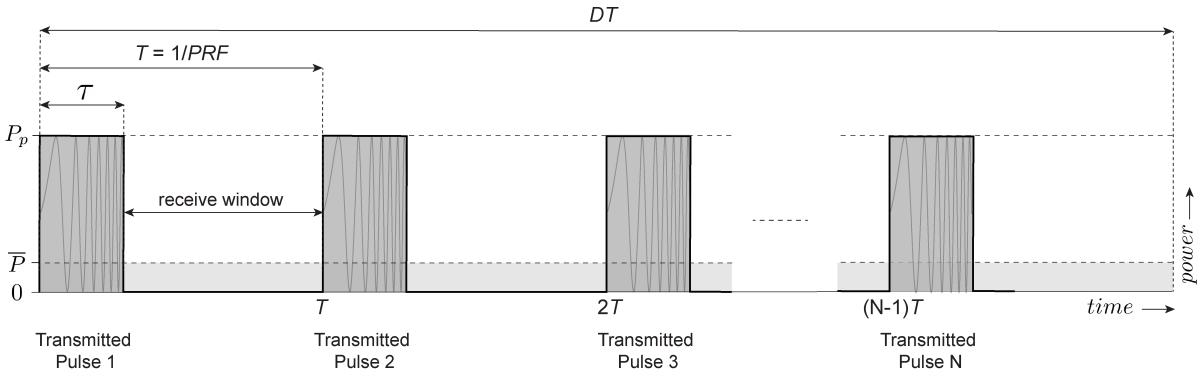

Figure 4.3: Signal timeline including DT, PRF, τ, P_p and $\overline{P}$. The antenna transmits during τ and receives during the receive window.

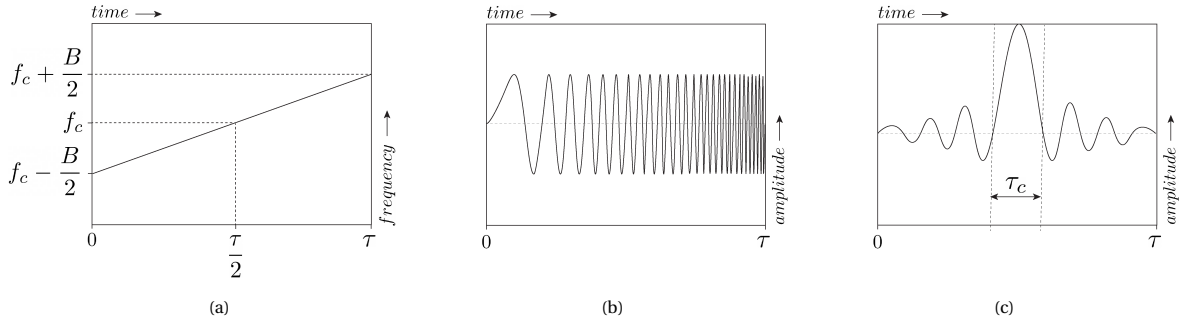

Figure 4.4: (a) Transmitted bandwidth during a single pulse. (b) Linear Frequency Modulated (LFM) waveform with pulse length τ. (c) Output after pulse compression including compressed pulse length τ_c.

Long pulses transmit more energy that increases the amount of energy of the backscattered signals from a target. However, transmitting longer pulses with a fixed desired duty cycle result in fewer pulses to be transmitted during a certain DT and therefore less signals of a target can be collected during a CPI. Besides, longer pulses also decrease the transmitted bandwidth B that worsen the range resolution [32]. To overcome this problem, SAR systems generally use pulse compression modulation techniques. The most commonly used type of modulation is the Linear Frequency Modulation (LFM) that applies a linear increase or decrease to the frequency of the transmitted pulse as illustrated in Figure 4.4a and 4.4b. The total range of frequencies transmitted is known as the bandwidth B and relates to the pulse duration τ by:

$$B = \frac{1}{\tau} \tag{4.7}$$

After pulse compression, the compressed pulse has a much higher amplitude over a shorter period of time τ_c as illustrated in Figure 4.4c. A more detailed explanation of pulse compression can be found in [33]. In consultation with TNO experts, and based on the literature value used in [25], a bandwidth of B = 150 MHz was used in this research.

4.2.3. Antenna

The radar is assumed to be a squared micro strip patch array antenna mounted at the front of the missile with a length and width of l_a = 30 cm. Therefore, the physical area of the antenna is A_a = 30 cm × 30 cm = 0.09 m^2. The antenna gain G describes how strongly the antenna radiates in any direction in space and can be computed by:

$$G = \frac{4\pi A_e}{\lambda_c^2} = \frac{4\pi(\eta_{ap} A_a)}{\lambda_c^2} \tag{4.8}$$

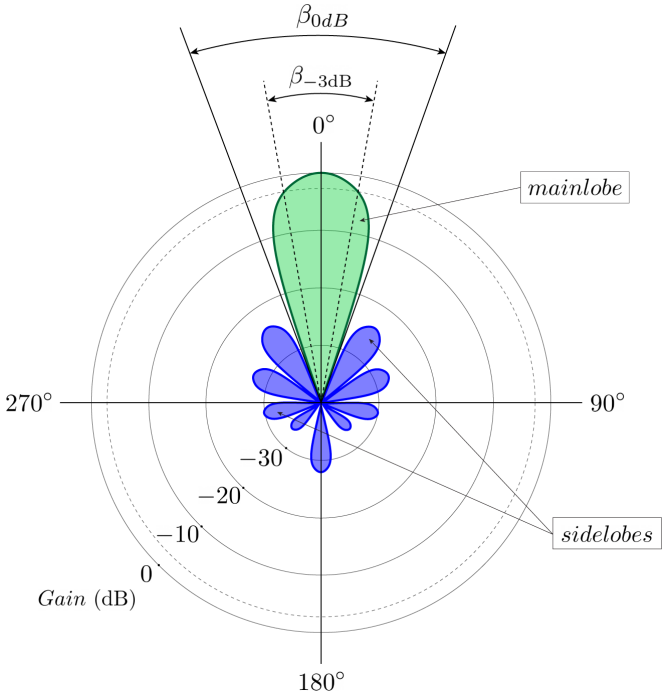

Figure 4.5: Typical antenna radiation pattern.

where A_e is the effective area of the antenna, η_{ap} the aperture efficiency of the antenna, A_a the physical area of the antenna aperture and λ_c the center transmitted wavelength of the radar. Typical values for the aperture efficiency lie between 40-70% [27]. The antenna is assumed to be very efficient, therefore, an aperture efficiency of η_{ap} = 70% is used in this research. According to Equation (4.8) and an operating wavelength of λ_c = 0.03 m, an antenna gain of G = 29.44 dB is found.

The radiation diagram of an antenna describes how strongly the antenna radiates in any direction and is shown in Figure 4.5. The radiation pattern consist of one mainlobe and several sidelobes. However, for the sake of simplicity, the sidelobes are not taken into account in this research. The antenna boresight is the axis of the maximum gain, i.e. the axis at 0° along $\vec{u}_{LOS}$. For a squared microstrip patch array antenna, the Half Power Beam Width (HPBW) $\beta_{-3\text{dB}}$ and the First Null Beam Width (FNBW) $\beta_{0\text{dB}}$ can be calculated by [34]:

$$\beta_{-3\text{dB}} = \frac{60\lambda_c}{l_e} \tag{4.9}$$

$$\beta_{0\text{dB}} = 2\left(\frac{60\lambda_c}{l_e}\right) \tag{4.10}$$

where λ_c is the center transmitted wavelength of the radar and l_a the effective antenna physical length. With an operating wavelength of λ_c = 0.03 m and the antenna length (or width) of l_a = 30 cm, beamwidths of $\beta_{-3\text{dB}}$ = 6.0° and $\beta_{0\text{dB}}$ = 12.0° are found.

The HPBW reflects half the power of the transmitted peak power (-3 dB) and is considered as the useful beam footprint of the transmitted energy. This beamwidth is used for calculations related to the reflected energy from the surface. The FNBW is used for calculations related to ambiguities of the radar. The corresponding variables are illustrated in Figure 4.6 and given by:

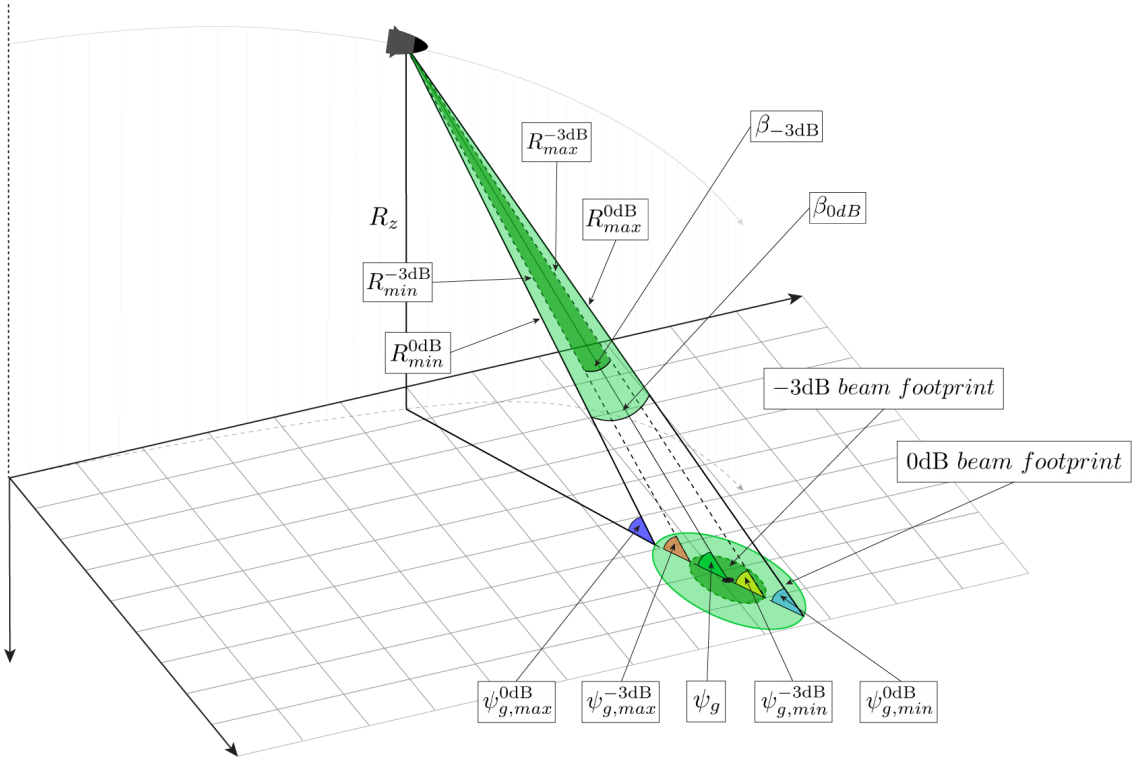

Figure 4.6: Various variables related to the -3dB and 0dB beam footprints.

$$\psi_{\text{g,max}}^{\text{0dB}} = \psi_g + 0.5\beta_{\text{0dB}} \tag{4.11a}$$
$$\psi_{\text{g,max}}^{\text{-3dB}} = \psi_g + 0.5\beta_{\text{-3dB}} \tag{4.11b}$$
$$\psi_{\text{g,min}}^{\text{-3dB}} = \psi_g - 0.5\beta_{\text{-3dB}} \tag{4.11c}$$
$$\psi_{\text{g,min}}^{\text{0dB}} = \psi_g - 0.5\beta_{\text{0dB}} \tag{4.11d}$$

$$R_{\text{max}}^{\text{0dB}} = R_z \sin^{-1}\left(\psi_{\text{g,min}}^{\text{0dB}}\right) \tag{4.12a}$$
$$R_{\text{max}}^{\text{-3dB}} = R_z \sin^{-1}\left(\psi_{\text{g,min}}^{\text{-3dB}}\right) \tag{4.12b}$$
$$R_{\text{min}}^{\text{-3dB}} = R_z \sin^{-1}\left(\psi_{\text{g,max}}^{\text{-3dB}}\right) \tag{4.12c}$$
$$R_{\text{min}}^{\text{0dB}} = R_z \sin^{-1}\left(\psi_{\text{g,max}}^{\text{0dB}}\right) \tag{4.12d}$$

The antenna of a SAR seeker is typically gimballed, allowing the seeker to look sideways relative to the longitudinal axis of the missile. This SAR seeker look angle is illustrated in Figure 4.7, represented by ζ and can be calculated by the dot product between x_b and $\vec{u}_{LOS}$:

$$\zeta = \cos^{-1}\left(x_b \cdot \vec{u}_{LOS}\right) \tag{4.13}$$

To avoid the antenna gimbal to operate behind its physical limit, the seeker look angle if typically constrained. A maximum seeker look angle of 40° was used in [26]. For this research, a maximum SAR seeker look angle $\zeta_{max} = 45°$ is used.

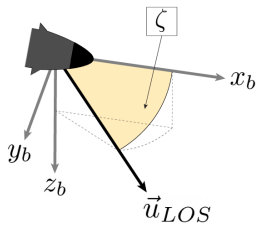

Figure 4.7: The SAR seeker look angle ζ equals the dot product between x_b and $\vec{u}_{LOS}$.

4.3. Resolutions

This section provides the equations regarding to the minimum resolution requirement of 2.00 x 2.00 m as discussed in Section 3.3.2. A resolution cell consist of a distance in the ground range and crossrange directions. Hence, the 'ground range' and the 'crossrange' resolution. The influence of different variables on these resolutions will be discussed as well.

4.3.1. Ground Range Resolution

The ground range resolution of a radar determines the distance between (point) targets that can be distinguished in the ground range direction. The range data acquisition of a SAR is identically the same as conventional radars; a signal is transmitted and backscattered signals are received at different times that provide range information. The ground range resolution ρ_{gr} is given by:

$$\rho_{gr} = \frac{c}{2B\cos(\psi_g)} \tag{4.14}$$

where c is the speed of light, B is the transmitted bandwidth of the radar and ψ_g the grazing angle. Note that lower values for the resolution represent better resolutions. To achieve better resolutions, it is desired to use wider bandwidths and/or fly at lower grazing angles. This relation is shown in Figure 4.8 for five different bandwidths and different grazing angles. If a ground range resolution of ρ_{gr} = 2.00 m is required, and the radar has a bandwidth of B = 150 MHz, the maximum grazing angle the radar may operate is at $\psi_g = 60°$. An illustration of the ground range contours and colormap for a bandwidth of B = 150 MHz at an altitude of 10, 15 and 20 km are shown in Figures 4.9-4.11. The Figures also include a search area with the radius of 2.00 km, located at 10 km in both North- and East-directions relative from the missile as an example. These Figures illustrate how the ground range resolution is distributed over the search area.

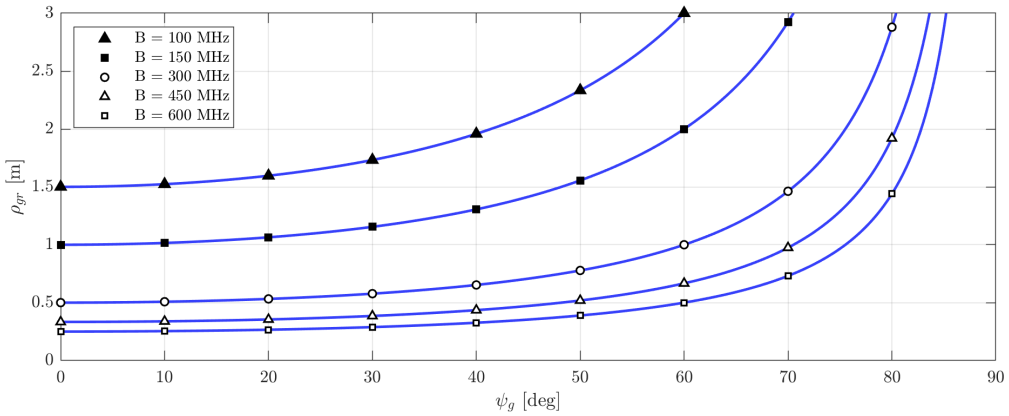

Figure 4.8: The ground range resolution ρ_{gr} as function of the grazing angle ψ_g for different bandwidths B. Lower ρ_{gr} values represent better resolutions.

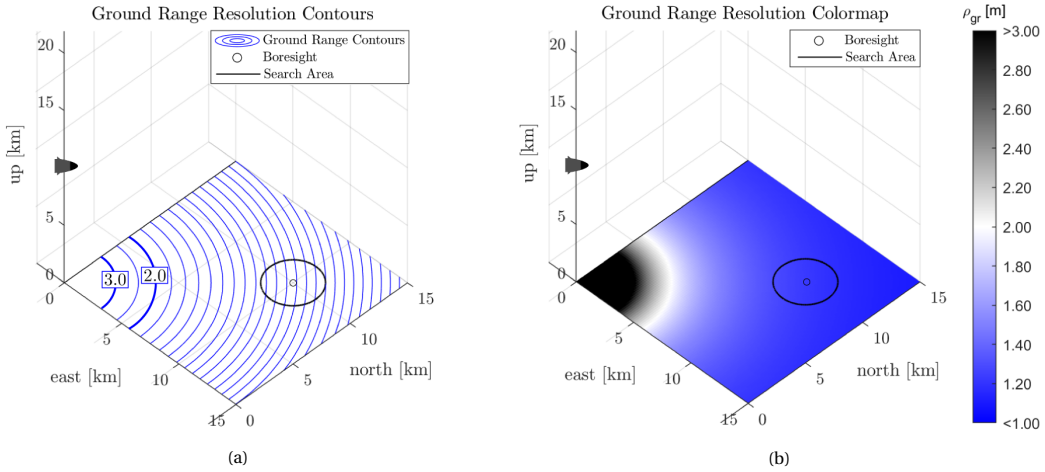

(a) (b)

Figure 4.9: (a) Ground range resolution ρ_{gr} contours and (b) the corresponding colormap for a radar with a bandwidth of B = 150 MHz at an altitude of 10 km. The boresight has a grazing angle of $\psi_g = 54.74°$.

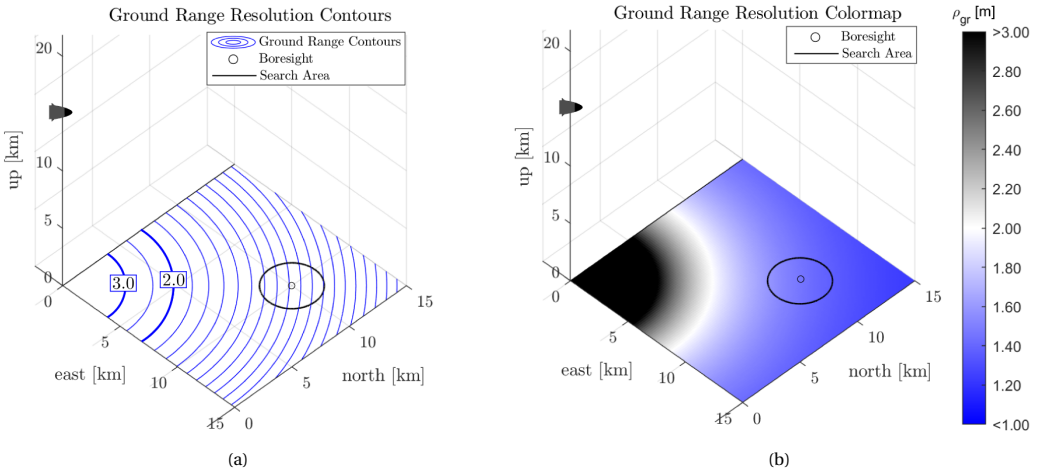

(a) (b)

Figure 4.10: (a) Ground range resolution ρ_{gr} contours and (b) the corresponding colormap for a radar with a bandwidth of B = 150 MHz at an altitude of 15 km. The boresight has a grazing angle of $\psi_g = 46.69°$.

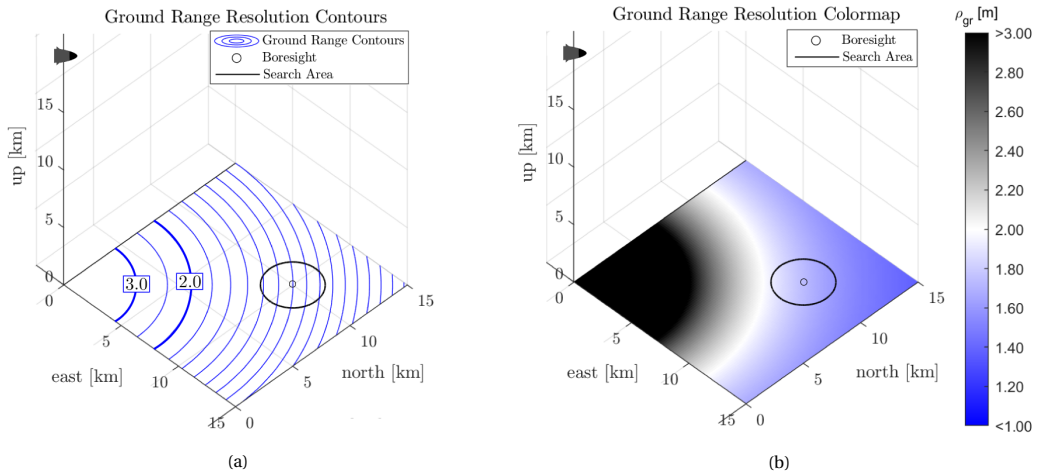

(a) (b)

Figure 4.11: (a) Ground range resolution ρ_{gr} contours and (b) the corresponding colormap for a radar with a bandwidth of B = 150 MHz at an altitude of 20 km. The boresight has a grazing angle of $\psi_g = 35.26°$.

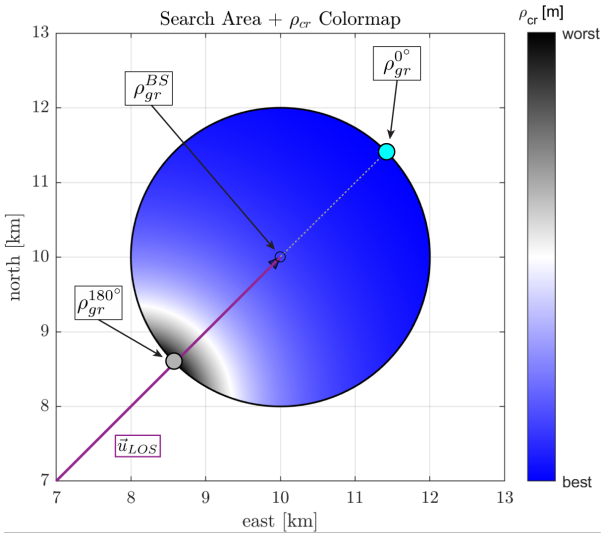

Figure 4.12: Ground range colormap of the search area, including the positions of the best, worst and boresight ground range resolution locations.

Based on Equation (4.14) and Figures 4.9-4.11, flying at lower altitudes improves the ground range resolution, due to the lower grazing angles. Therefore, to obtain better ground resolutions within the search area at a certain fixed distance, the missile has to fly lower or the radar has to use a wider bandwidth.

Another conclusion that can be made based on Equation (4.14) and Figures 4.9-4.11, is that the best ground range resolution within the search area is always located at the far edge relative to the radar. For the remaining of this thesis, this point will be indicated as $\rho_{gr}^{0^\circ}$. The worst ground range resolution is always located at the near edge of the search area relative to the radar, indicated as $\rho_{gr}^{180^\circ}$, due to its larger grazing angle. The ground range resolution at the boresight will be indicated by ρ_{gr}^{BS}. An overview of these locations are shown in Figure 4.12. To ensure that the ground range resolution constraint of $\rho_{gr} = 2.00$ m is obtained everywhere in the search area, it is assumed that $\rho_{gr}^{180^\circ}$ should always be lower than 2.00 m:

$$\rho_{gr}^{180^\circ} < 2.00 \text{ m} \tag{4.15}$$

4.3.2. Crossrange Resolution

The crossrange resolution of a radar determines the distance between (point) targets that can be distinguished in the crossrange direction. This can be achieved by analysing the Doppler shifts of the received signals, induced by the changing range during the during the CPI. The Doppler shift is given by:

$$f_D = \frac{2V\cos(\Omega)}{\lambda} \tag{4.16}$$

where V is the absolute velocity of the missile and Ω the total angle between the velocity vector $\vec{u}_v$ and the LOS-vector $\vec{u}_{LOS}$, given by:

$$\Omega = \cos^{-1}(\vec{u}_v \cdot \vec{u}_{LOS}) \tag{4.17}$$

The Doppler resolution ρ_{f_D} describes the ability to resolve the Doppler shifts of targets located at the same range by:

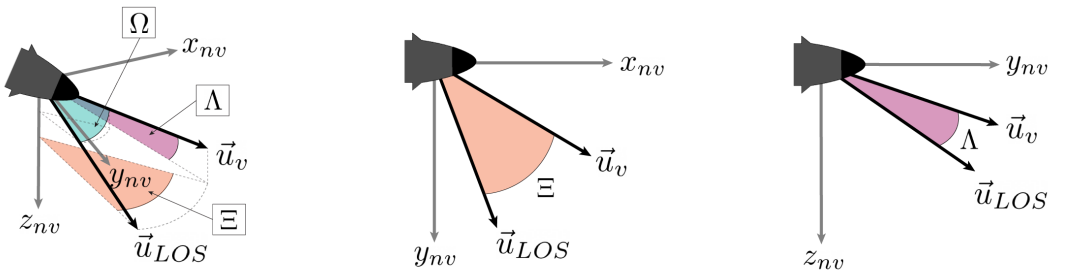

(a) (b) (c)

Figure 4.13: (a) The total angle Ω, horizontal angle Ξ and vertical angle Λ between the velocity vector $\vec{u}_v$ and the LOS-vector $\vec{u}_{LOS}$. (b) Top view of F_{nv} illustrating the horizontal angle Ξ. (c) Side view of F_{nv} illustrating the vertical angle Λ.

$$\rho_{f_D} = \frac{1}{DT} \tag{4.18}$$

where DT is the dwell time. Therefore, longer DT are desired since it improves the Doppler resolution. A derivation of the Doppler resolution to the crossrange resolution can be found in [26] and is given by:

$$\rho_{cr} = \frac{\lambda_c R}{2V(DT)\sin(\Xi)\cos(\Lambda)} \tag{4.19}$$

where λ_c is the center wavelength of the transmitted signal, R the range between the missile and point target, V the absolute velocity of the missile, DT the dwell time and Ξ and Λ the horizontal and vertical angle between the velocity vector $\vec{u}_v$ and the LOS-vector $\vec{u}_{LOS}$. These two angles are given by:

$$\Xi = \cos^{-1}\left[\sin(\theta_{sq})\sin(\chi) + \cos(\theta_{sq})\cos(\chi)\right] \tag{4.20}$$

$$\Lambda = \cos^{-1}\left[-\sin(\psi_g)\cos(\theta_{sq})\sin(\gamma)\cos(\chi) - \sin(\theta_{sq})\sin(\psi_g)\sin(\gamma)\sin(\chi) + \cos(\psi_g)\cos(\gamma)\right] \tag{4.21}$$

where θ_{sq} is the squint angle, ψ_g the grazing angle, γ the flight path angle and χ the heading angle. Note that Ξ and Λ equal the dot product between the second and third columns respectively of the rotation matrix $\mathbf{C}_{\mathrm{t}}^{\mathrm{nv}}$ in Equation (2.5) and $\mathbf{C}_{\mathrm{s}}^{\mathrm{nv}}$ in Equation (2.6). These angle are illustrated in Figure 4.13. Ξ and Λ will be referred as the 'horizontal look angle' and 'vertical look angle' for the remaining of this thesis.

The crossrange resolution depends on many different variables. The influence of each of these variables will now be shown for a scenario with the parameters summarised in Table 4.2. The corresponding range R, squint angle θ_{sq}, grazing angle ψ_g, horizontal Ξ and vertical Λ look angles and crossrange resolution ρ_{cr}, according to Equation (4.2), (4.4), (4.5), (4.20) (4.21) and (4.19) are given in Table 4.3. The crossrange resolution contours and colormap for this scenario with a search area with r_{search} = 2.00 km, are illustrated in Figure 4.14. The influences of different ranges R, velocities V and dwell times DT on the crossrange resolution are illustrated in Figure 4.15a-4.15c. The influences of different squint angles θ_{sq}, grazing angles ψ_g, flight path angles γ and heading angles χ on the crossrange resolution are illustrated in Figures 4.16-4.27.

Assumed missile, radar and target parameters

$[x_m, y_m, z_m]$ [km]	$[x_t, y_t, z_t]$ [km]	λ_c [m]	V [m/s]	γ [deg]	χ [deg]	DT [s]
[0, 0, 15]	[10, 10, 0]	0.03	2000	0.00	0.00	0.20

Table 4.2: Assumed parameters for an example scenario to demonstrate the influence of different variables on the crossrange resolution.

Corresponding variables to Table 4.2

R [km]	θ_{sq} [deg]	ψ_g [deg]	Ξ [deg]	Λ [deg]	ρ_{cr} [m]
20.62	45.00	46.69	45.00	46.69	1.59

Table 4.3: Corresponding variables related to the crossrange resolution calculated from the parameters from Table 4.2.

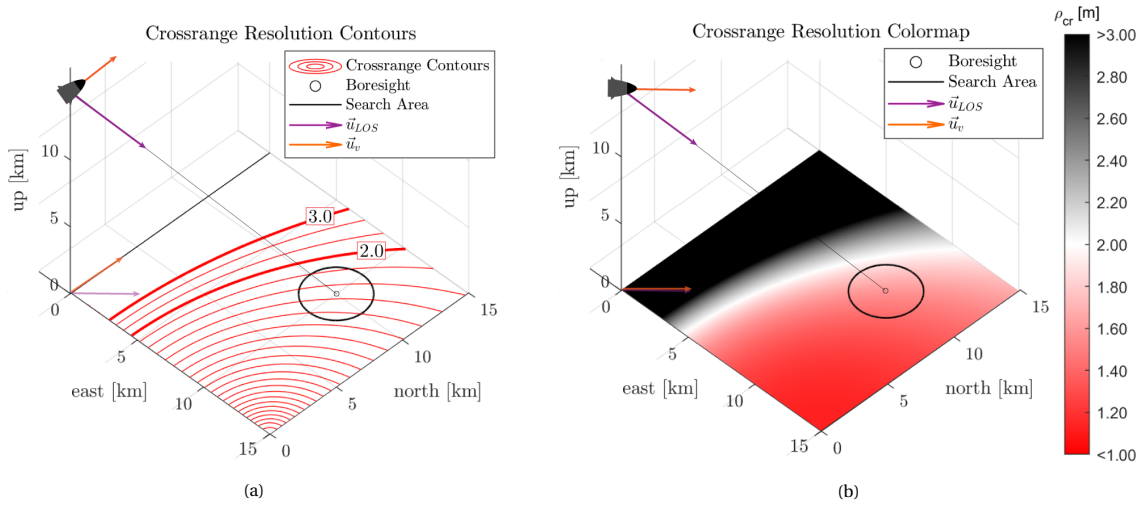

Figure 4.14: (a) Crossrange resolution contours and (b) colormap for the parameters in Table 4.2.

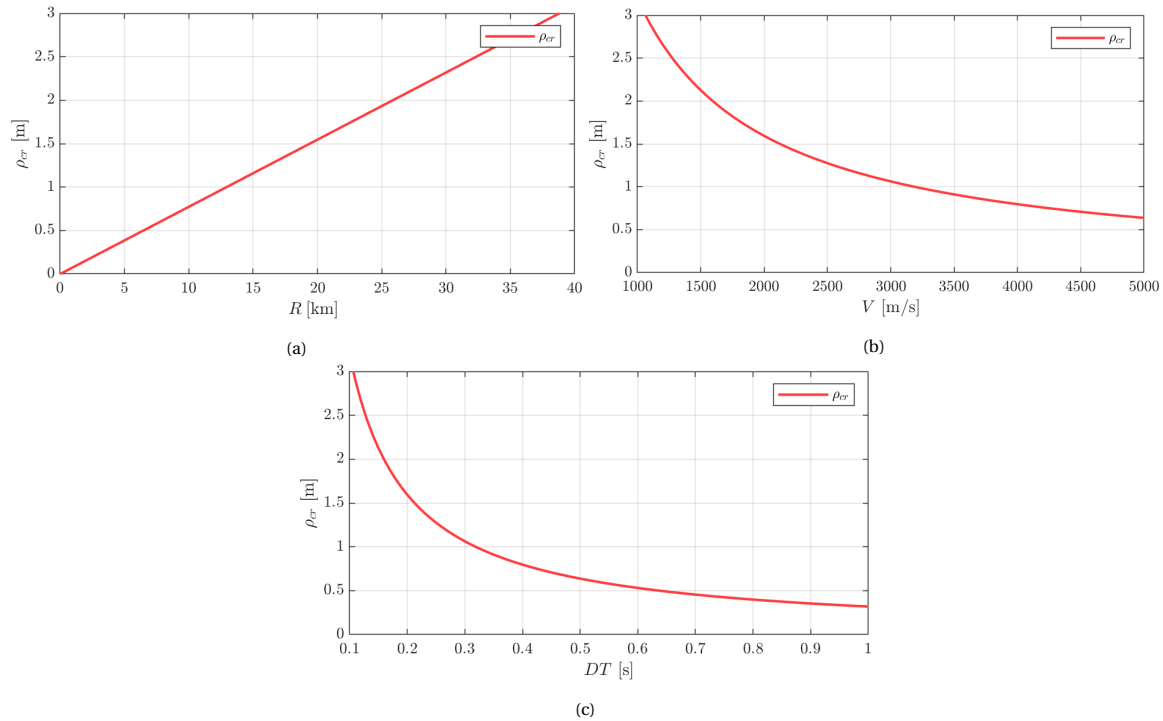

Figure 4.15: (a) Influence of the slant range, (b) velocity of the missile and (c) dwell time on the boresight crossrange resolution for the parameters in Table 4.3.

Based on Equation (4.19) and Figure 4.15a-4.15c, the crossrange resolution improves (i.e. lower values) for lower ranges R, higher missile's velocities V and higher dwell times DT.

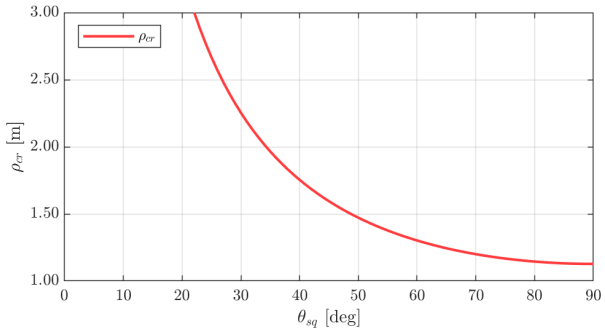

Figure 4.16: Influence of the squint angle θ_{sq} on the boresight crossrange resolution ρ_{cr}.

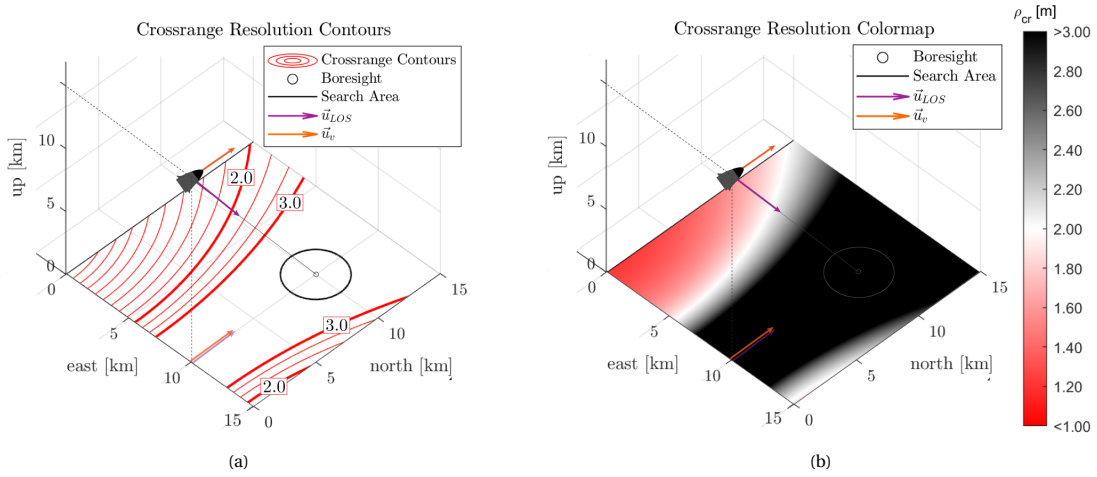

Figure 4.17: (a) Crossrange resolution contours and (b) crossrange resolution colormap for $\theta_{sq} = 0°$.

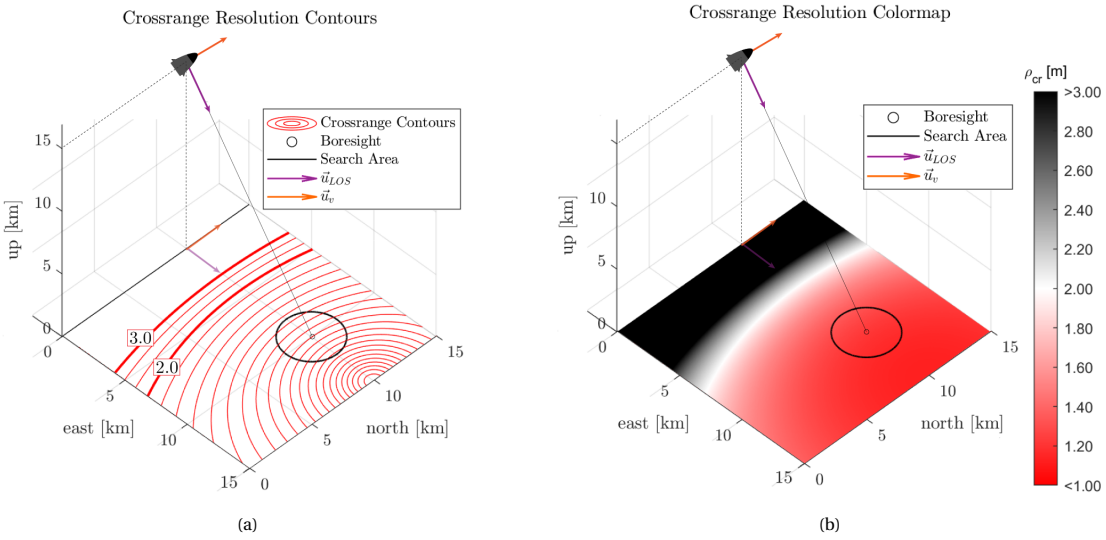

Figure 4.18: (a) Crossrange resolution contours and (b) crossrange resolution colormap for $\theta_{sq} = 90°$.

Based on Figures 4.16, the crossrange improves for higher squint angles θ_{sq}. An illustration for squint angles of $\theta_{sq} = 0°$ and $\theta_{sq} = 90°$ are given in Figures 4.17 and 4.18 respectively.

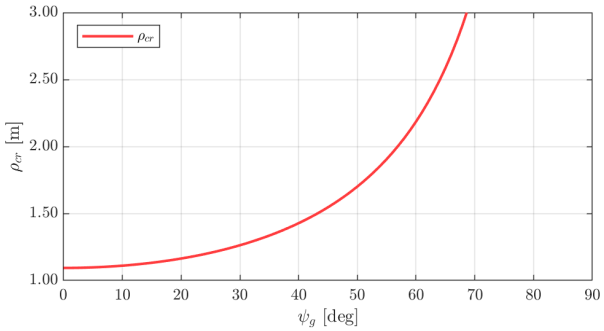

Figure 4.19: Influence of the grazing angle ψ_g on the boresight crossrange resolution ρ_{cr}.

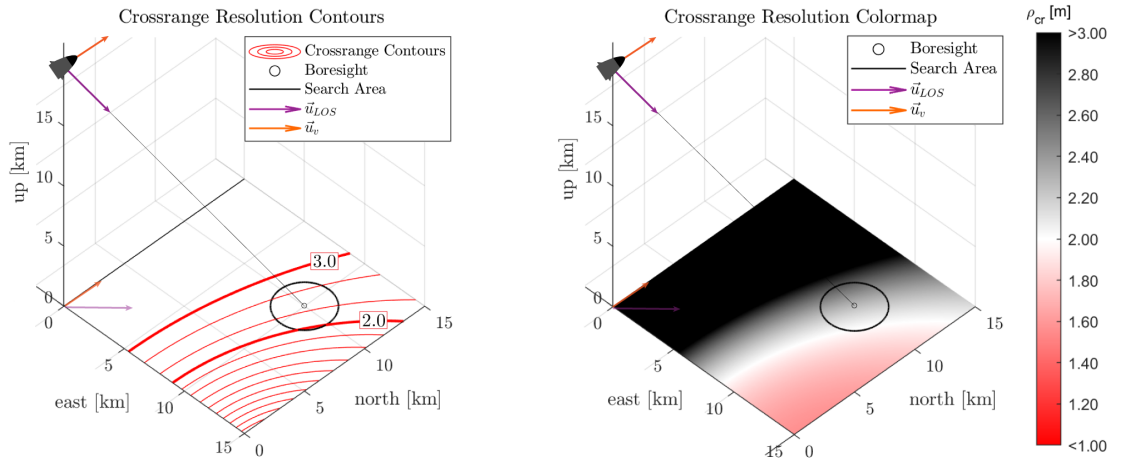

Figure 4.20: Altitude = 20 km. (a) Crossrange resolution contours and (b) crossrange resolution colormap for $\psi_g = 54.73°$.

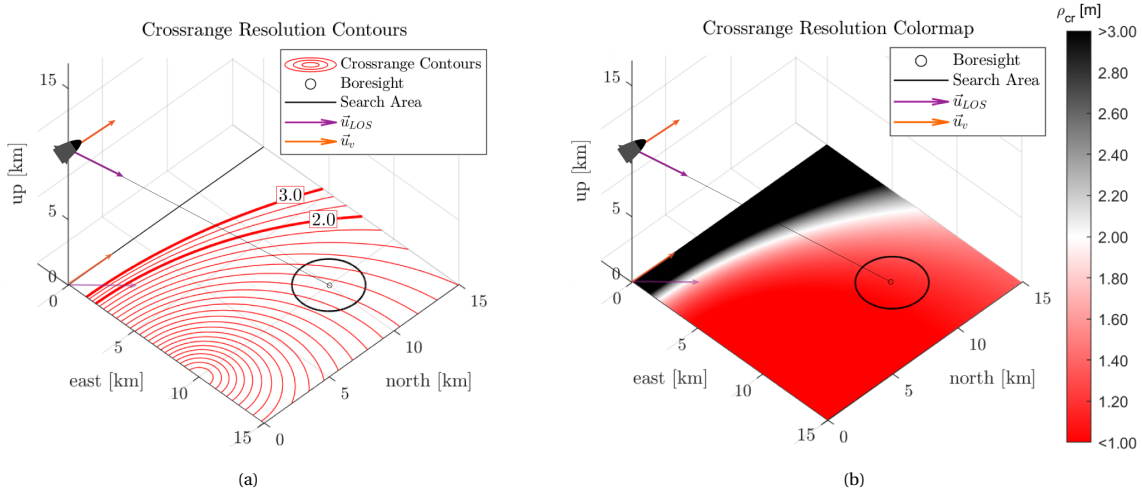

Figure 4.21: Altitude = 10 km. (a) Crossrange resolution contours and (b) crossrange resolution colormap for $\psi_g = 35.26°$.

Based on Figures 4.19, the crossrange resolution improves for lower grazing angles ψ_g. Therefore, flying at lower altitudes improve the crossrange resolution, as illustrated in Figures 4.20 and 4.21.

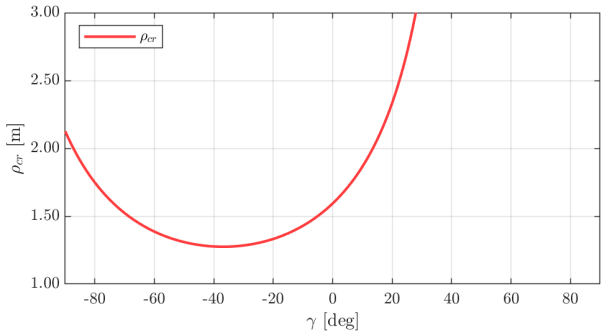

Figure 4.22: Influence of the flight path angle γ on the boresight crossrange resolution ρ_{cr}.

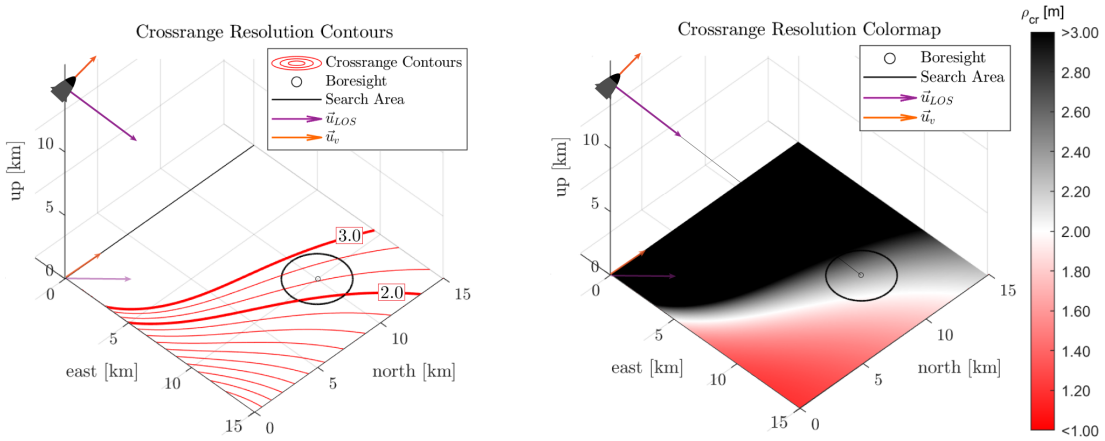

Figure 4.23: (a) Crossrange resolution contours and (b) crossrange resolution colormap for γ = 20.00°.

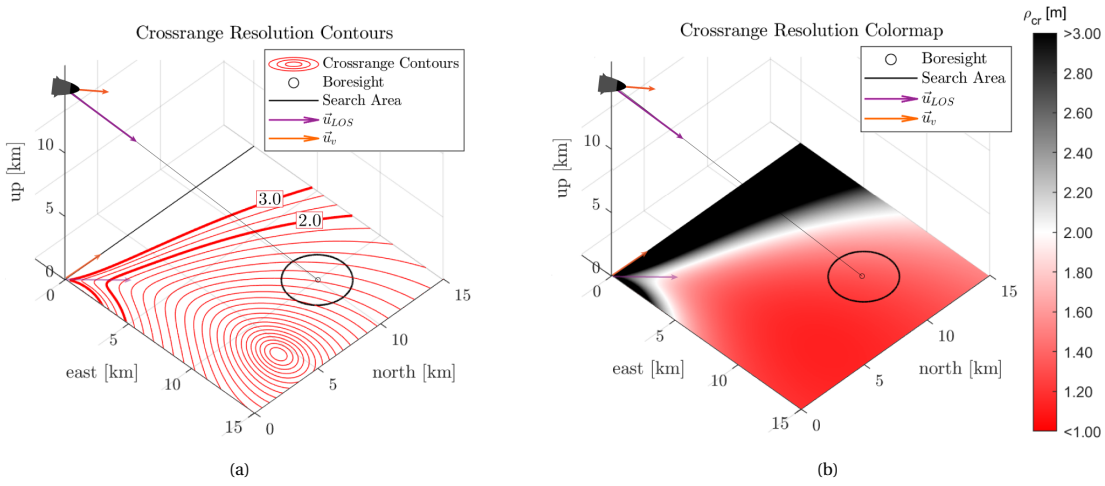

Figure 4.24: (a) Crossrange resolution contours and (b) crossrange resolution colormap for γ = -20.00°.

As illustrated in Figure 4.22, the best crossrange resolution can be obtained for γ = -36.87°. This value depends on the geometry between the radar and target and this value can analytical be solved by Equation (4.21). Therefore, in general, the crossrange resolution improves for velocities with a down component, until a certain flight path angle that depends on the geometry of the scenario. Figures 4.23 and 4.24 illustrates the crossrange resolution contours and colormap for flight path angles of γ = 20.00° and γ = -20.00° respectively as an example.

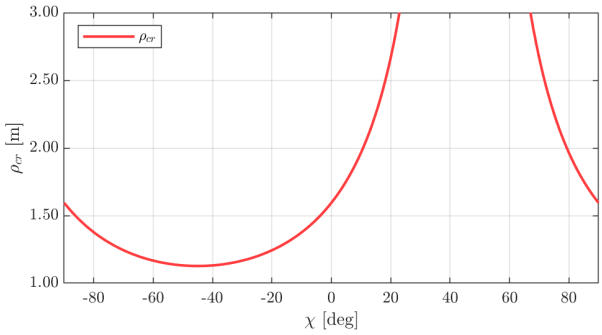

Figure 4.25: Influence of the heading angle χ on the boresight crossrange resolution ρ_{cr}.

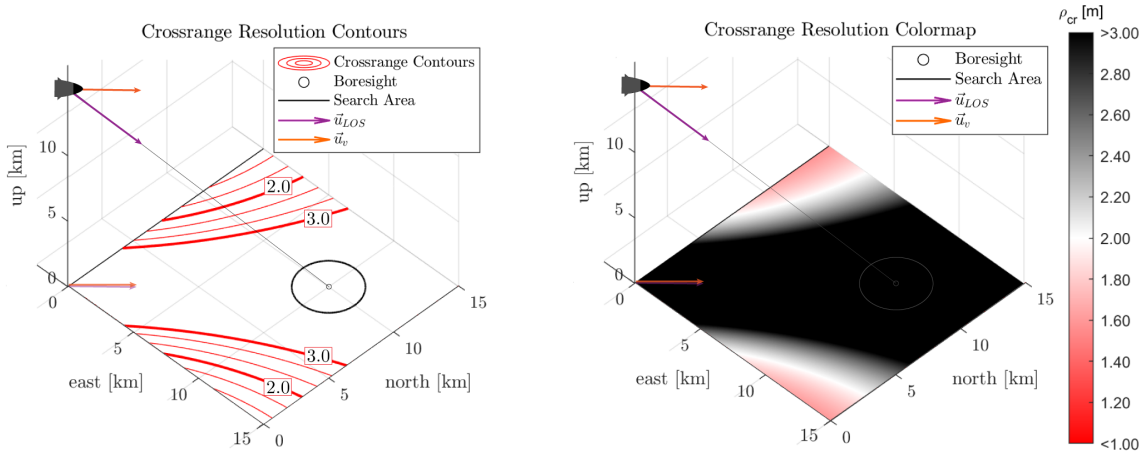

Figure 4.26: (a) Crossrange resolution contours and (b) crossrange resolution colormap for χ = 45.00°.

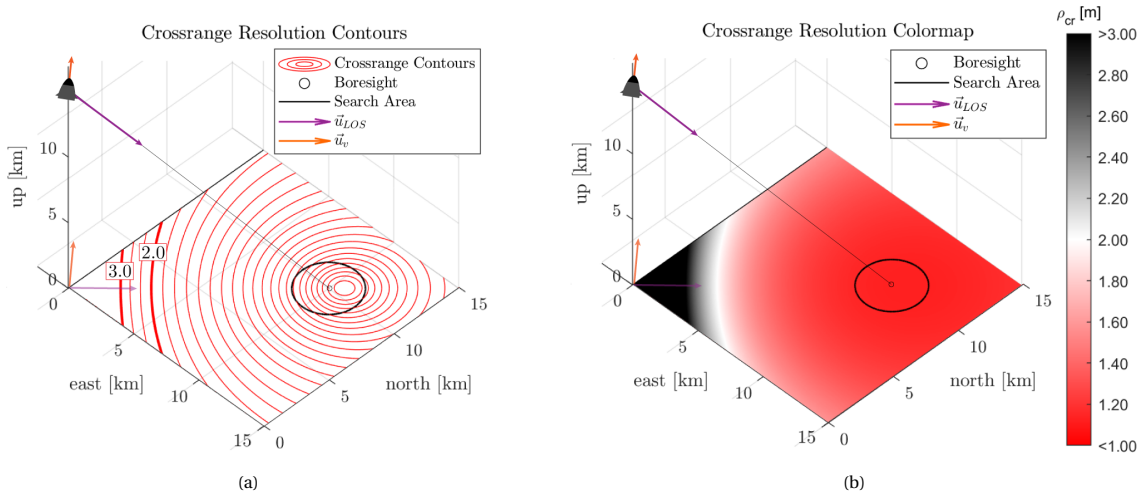

Figure 4.27: (a) Crossrange resolution contours and (b) crossrange resolution colormap for χ = -45.00°.

As illustrated in Figure 4.25, the best crossrange resolution can be obtained for χ = -45.00°, that also follows from Equation (4.21) and the parameters from Table 4.2. Therefore, if the squint angle has the same value as the heading angle, i.e. the radar does not make a horizontal look angle relative to the target, no crossrange resolution can be obtained (ρ_{cr} goes to infinity). In this example, this is the case for χ = 45.00°, since the

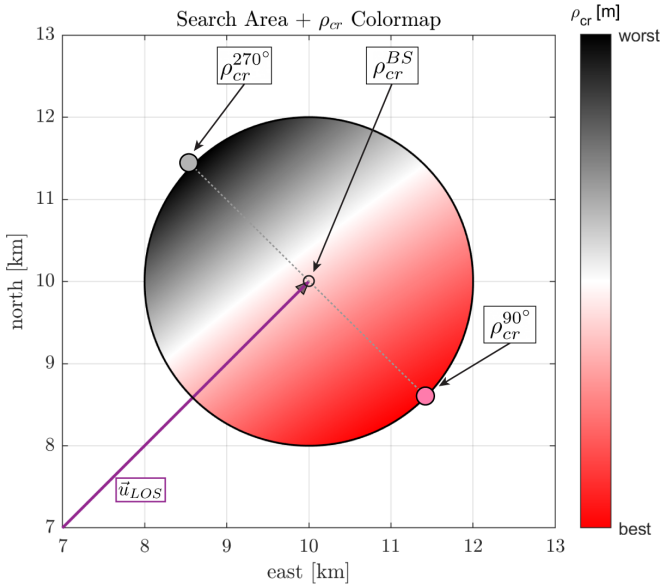

Figure 4.28: Ground range colormap within the search area, including the positions of the best, worst and boresight ground range resolution locations.

squint angle is θ_{sq} = 45.00° as illustrated in Figure 4.26. If the heading angle is perpendicular to the squint angle, χ = -45.00° in this example, the best crossrange resolution can be obtained, as illustrated in Figure 4.27.

In summary, the crossrange resolution, and so the required dwell time to obtain the same value, improves for a higher missile velocity V, dwell times DT, squint angles θ_{sq} and lower slant ranges R, grazing angles ψ_g, flight path angles γ and heading angles χ. However, the optimal values of the latter two variables depends on the geometry between the radar and target.

According to the crossrange resolution colormaps in Figures 4.18b, 4.20b, 4.21b, 4.23b and 4.24b, the best crossrange resolution within the search area is approximately located at the right side relative of $\vec{u}_{LOS}$, while the worst crossrange resolution is located at the left side of $\vec{u}_{LOS}$. The exact locations of these points can not be analytically calculated. The most convenient way is to use the *min()* and *max()* options in MATLAB. However, these options were not yet implemented in the GIANT optimisation tool. Therefore, an approximation of these locations was used in this research. The location corresponding to the best crossrange resolution (having a larger squint angle) is indicated as $\rho_{cr}^{90^\circ}$, while the worst resolution (having a smaller squint angle) is indicated as $\rho_{cr}^{270^\circ}$. The crossrange resolution at the boresight is indicated by ρ_{gr}^{BS}. Note that this approximation only holds if the squint angle is positive. For negative squint angles, the approximation of these locations are mirrored, because the missile will approach the target from the other direction. An overview of these locations are shown in Figure 4.28. To ensure that the ground range resolution constraint of ρ_{cr} = 2.00 m is obtained everywhere in the search area, it is assumed that $\rho_{cr}^{270^\circ}$ should always be lower than 2.00 m:

$$\rho_{cr}^{270^\circ} < 2.00 \text{ m} \tag{4.22}$$

4.4. Target Detectability

This section provides the derivation of equations to obtain the SNR and SCR values as discussed in Section 3.3.3.

4.4.1. Signal-to-Noise Ratio (SNR)

As discussed in Section 3.3.3, the power of the reflected signals of the target have to overcome the background power noise, this ratio is given by the SNR. For a monostatic SAR system, i.e. the same antenna is used for transmission and reception, the received power of a signal reflected by a target can be written as:

$$P_r = \frac{P_p G^2 \lambda_c^2 G_r G_a \sigma_t d_c}{(4\pi)^3 R^4 L_{\text{radar}} L_{\text{atmos}}} \tag{4.23}$$

where P_r is the received power by the antenna, P_p the peak transmitted power by the antenna, G the antenna gain, λ_c the transmitted wavelength, G_r the range processing gain, G_a the crossrange processing gain, σ_t the total target RCS, d_c the duty cycle, R the distance from the antenna to the point target, L_{radar} the radar loss factor and L_{atmos} the atmospheric loss factor. The range processing gain (G_r) is achieved by pulse compression and is given by:

$$G_r = \frac{\tau B}{L_r} \tag{4.24}$$

where τ is the effective pulse width, B the bandwidth of the transmitted signal and L_r the reduction in gain due to non-ideal range filtering, usually $L_r \approx 1.2$ [25]. The crossrange processing gain (G_a) is achieved by coherently integrating the pulses during the CPI and given by:

$$G_a = \frac{N}{L_a} = \frac{DT \times PRF}{L_a} \tag{4.25}$$

where N is the total number of integrated pulses, DT the dwell time, PRF the Pulse Repetition Frequency and L_a the reduction in gain due to non-ideal crossrange filtering, $L_a \approx 1.2$ [25]. As discussed in Section 3.1, the normalised target RCS used in this thesis is σ_t^0 = -10.0 dBm^2/m^2. To obtain the target RCS per resolution cell, this value has to be multiplied by the ground range and crossrange resolution. Since it is assumed that the target is located at the center of the search area [x_t, y_t, z_t], the ground range ρ_{gr}^{BS} and crossrange resolution ρ_{cr}^{BS} at the boresight are used:

$$\sigma_t = \sigma_t^0 \rho_{gr}^{BS} \rho_{cr}^{BS} \tag{4.26}$$

Substituting Equation (4.24)-(4.26) into Equation (4.27) yields:

$$P_r = \frac{P_p G^2 \lambda_c^2 (\tau B)(DT \times PRF) \left(\sigma_t^0 \rho_{gr}^{BS} \rho_{cr}^{BS}\right) d_c}{(4\pi)^3 R^4 L_r L_a L_{\text{radar}} L_{\text{atmos}}} \tag{4.27}$$

The background noise, originating from the radar internal circuits and the environment, is given by [35]:

$$N_0 = k_B T_0 B F_n \tag{4.28}$$

where N_0 is the received background noise, k_B the Boltzmann constant, T_0 the nominal reference temperature, B the bandwidth at the antenna and F_n the noise figure. A nominal reference temperature of T_0 = 290 K and a noise figure F = 4 dB were used. The SNR can be found by dividing the received power of the target by this background noise:

$$SNR = \frac{P_r}{N_0} = \frac{P_p G^2 \lambda_c^2 (\tau)(DT \times PRF) \left(\sigma_t^0 \rho_{gr}^{BS} \rho_{cr}^{BS}\right) d_c}{(4\pi)^3 R^4 (k_B T_0 F_n) L_r L_a L_{\text{radar}} L_{\text{atmos}}} \tag{4.29}$$

Substituting Equation (4.19) for the crossrange resolution ρ_{cr}^{BS} and $d_c = \tau PRF$ according to Equation (4.6), Equation (4.29) becomes:

$$SNR = \frac{P_p G^2 \lambda_c^3 \sigma_t^0 d_c^2 \rho_{gr}^{BS}}{(4\pi)^3 R^3 (k_B T_0 F_n) L_r L_a L_{\text{radar}} L_{\text{atmos}}} \left(\frac{1}{2V \sin(\Xi) \cos(\Lambda)} \right) \tag{4.30}$$

According to Equation (4.30), the SNR is: 1) proportional to the third power of the center wavelength λ_c; 2) proportional to second power of the duty cycle d_c; 3) inversely proportional to the third power of range R and 4) independent of the crossrange resolution.

4.4.2. Signal-to-Clutter Ratio (SCR)

The power of the reflected signals of the target also have to overcome the background power noise originating from the sea clutter, given by the Signal-To-Clutter Ratio SCR. As discussed in Section 3.2, the sea clutter RCS increases for larger grazing angles for vertical polarisations. Therefore, the maximum amount of sea clutter originates from the location at where the -3dB beamwidth hits the surface, $\psi_{\text{g,max}}^{-3\text{dB}}$, as discussed in Section 4.2.3. Therefore, the maximum sea clutter to be considered in the simulation can be calculated by Equation (4.31) with the grazing angle ψ_g replaced by $\psi_{\text{g,max}}^{-3\text{dB}}$. Repeated here for convenience:

$$\begin{aligned} \sigma_{c(H,V)}^0 = c_1 + c_2 log_{10} \sin\left(\psi_{\text{g,max}}^{-3\text{dB}}\right) + \frac{\left(27.5 + c_3 \cdot \psi_{\text{g,max}}^{-3\text{dB}}\right) log_{10}(f)}{(1 + 0.95\psi_{\text{g,max}}^{-3\text{dB}})} \\ + c_4 \cdot (1 + SS)^{\frac{1}{2 + 0.085\psi_{\text{g,max}}^{-3\text{dB}} + 0.033SS}} + c_5 \left(\psi_{\text{g,max}}^{-3\text{dB}}\right)^2 \end{aligned} \tag{4.31}$$

Note that at this location of $\psi_{\text{g,max}}^{-3\text{dB}}$, the ground range and cross range resolution also needs to be redefined to $\rho_{gr,max}^{-3\text{dB}}$ and $\rho_{cr,max}^{-3\text{dB}}$ to:

$$\rho_{\text{gr,max}}^{-3\text{dB}} = \frac{c}{2B \cos\left(\psi_{\text{g,max}}^{-3\text{dB}}\right)} \tag{4.32}$$

$$\rho_{\text{cr, max}}^{-3\text{dB}} = \frac{\lambda R_{\text{min}}^{-3\text{dB}}}{2V(DT) \sin(\Xi) \cos(\Lambda_{\text{max}}^{-3\text{dB}})} \tag{4.33}$$

with $\Lambda_{\text{max}}^{-3\text{dB}}$ given by:

$$\Lambda_{\text{max}}^{-3\text{dB}} = \cos^{-1}\left[\sin(\psi_{\text{g,max}}^{-3\text{dB}}) \cos(\theta_{sq}) \sin(\gamma) \cos(\chi) + \sin(\theta_{sq}) \sin(\psi_{\text{g,max}}^{-3\text{dB}}) \sin(\gamma) \sin(\chi) + \cos(\psi_{\text{g,max}}^{-3\text{dB}}) \cos(\gamma)\right] \tag{4.34}$$

Note that the horizontal look angle Ξ does not need to be redefined since the squint angle of the location at $\psi_{\text{g,max}}^{-3\text{dB}}$ equals the squint angle at the ψ_g. Like the derivation of the SNR, the received power from the clutter can eventually be expressed as:

$$P_{r,clutter} = \frac{P_p G^2 \lambda_c^2 (\tau B) \sqrt{DT \times PRF} \left(\sigma_c^0 \rho_{\text{gr,max}}^{-3\text{dB}} \rho_{\text{cr,max}}^{-3\text{dB}}\right) d_c}{(4\pi)^3 \left(R_{\text{min}}^{-3\text{dB}}\right)^4 L_r L_a L_{\text{radar}} L_{\text{atmos}}} \tag{4.35}$$

Note that in this equation, the crossrange processing gain is $G_a = \frac{\sqrt{DT \times PRF}}{L_a}$. This is due to the assumption that the sea clutter is not coherently added up during the dwell time DT. This originates from the Poisson distribution, where the standard deviation of the noise equals the square root of the signal energy. Therefore, a longer DT improves the signal power compared to the noise power. The SCR defines the ratio of the signal power relative to the clutter and is given by:

$$SCR = \frac{P_r}{P_{r,clutter}} = \frac{\left(R_{\text{min}}^{-3\text{dB}}\right)^4 \sqrt{DT \times PRF} (\sigma_t^0 \rho_{gr}^{BS} \rho_{cr}^{BS})}{R^4 \left(\sigma_c^0 \rho_{\text{gr,max}}^{-3\text{dB}} \rho_{\text{cr,max}}^{-3\text{dB}}\right)} \tag{4.36}$$

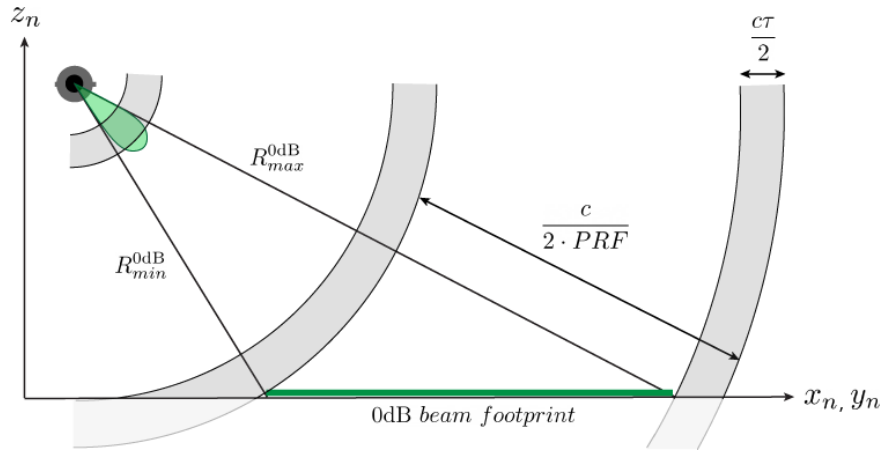

Figure 4.29: The echo from the far edge of the 0dB beam footprint should be received before the echo from the near edge of the next pulse to avoid range ambiguity. The sidelobes of the radar antenna are neglected.

4.5. Radar Ambiguities

An important constraint of the SAR seeker is related to its Pulse Repetition Frequency PRF. To avoid ambiguities in range and Doppler, the PRF is bounded by an upper and a lower limit. This section provides the equations related to these limits, commonly known as range and azimuth ambiguity. Finally, a short description is given about the nadir echo.

4.5.1. Range Ambiguity

In order to distinguish received pulses from another, they should not be received at the same time. Therefore, the echo from the far edge of the 0dB beam footprint, at $R_{\text{max}}^{0\text{dB}}$, should be received before the echo from the near edge $R_{\text{min}}^{0\text{dB}}$ of the next pulse as illustrated in Figure 4.29. This requirement only holds if the sidelobes of the antenna are neglected, i.e. the reflected signals from closer ranges than the 0dB beamwidth are not taken into account. To avoid this ambiguity in range, it is necessary that the Pulse Repetition Interval T is greater than:

$$T_{\text{min}} > \frac{2\left(R_{\text{max}}^{0\text{dB}} - R_{\text{min}}^{0\text{dB}}\right)}{c} = PRF_{\text{max}} \tag{4.37}$$

This translates to an upper limit for the PRF:

$$PRF < PRF_{\text{max}} \tag{4.38}$$

4.5.2. Azimuth Ambiguity

The lower limit of the PRF is related to the maximum Doppler shift of the return signals. Targets ahead of the boresight return higher Doppler shifts, while targets behind the boresight return lower Doppler shifts. The range of these frequencies is known as the Doppler bandwidth B_D and is given by [36]:

$$B_D = \frac{4V}{\lambda_c} \cos(\Omega) \sin\left(\frac{\beta_{0\text{dB}}}{2}\right) \tag{4.39}$$

where V is the absolute velocity of the missile, λ_c the center wavelength, Ω the total angle between $\vec{u}_v$ and $\vec{u}_{LOS}$ and $\beta_{0\text{dB}}$ the 0dB beamwidth. The PRF should be greater than the Doppler bandwidth to avoid Doppler aliasing. Therefore, the lower limit of the PRF is given by:

$$PRF > B_D = PRF_{\text{min}} \tag{4.40}$$

4.5.3. Nadir Echo

The nadir is referred as the point on the Earth's surface directly below the radar. The nadir echo is the reflected signal from this point and is generally generated by one of the sidelobes of the beam. In the process of radar design, the nadir echo is an often used parameter to avoid interference with the signals registered by the mainlobe. The frequency of the nadir echos (PRF_{nadir}) is given by:

$$PRF_{\text{nadir}} = \frac{c}{2z} \tag{4.41}$$

where z is the altitude of the radar. The PRF can be designed such, that the nadir echo is exactly registered during the receive window, i.e. the PRF should equal PRF_{nadir} or natural numbers multiplications of this value. Because the sidelobes of the radar are neglected in this research, this constraint is also ignored. However, the PRF_{nadir} is still given to provide additional information for the radar design engineer.

5

Trajectory Optimisation

This chapter provides an introduction into the optimal control problem. First, the definition of the optimal control problem is given in Section 5.1. In Section 5.2, a description of the GIANT optimisation tool, objectives and a summary of the constraints are provided. Finally, in Section 5.3, an introduction into the scaling factors will be given.

5.1. Definition of the Optimal Control Problem

As discussed in Chapter 3, a minimum ground range and crossrange resolution of 2.00 m and a SNR and SCR of 20.00 dB are required for target acquisition. This acquisition will be performed by SAR. In this research, the objectives are to minimise the dwell time DT of the SAR seeker in order to limit the amount of defocus, the exposure time of the missile t_{end} and the maximisation of its vertical end velocity $V_{\text{D,end}}$. More details about these objectives will given in Section 5.2.2.

As discussed in Section 4.3.1, the ground range resolution can be obtained by flying at a certain altitudes (i.e. grazing angles, depending on the ground range to the target). However, at lower altitudes, the atmosphere has a significant higher density resulting in higher drag forces. Hence, the absolute velocity decreases faster at these altitudes, that directly relates to the vertical end velocity objective. Therefore, it is desired to fly at higher altitudes during the acquisition phase. In Section 4.3.2, it was shown that the crossrange resolution can only be obtained if the heading angle has not the same value as the squint angle, i.e. the SAR seeker requires a horizontal look angle with the target. This means that the missile has to diverge from its shortest time of flight trajectory, that increases the total exposure time objective. According to Section 4.4.1, the SNR is inversely proportional to the third power of the slant range. Therefore, it is desired to start the acquisition phase at the shortest slant range possible. However, the acquisition of the target has to be completed before the terminal guidance phase, i.e. accomplished at a certain range from the target to allow the missile to manoeuvre itself to the target. As discussed in Section 4.4.2, the SCR improves for higher dwell times, but the objective is to minimise this dwell time. Finally, as discussed in Section 4.5, the SAR seeker is constrained to the lower and upper boundary of the PRF, that depends on the slant range, the missile's velocity and the squint angle.

To satisfy the objectives, the constraints related to the missile's manoeuvrability, the imaging requirements for the acquisition of a target and the constraints of SAR, the trajectory can be optimised. This can be achieved by finding the optimal controls for the dynamic model, that are the angular velocities p, q and r. These

optimised variables manoeuvre the missile to its optimal trajectory. This trajectory provides an insight into the limitations and achievable performances of this application of SAR for the chosen parameters.

5.2. Optimisation Tool

5.2.1. GIANT

The GIANT optimisation software, developed and provided by TNO, was used for this research. GIANT uses the Pseudo-Spectral Collocation method to transform a continuous problem into a finite-dimensional discrete Nonlinear Programming (NLP) problem [37]. The algorithm used for solving this problem is a combination of three methods: Sequential Quadratic Programming (SQP), the trust-region method and the interior-point method. The combined algorithm has the same form of SQP, meaning that the problem is solved iteratively. The first iteration starts with a user-defined approximation of the optimal values for solving the objective function. Then, the algorithm replaces the objective function by a quadratic approximation. The solution to this approximation is used in the next iteration to construct a better approximation. This process is repeated until a sequence of approximations converges to a solution. To prevent the quadratic approximation of the objective function to become worse during the iteration process, the trust-region method is applied. This method defines a region around the current solution in which the quadratic approximation of the objective function can extent. The size of this region changes for every iteration depends on the improvement of the approximation. The interior-point method is applied to let the SQP handle inequality constraints. A detailed description of these algorithms used can be found in [38] and [39]. A description of the combined algorithm used in GIANT can be found in [18]. An unique feature of GIANT is its ability to automatically generate the analytical Jacobian and Hessian.

GIANT allows to have multiple phases (trajectory parts) that are separated by boundaries. The constraints can apply to individual or several phases and/or boundaries. Besides variables, parameters can be defined that are sets of values that stay constant during the optimisation process. Examples of these parameters are the antenna gain, beamwidth or the target RCS. For the optimisation, a total of three phases have been chosen as shown in Figure 5.1. The first phase defines the re-entry phase. This phase describes the optimal re-entry trajectory, before the start of second phase: the target acquisition phase/SAR phase. The initial conditions of the missile apply to the start of the re-entry phase and first boundary (1). The second boundary (2) defines the position at the end of the re-entry phase and start of the SAR phase. The SAR phase describes the optimal trajectory to perform SAR for target acquisition. Boundary (3) defines the position between the end of the SAR phase and the start of the last phase: the terminal guidance phase. In this last phase the missile is guided to its end position: boundary (4).

The optimal control problem is formulated by an objective function, a cost function, F, which is to be minimised (or maximised) and given by:

$$F(t,\mathbf{T},\mathbf{x}(t),\mathbf{u}(t),\mathbf{V}) = \Psi(\mathbf{T},\mathbf{x}(t),\mathbf{u}(t),\mathbf{V}) + \int_{t_0}^{t_e} \Phi(t,\mathbf{x}(t),\mathbf{u}(t),\mathbf{V})\,dt \tag{5.1}$$

where t is the time, $\mathbf{T}$ the values of t at the boundaries of the phases, $\mathbf{x}$ the state variables, $\mathbf{u}$ the control variables and $\mathbf{V}$ the design variables. The objective function is subject to the dynamics $\mathbf{f}$:

$$\dot{\mathbf{x}}(t) = \mathbf{f}(\mathbf{x}(t),\mathbf{u}(t),\mathbf{V}) \tag{5.2}$$

The optimisation problem may contain equality constraints $\mathbf{c}_E$ and inequality constraints $\mathbf{c}_I$:

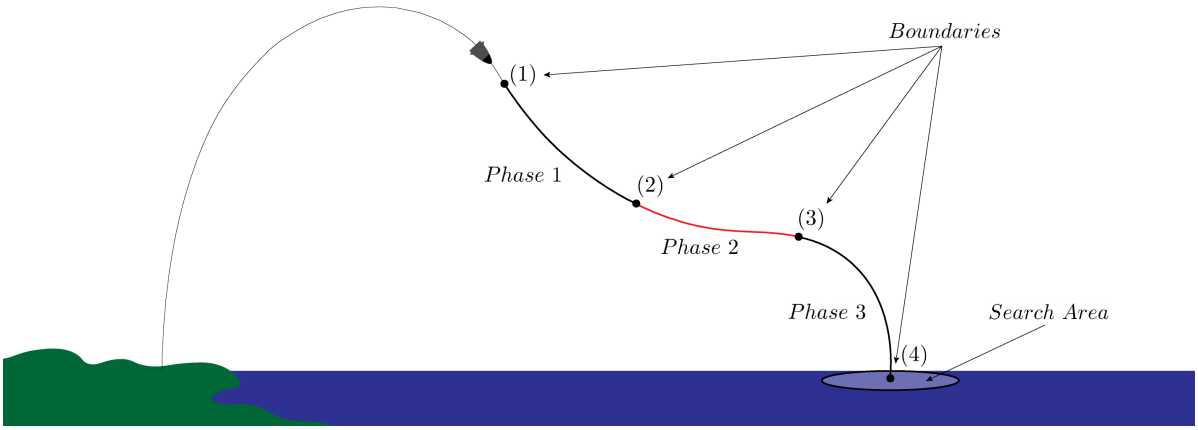

Figure 5.1: 2D view of the optimisation setup. The optimisation consists of 3 phases and 4 boundaries. Phase 1: re-entry, Phase 2: target acquisition (SAR) and Phase 3: terminal guidance.

$$\begin{aligned} \mathbf{c}_E(t,\mathbf{T},\mathbf{x}(t),\mathbf{u}(t),\mathbf{V}) &= 0 \\ \mathbf{c}_I(t,\mathbf{T},\mathbf{x}(t),\mathbf{u}(t),\mathbf{V}) &\geq 0 \end{aligned} \tag{5.3}$$

The cost function is composed of the Mayer term Ψ and a Lagrange term Φ. The former term is a function of the variables at the boundaries. This term is calculated at the end of every iteration and added to the total cost function. The latter term is an integral over the span of t from the initial time value t_0 to the end time value t_e.

The state variables $\mathbf{x}$ were discussed in Chapter 2. The control variables $\mathbf{u}$ are the angular velocities p, q and r. In addition, the dwell time DT is also set as a control variable because it is a continuous function of time during the acquisition phase and part of the cost function. Finally, the PRF is set as a design variable $\mathbf{V}$, since it is not a function of time and chosen to be constant during the acquisition phase. The PRF has to be higher than the minimum PRF to prevent range ambiguity and lower than the maximum PRF to prevent Doppler ambiguity as discussed in Section 4.5.

5.2.2. Cost Function

The cost function defines the overall performance of the SAR seeker and the missile. In this thesis, three different performance indicators have been chosen:

- Minimisation of the Dwell Time (DT)
  In this research, it is assumed that a target is stationary. However, in real world applications, the target is moving with an unknown speed and direction. A more detailed explanation of the behaviour of moving targets in SAR data can be found in [40]. In summary, a target with a motion component in the range direction causes a displacement of the target in the SAR images, while a motion component in the crossrange direction causes the target to be defocused in this direction. These effects can be compensated to some extent by post-processing algorithms, but the theory behind this is beyond the scope of this thesis. The amount of defocus in a target in a SAR image is proportional to the dwell time [41]. Therefore, to improve the acquisition of a target in real world applications, it is desired to reduce the amount of defocus by minimizing the dwell time. In addition, it is desired to complete the acquisition and identification of a target as fast as possible. However, longer dwell times improve the SCR. Therefore, a trade-off has to be made during the trajectory optimisation that minimises the dwell time, but still satisfies the target acquisition constraints.

- Minimisation of the exposure time (t_{end})
  To decrease the chances of anti-missile systems to operate, it is desired to minimise the exposure time of the missile. Therefore, the end time of the entire trajectory should to be minimised.
- Maximisation of the vertical end velocity ($V_{\text{D,end}}$)
  To maximise the effectiveness of the missile, the impact angle and velocity should be maximised. These two variables are related to each other by the end velocity in the down-direction, i.e. the vertical end velocity.

The dwell time DT is added to the Lagrange term Φ, because this value has to be minimised over time. The exposure time t_{end} and the vertical end velocity $V_{\text{D,end}}$ are added to the Mayer term Ψ since they are bounded to boundary (4).

5.2.3. Constraints

The constraints have been discussed in Chapters 2, 3 and 4. A summary of these constraints are provided here. Most of the constraints were chosen based on the expertise of TNO experts and others on values found in literature. During the trajectory, the missile and SAR seeker are bounded to the following constraints:

1) Limited angle-of-attack:
   The angle-of-attack may not exceed -25° and 25° to prevent the missile to be in stall:

$$-25^\circ < \alpha < 25^\circ \tag{5.4}$$

2) Minimum resolution:
   As discussed in Section 3.3.2, a minimum resolution of 2.00 m x 2.00 m has to be achieved everywhere within the search area. This translated to:

$$\rho_{gr}^{180^\circ} < 2.00 \text{ m} \tag{5.5}$$

$$\rho_{cr}^{270^\circ} < 2.00 \text{ m} \tag{5.6}$$

3) Minimum SNR and SCR:
   As discussed in Section 3.3.3, a minimum SNR and SCR of 20.00 dB have to be achieved of the target:

$$SNR > 20.00 \text{ dB} \tag{5.7}$$

$$SCR > 20.00 \text{ dB} \tag{5.8}$$

4) Maximum seeker look angle:
   As discussed in Section 4.2.3, the maximum SAR seeker look angle may not exceed 45° to avoid the antenna to operate behind its physical limit:

$$\zeta < 45^\circ \tag{5.9}$$

5) Minimum acquisition phase time:
   Any actual acquisition and localisation process of a target were not taken into account in this research. Therefore, the exact required time for the identification of a target is a complex problem, scenario dependent and beyond the scope of this thesis. However, a minimum required time for the acquisition phase had

Initial Conditions of the missile			
$[x_i, y_i, z_i]$	Initial Position	[0.00, 0.00, 60.00]	km
$[\phi_0, \theta_0, \psi_0]$	Initial Euler Angles	[0.00, -30.00, 45.00]	deg
V_0	Initial Velocity	3500.00	m/s
γ_0	Initial Flight Path Angle	-30.00	deg
χ_0	Initial Heading Angle	45.00	deg

Table 5.1: Missile and related parameters used in the optimisation.

to be chosen. In consultation with TNO experts, a value of 3.00 s was used, corresponding to a constraint between boundary (2) and (3) by:

$$T_{(2)\rightarrow(3)} > 3.00 \text{ s} \tag{5.10}$$

This value was chosen based on the following considerations: 1) typical dwell time values for obtaining crossrange resolution of about ρ_{cr} = 2.00 m, range from 0.3-0.5 s [24] and [26]; 2) the target acquisition might require more than one SAR image; 3) the acquisition of a target requires computational time and 4) the entire search area might not be completely mapped in one SAR image due to a limited beamwidth.

6) Minimum range for terminal guidance:
After the acquisition phase has been completed, the missile should guide itself to the target within the pre-defined search area of 2.00 km. This range should be sufficient to allow the missile to manoeuvre to its target, but still within the capabilities of the homing mode of the radar. In consultation with TNO experts, this range is assumed to be 15.00 km, corresponding to a constraint between boundary (3) and (4) by:

$$R_{(3)\rightarrow(4)} > 15.00 \text{ km} \tag{5.11}$$

Larger sized search areas would require a higher value for $R_{(3)\rightarrow(4)}$, because in that case the missile requires a sharper turn to guide itself towards a target possibly located the edge of the search area.

5.2.4. Initial and Final Conditions

Since this research focuses on the optimisation of the acquisition phase of an ASBM, the boost and midcourse phase of the missile were not taken into account. Hence, the initial conditions of the missile were set to common short range ASBM re-entry conditions. These conditions were chosen in consultation with TNO experts and are summarised in Table 5.1. A heading angle of χ = 45.00° was used for improving the visualisation of the trajectory in 3D (i.e. the missile has a velocity component in the North- and East-direction).

The end position of the missile should match to the location of the target. As mentioned before, it is assumed that the target is located at the center of the search area. One possible scenario is that this location equals the impact location of the uncorrected ballistic trajectory of the missile. While this is unlikely to be the case in real world scenarios, it is an interesting location to be used for the end conditions because the optimised manoeuvres of the missile could be visualised and compared easily to this uncorrected trajectory.

The impact location was found to be approximately [67.00, 67.00, 0.00] km for the initial conditions as given in Table 5.1 by a MATLAB ODE45 integration. The uncorrected ballistic trajectory and the missile position variables are illustrated in Figure 5.2.

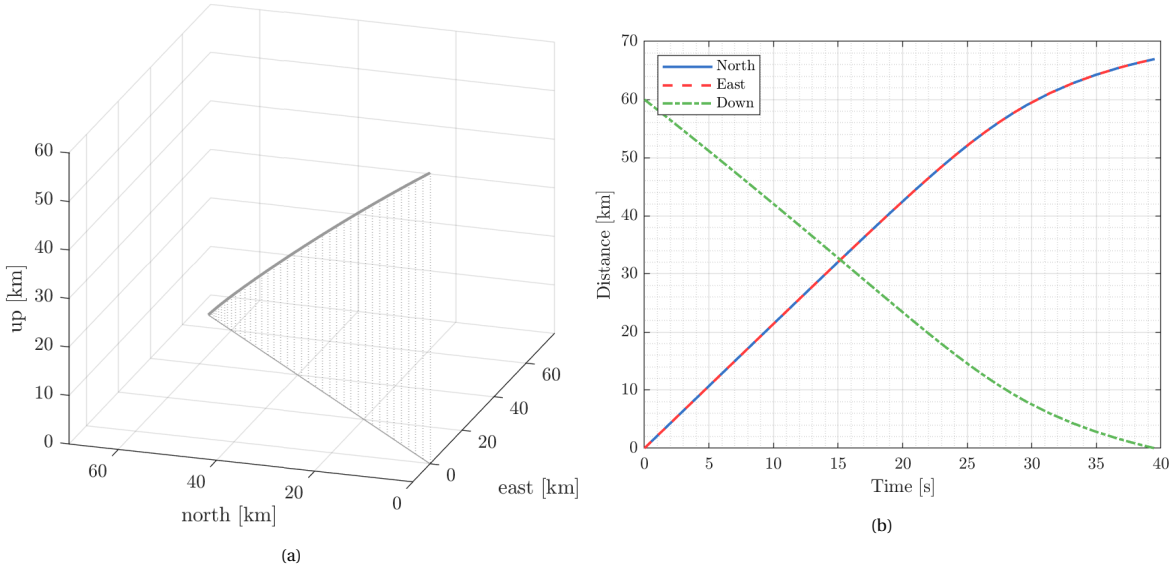

Figure 5.2: (a) 3D view of the ballistic trajectory from an altitude of 60 km with lift and drag. (b) The position in the North- (x), East- (y) and Down-directions (z).

5.3. Scaling Factors

The optimisation tool needs to be tuned in order to program the precedence of the objectives. This is be achieved by adding user-defined scaling factors to the cost function. In addition, a scaling factor was also used for the control variable p, q and r because they have to be smooth and be within reasonable limits for realistic input into the autopilot of the missile. Without penalizing these variables, the graph for these optimised values may contain jitter. To avoid this, these variables can be penalized by adding p^2, q^2 and r^2 to the Lagrange cost term [18]. Therefore, the Mayer and Lagrange terms have the following forms:

$$\Phi = \Gamma_{\text{pqr}} \left[p^2 + q^2 + r^2 \right] + \Gamma_{\text{DT}} DT \tag{5.12}$$

$$\Psi = \Gamma_{t_{\text{end}}} t_{\text{end}} + \Gamma_{V_{\text{D,end}}} V_{D,end} \tag{5.13}$$

where Γ_{pqr} is the scaling factor for the angular velocities, Γ_{DT} the scaling factor for the dwell time, $\Gamma_{t_{\text{end}}}$ the scaling factor for the exposure time and $\Gamma_{V_{\text{D,end}}}$ the scaling factor for the vertical end velocity. The desired ratios can be found by repeating the optimisation process with different scaling factors values and plotting the corresponding performance indicators in a Pareto plot, as illustrated in Figure 5.3. The Pareto plot provides a quick overview of how different scaling factors influence the performance indicators. The selection of the optimal set of scaling factors is a choice by the engineer and is scenario dependent. For instance, the engineer may set higher precedence to the vertical end velocity compared to the average dwell time. However, in this research, the optimal solution is chosen to be the point closest to the interception of the asymptotes of the Pareto plot. This means that the performance indicators all have the same precedence. This ratio of scaling factors generates a trajectory with an equal compromise between the lowest DT and t_{end}, and highest $V_{\text{D,end}}$-values.

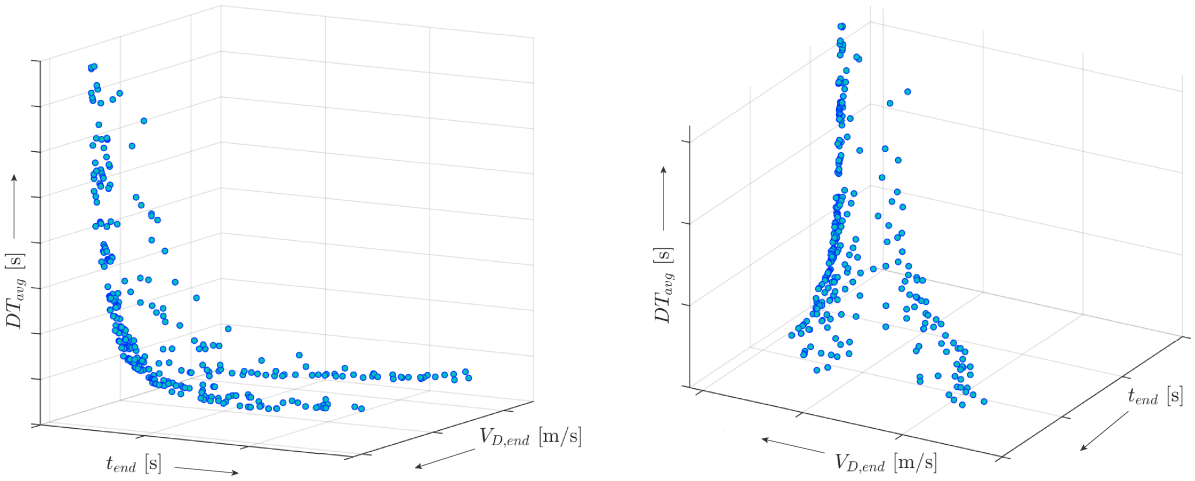

Figure 5.3: Pareto plot example of the influences of the scaling factors on the performance.

6

Verification and Validation

This chapter provides the verification and validation of the optimisation input model. The atmospheric and aerodynamic models were not validated since these were part of GIANT provided by TNO. The equations of motion are verified by a comparison of analytical calculated data and the output of a pre-defined simulation in Section 6.1. In addition, the resolution equations are verified the same way as given in Section 6.2.

6.1. Equations of Motion

The following simulations were performed: 1) free fall without lift and drag and 2) ballistic flight without lift and drag.

6.1.1. Free Fall without Lift and Drag

In this example the lift and drag forces were set to zero. The flight path angle was set to γ = -90.00°, corresponding to a velocity in pointing straight in the Down-direction. The other used initial conditions are summarised in Table 6.1.

Free fall initial conditions

$[x_0, y_0, z_0]$	Initial position	[0.00, 0.00, 60.00]	km
$[\phi_0, \theta_0, \psi_0]$	Initial Euler angles	[0.00, 0.00, 0.00]	deg
$[\gamma_0, \psi_0]$	Initial flight path angle and heading angle	[-90.00, 0.00]	deg
V_0	Initial absolute velocity	0.001	m/s

Table 6.1: Chosen initial conditions for a free fall trajectory verification.

Since the constant gravity is the only acceleration acting on the missile, the free fall time can be calculated. The distance traveled in the Down-direction (z) can be calculated by:

$$\ddot{z} = g_0 \tag{6.1a}$$

$$\dot{z} = g_0 t - V_{z0} \tag{6.1b}$$

$$z = g_0 \frac{t^2}{2} - V_{z0} t + z_0 \tag{6.1c}$$

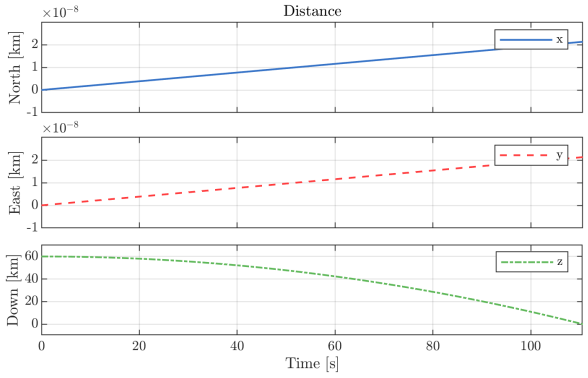

(a) The North (x), East (y) and Down (z) distances.

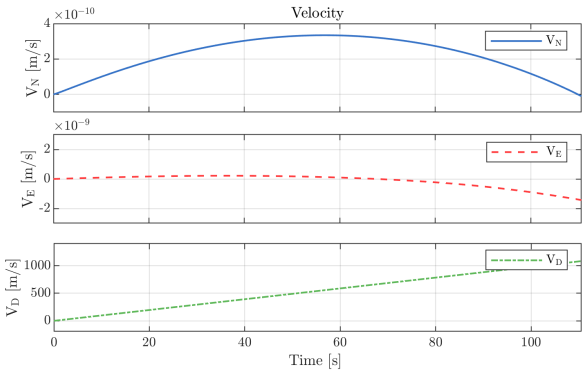

(b) The North (V_N), East (V_E) and Down (V_D) velocities.

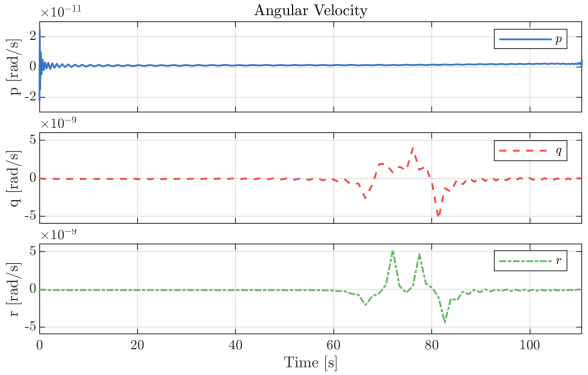

(c) The roll (p), pitch (q) and yaw (r) rate.

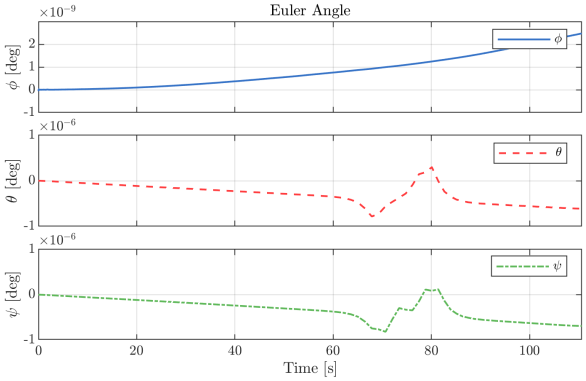

(d) The roll (ϕ), pitch (θ) and yaw (ψ) angles.

Figure 6.1: The (a) distances, (b) velocities, (c) angular velocities and (d) Euler angles for the free fall simulation.

With $V_{z0} = V_0 \sin(\gamma_0)$ and rewriting Equation (6.1), the time of flight from an initial altitude z_0 is given by:

$$t_{\text{TOF}} = \frac{-V_0 \sin(\gamma_0) + \sqrt{(V_0\ sin(\gamma_0))^2 + 2g_0(z_0 - z)}}{g_0} \tag{6.2}$$

With the initial values from Table 6.1 and a constant gravity of $g_0 = 9.81\ \text{m}/s^2$, a time of flight of $t_{\text{TOF}} = 110.60$ s was found. The end velocity in the down-direction can be calculated by:

$$V_{\text{D,end}} = V_0 \sin(\gamma_0) + g_0 t_{\text{TOF}} \tag{6.3}$$

With $t_{\text{TOF}} = 110.60$ s, an end velocity in the Down-direction of $V_{D,end} = 1085.00$ m/s was found. Figure 6.1 shows the results for the distances, velocities, angular velocities and Euler angles for a free fall trajectory without lift and drag.

Based on the Figures, the motion of the missile follows a free fall motion as expected, i.e. does not move in the North- and East-direction as shown in Figure 6.1a. However, all values that were expected to be constant still show fluctuating values during the trajectory. The magnitude of these influences are in the range of 10^{-6} to 10^{-10}. Therefore, their effect have been neglected for the optimisation process. An altitude of $z = 0.00$ km is reached after 110.5993 s, which matches the expected value. The velocity in the Down-direction (V_D) increases linearly due to the constant gravity to an end velocity of $V_D = 1085.00$ m/s as shown in Figure 6.1b, which also matches the expected value. Figure 6.1c and 6.1d show that the equations related to the Euler angles are implemented correctly, since the graphs correspond to the initial Euler angles of 0.00°.

Ballistic flight initial conditions			
$[x_0, y_0, z_0]$	Initial position	[0.00, 0.00, 60.00]	km
$[\phi_0, \theta_0, \psi_0]$	Initial Euler angles	[0.00, 0.00, 0.00]	deg
$[\gamma_0, \psi_0]$	Initial flight path angle and heading angle	[0.00, 0.00]	deg
V_0	Initial absolute velocity	3500.00	ms^{-1}

Table 6.2: Chosen initial conditions for a ballistic flight verification.

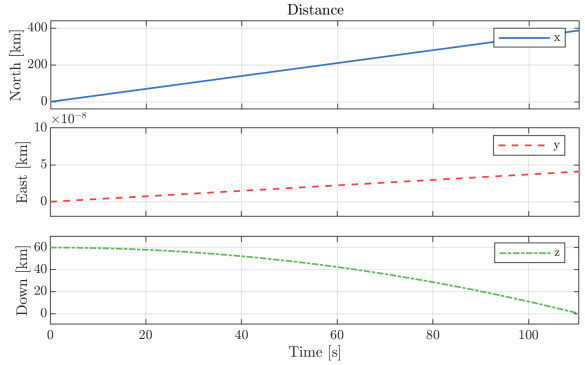

(a) The North (x), East (y) and Down (z) distances.

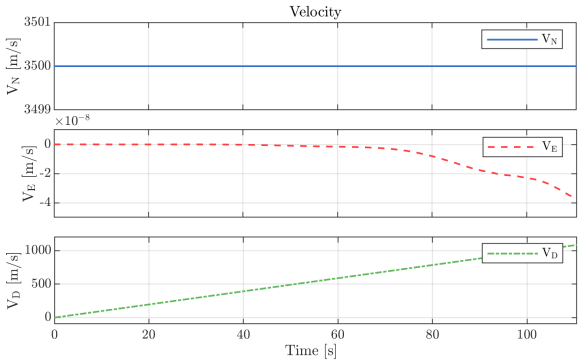

(b) The North (V_N), East (V_E) and Down (V_D) velocities.

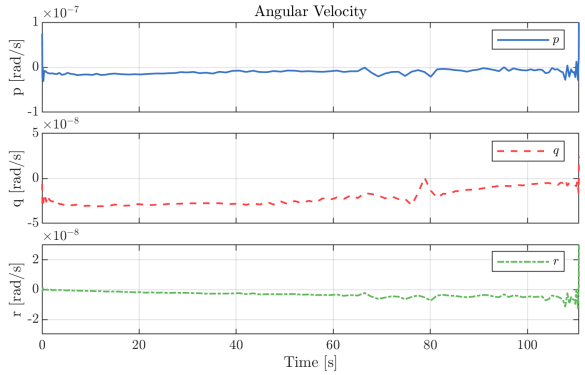

(c) The roll (p), pitch (q) and yaw (r) rate.

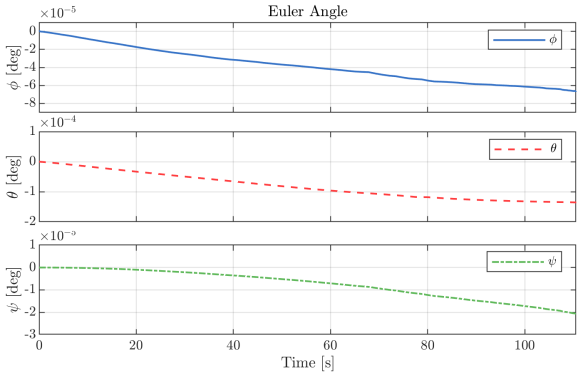

(d) The roll (ϕ), pitch (θ) and yaw (ψ) angles.

Figure 6.2: The distances (a), velocities (b), angular velocities (c) and Euler angles (d) for the ballistic flight simulation.

6.1.2. Ballistic Flight without Lift and Drag

In this example the lift and drag forces were also set to zero. The flight path angle was set to $\gamma = 0.00°$ with a velocity in the North-direction of $V_N = 3500.00$ m/s. The other used initial conditions for this example are summarised in Table 6.2.

Like the simulation for the free fall, a time of flight of $t_{TOF} = 110.60$ s and end velocity in the Down-direction of $V_D = 1085.00$ m/s were found. With a flight path angle of $\gamma = 0.00°$, the missile has a horizontal velocity component pointing in the North-direction of $V_N = V_0 \cos(\gamma_0)$. The corresponding horizontal displacement can be calculated by:

$$x = V_0 \cos(\gamma_0)\, t_{TOF} \tag{6.4}$$

With a time of flight of $t_{TOF} = 110.60$ s, a horizontal displacement of $x = 387.10$ km was found. Figure 6.2 shows the results for the distances, velocities, angular velocities and Euler angles for a ballistic flight without lift and

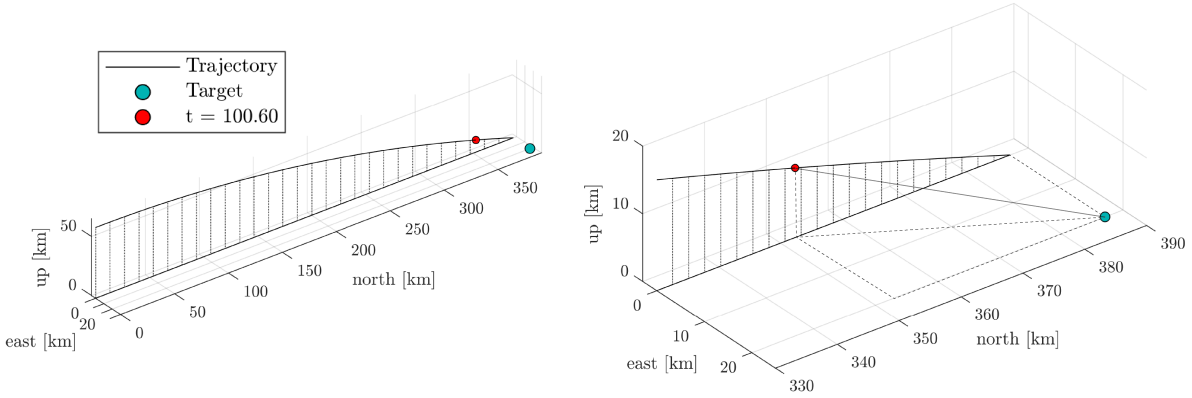

Figure 6.3: 3D view, including close-up, of the ballistic flight with a target.

drag. Based on the Figures, the motion of the missile follows a ballistic flight as expected. The final position obtained by the simulation was [387.10, 0.00, 0.00] km after 110.5993 s. An end velocity in the Down-direction of V_D = 1085.00 m/s was also found as shown in Figure 6.2b. These values match the expected values. Figures 6.2c and 6.2d show negligible fluctuations that range from 10^{-4} to 10^{-8}.

6.2. Resolution Equations

In this section the implementation of equations related to the ground range and crossrange resolutions are verified. The initial conditions of Table 6.2 are also used for this example. A target is located at [387.10, 20.00, 0.00] km, i.e. 20.00 km in the East-direction relative to the missile's final position of [387.10, 0.00, 0.00] km. The ground range and crossrange resolutions can analytically be calculated by Equation (4.14) and (4.19), repeated here for convenience:

$$\rho_{gr} = \frac{c}{2B\cos(\psi_g)} \tag{6.5}$$

$$\rho_{cr} = \frac{\lambda_c R}{2V(DT)\sin(\Xi)\cos(\Lambda)} \tag{6.6}$$

In order to calculate these resolutions, the grazing angle ψ_g, range R, absolute velocity V, horizontal look angle Ξ and vertical look angle Λ are required. A bandwidth of B = 150 MHz, center transmitted wavelength of λ_c = 0.03 m and dwell time DT = 0.40 s are assumed for this example. Furthermore, the resolutions will be calculated at t = 100.60, i.e. 10 seconds before impact of t_{TOF} = 110.60 s. This location is illustrated in Figure 6.3.

According to Equation (6.3), at t = 100.60 s, a velocity in the Down-direction was found to be V_D = 986.89 m/s. The velocities in the North- and East-direction are constant with V_N = 3500.00 m/s and V_E = 0.00 m/s. The position in the Down-direction can be calculated according to Equation (6.1): z = 10.36 km. The position in the East-direction is zero and the position in the North-direction can be calculated with Equation (6.4): x = 352.10 km. With these values, the required variables in Equation (6.5) and (6.6) can be calculated by Equations (4.5), (4.2), (2.25), (4.20) and (4.21) respectively. These answers are summarised in Table 6.3 and provides a ground range and crossrange resolution of ρ_{gr} = 1.03 m and ρ_{cr} = 0.86 m. Figure 6.4 shows the results for the distances-to-go, range, velocities, squint and grazing angle and the horizontal and vertical look angles for a ballistic trajectory without lift and drag with a target at [387.10, 20.00, 0.00] km.

Calculated variables at t = 100.60					
t [s]	ψ_g [deg]	R_s [m]	V [m/s]	Ξ [deg]	Λ [deg]
100.60	14.40	41.40	3636.66	29.92	7.81

Table 6.3: Required variables at t = 100.60 from a ballistic trajectory without lift and drag for calculating the resolutions.

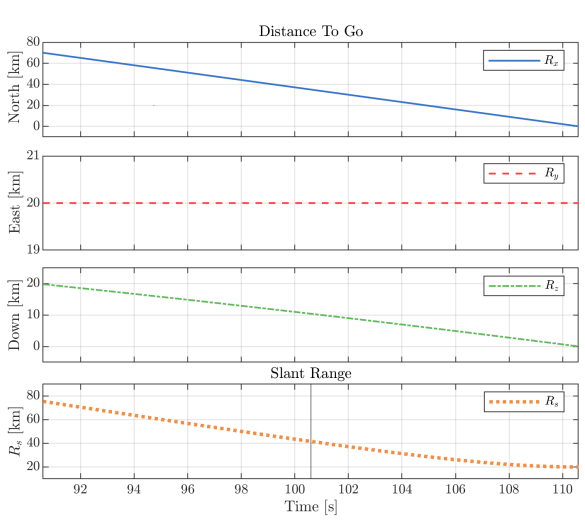

(a) The North (x), East (y), Down (z) distances and slant range R_s.

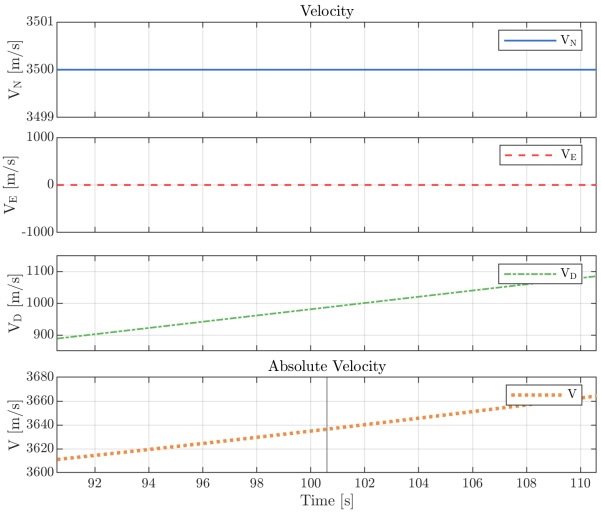

(b) The North (V_N), East (V_E) and Down (V_D) velocities and the absolute velocity (V).

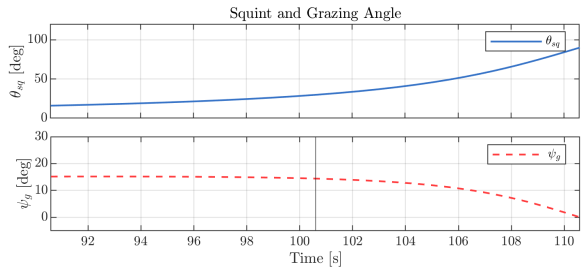

(c) The squint (θ_{sq}) and grazing angle (ψ_g).

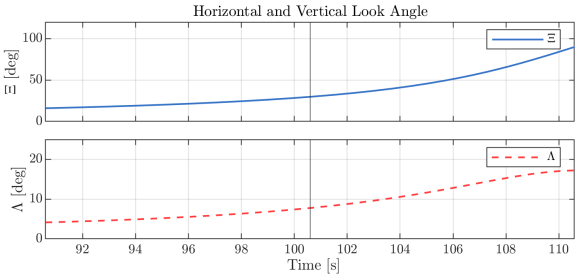

(d) The horizontal (Ξ) and vertical (Λ) look angles.

Figure 6.4: The (a) distances-to-go, (b) velocities, (c) squint and grazing angles and (d) the horizontal and vertical look angles for the ballistic flight simulation.

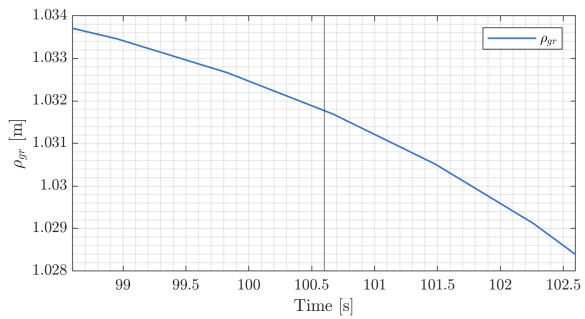

(a)

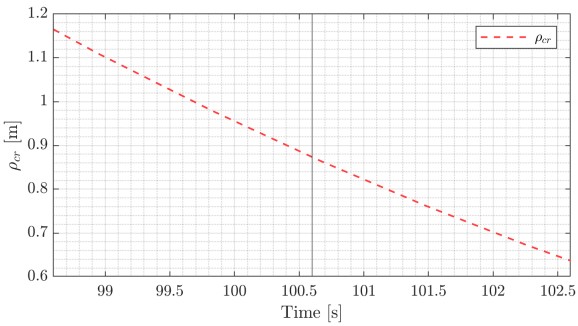

(b)

Figure 6.5: (a) The ground range ρ_{gr} and (b) crossrange ρ_{cr} resolutions for the ballistic flight simulation.

The intersection of the graphs with the vertical line at t = 100.60 s are identical as the values determined in Table 6.3. The corresponding ground range and crossrange resolutions are shown in Figure 6.5. At t = 100.60 s, the simulation found a ground range and cross range of 1.0317 m and 0.8639 m respectively. Both values match the expected values. Therefore, the resolution values seem to be calculated correctly.

7

Results and Discussion

This chapter provides the results and discussion of the optimised trajectories. In Section 7.1, an overview of the assumptions that were being made is given. The used parameters and constraints are summarised in Section 7.2. The chosen scaling factors are discussed in Section 7.3. In Section 7.4, the results of the optimal trajectory for fixed initial conditions are given. This trajectory is compared with the trajectory for optimised initial conditions in Section 7.5. Finally, a resolution limitation analysis is conducted to investigate the maximum obtainable resolutions for the chosen parameters of the SAR seeker in Section 7.6.

7.1. Assumptions

The following assumptions were made:

- The Earth is flat, non-rotating and the gravity is constant.
- The missile is a rigid model.
- There is no sideslip acting on the missile.
- The sightline and trajectory reference frames share the same z-axis.
- The origins of the sightline and body reference frames coincide.
- The search area location is known before re-entry.
- The target is located at the center of the predefined search area.
- The Doppler shifts induced by the motion of the target are neglected.
- The target acquisition is completed within 3.00 s of SAR.
- The atmosphere is free of clouds and hazy atmospheric circumstances.
- The SAR seeker performance is not influenced by re-entry heating.
- The boresight of the antenna stays pointed at the same ground location.
- The sidelobes of the antenna beam are neglected.
- The sea is the only contributing factor to the clutter.
- The clutter is incoherent during the dwell time.

7.2. Overview of the used Parameters, Constraints and Constants

An overview of the chosen parameters for the SAR seeker, missile and target are given in Tables 7.1-7.3. The used constants are provided in Table 7.4 and the constraints are summarised in Table 7.5.

SAR seeker			
λ_c	Wavelength of transmitted signal	0.03	m
f_c	Center frequency of transmitted signal	10.0	GHz
A_a	Physical area of the antenna	0.09	m^2
η_{ap}	Aperture efficiency of the antenna	70	%
G	Antenna gain	29.44	dB
P_p	Peak Power	1000	W
B	Transmitted bandwidth	150	MHz
d_c	Duty cycle	10	%
$\beta_{-3\text{dB}}$	-3dB beamwidth	6.00	deg
$\beta_{0\text{dB}}$	0dB beamwidth	12.00	deg
Pol	Polarisation	Vertical	-
T_0	Effective noise temperature	290	K
F	Noise figure	4	dB
L_{radar}	Radar loss	2	dB
L_{atmos}	Atmospheric loss	1	dB
L_{gr}	Loss in gain compression	20	%
L_{az}	Loss in azimuth compression	20	%
r_{search}	Search area radius	2.00	km
SS	Sea state	4	-

Table 7.1: SAR seeker and related parameters used in the optimisation.

Missile			
$[x_i, y_i, z_i]$	Initial position	[0.00, 0.00, 60.00]	km
$[\phi_0, \theta_0, \psi_0]$	Initial Euler angles	[0.00, -30.00, 45.00]	deg
V_0	Initial velocity	3500.00	m/s
γ_0	Initial flight path angle	-30.00	deg
χ_0	Initial heading angle	45.00	deg
β_0	Ballistic coefficient	6000	kg/m^2
$C_{L\alpha}$ / C_{d0}	Relative lift derivative to zero-lift drag coefficient ratio	65	-

Table 7.2: Missile and related parameters used in the optimisation.

Target			
$[x_t, y_t, z_t]$	Position	[67, 67, 0]	km
σ_0^t	Normalised target RCS per m^2	-10.0	dBm^2

Table 7.3: Target parameters used in the optimisation.

Constants			
c	Speed of light	2.997×10^8	m/s
g_0	Gravitational acceleration	9.81	m/s^2
k	Boltzmann constant	1.381×10^{-23}	m^{2}kg/ s^{2}K

Table 7.4: Constants used in the optimisation.

Constraints	
-25° < α < 25°	Angle-of-attack
$[x_m(t_e), y_m(t_e), z_m(t_e)] = [x_t, y_t, z_t]$	End Position
$\zeta < 45°$	Antenna look angle
$\rho_{gr}^{180°} <$ 2.00 m	Range resolution
$\rho_{cr}^{270°} <$ 2.00 m	Crossrange resolution
SNR > 20.00 dB	Signal-to-Noise Ratio
SCR > 20.00 dB	Signal-to-Clutter Ratio
$T_{(2)\rightarrow(3)} >$ 3.00 s	SAR phase period
$R_{(3)\rightarrow(4)} >$ 15.00 km	Terminal guidance phase length
$PRF_{\min} < PRF < PRF_{\max}$	Pulse Repetition Frequency

Table 7.5: Summary of the constraints used in the optimisation.

7.3. Choice of Scaling Factors

First of all, the scaling factor Γ_{pqr} for the control variables p, q and r was determined. It is desired to have a scaling factor as low as possible to minimise the penalization, but still have a high enough scaling factor to avoid jitter. The optimal scaling factor was determined by modifying its magnitude until no jitter was present as suggested in the GIANT manual. A scaling factor of $\Gamma_{\text{pqr}} = 1000$ was found that provided the control variables p, q and r to be smooth. This value was kept constant for all optimisation runs.

Subsequently, the optimal scaling factors for $\Gamma_{V_{\text{D,end}}}$, $\Gamma_{t_{\text{end}}}$ and Γ_{DT} were determined by a Pareto plot. A total of 8 scaling factors were chosen for each of these individual scaling factors. These values were determined by modifying their magnitudes such that the performance indicator values would be normalised relative to each other. Relatively high values were also included to investigate their influence on the trajectory and to help finding the asymptotes in the Pareto plot. The following values for the scaling factors were used:

$\Gamma_{V_{\text{D,end}}}$ = [0.1 0.5 5 50 250 500 750 1250]
$\Gamma_{t_{\text{end}}}$ = [0.1 0.5 5 50 250 500 750 1250]
Γ_{DT} = [100 1000 5000 7500 10000 15000 20000 30000]

Therefore, a total of $8^3 = 512$ trajectories were generated. The corresponding cost function values are shown in Figure 7.1. The asymptotes in this Figure are at approximately $V_{\text{D,end}} = 1133.00$ m/s, $t_{\text{end}} = 38.12$ s and $DT_{\text{avg}} = 0.088$ s.

Summary Scaling Factors		
Γ_{pqr}	Scaling factor for p, q and r	1000
$\Gamma_{\text{V}_{\text{D,end}}}$	Scaling factor for $V_{\text{D,end}}$	50
$\Gamma_{\text{t}_{\text{end}}}$	Scaling factor for t_{end}	750
Γ_{DT}	Scaling factor for DT	7500

Table 7.6: Used scaling factors used in the optimisation for fixed initial conditions.

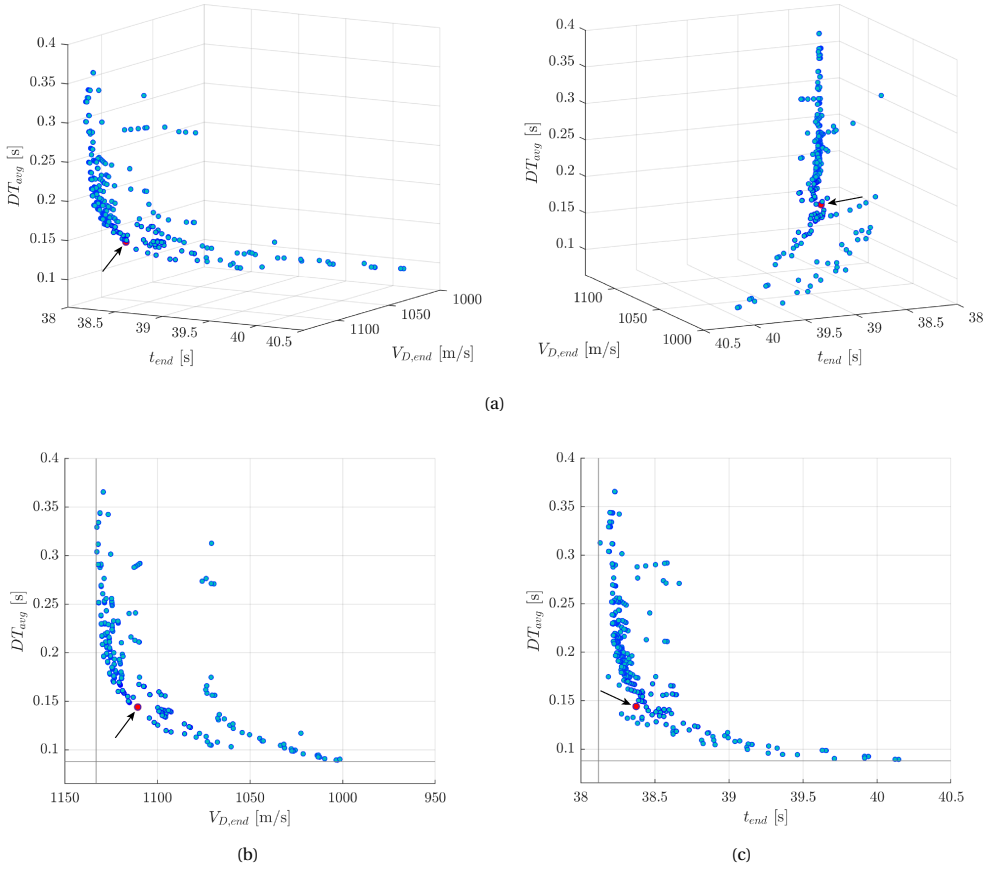

Figure 7.1: Pareto plot generated for different scaling factors for $\Gamma_{V_{\text{D,end}}}$, $\Gamma_{\text{t,end}}$ and Γ_{DT}. (a) Pareto plot in 3D from two different view angles. (b) 2D view for $V_{\text{D,end}}$ and DT_{avg}. (c) 2D view for t_{end} and DT_{avg}. Red dot represents the selected set of scaling factors.

The optimal set of the scaling factors depends on the choice of the engineer. It might be that a higher exposure time with an average dwell time, e.g. t_{end} = 40.00 s and DT_{avg} = 0.09 s, is preferred over a lower exposure time with a higher average dwell time, e.g. t_{end} = 38.50 s and DT_{avg} = 0.15 s. This also applies to the comparison of the vertical end velocity with the average dwell time and exposure time. For the sake of convenience, it is assumed that all of the performance values have the same precedence. This corresponds to the nearest point relative to the interception of the asymptotes (i.e. the trajectory having the relatively best end velocity, shortest exposure time and lowest average DT). The scaling factors corresponding to this trajectory are provided in Table 7.6 and have the following performance indicator values: $V_{\text{D,end}}$ = 1110.60 m/s, t_{end} = 38.37 s and DT_{avg} = 0.1441. This trajectory is discussed in the next section.

7.4. Optimal Trajectory for Fixed Initial Conditions

Figure 7.2 shows the re-entry, acquisition and terminal guidance phases in 3D with the ballistic trajectory from Section 5.2.4 as reference.

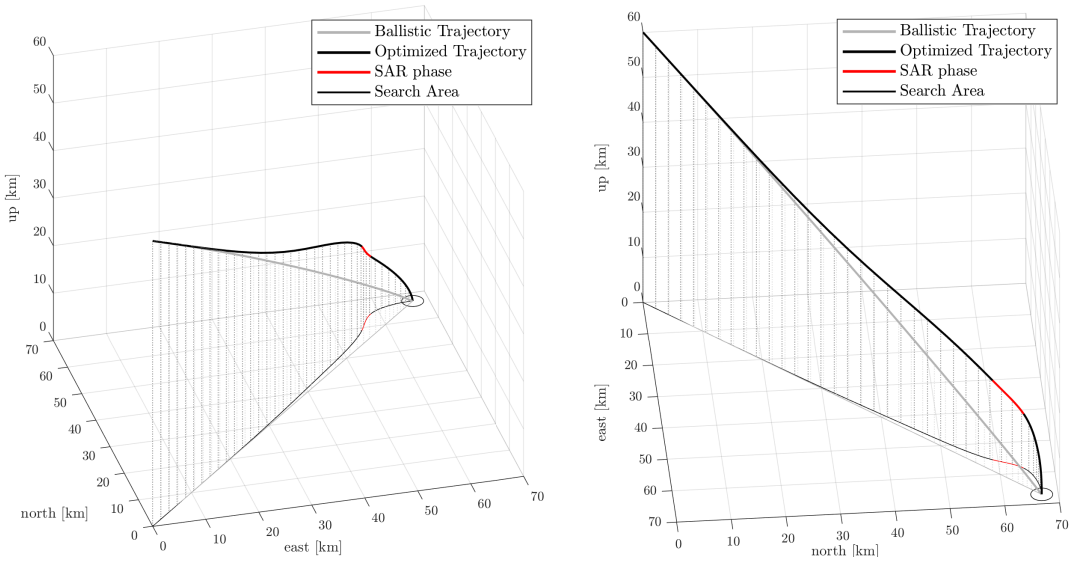

Figure 7.2: The optimised trajectory for the parameters from Tables 7.1-7.5. The ballistic trajectory is shown as a reference.

Compared to the ballistic trajectory, the optimised trajectory shows that the missile manoeuvres itself to satisfy the constraints. The first part of the re-entry phase of the ballistic and optimised trajectory are similar, but at a certain range from the target, the missile manoeuvres more into the North-direction, that increases its squint angle. The corresponding data for the optimised trajectory for various variables are provided in Figures 7.3-7.10.

Figure 7.3 shows the slant range R_s and the missile's coordinates in the North (x), East (y) and Down (z) directions. The final position of the missile is [67.00, 67.00, 0.00] km, meaning that the missile hits the target. The SAR phase starts at a slant range of R_s = 22.63 km and ends at R_s = 15.00 km. Therefore, the terminal guidance phase length constraint of $R_{(3)\rightarrow(4)}$ was satisfied. During the SAR phase the missile descends from an altitude of z = 17.63 km to z = 12.06 km, allowing to obtain a sufficient grazing angle for the required ground range resolution.

The grazing angle ψ_g and squint angle θ_{sq} are shown in Figure 7.4. During the SAR phase, the grazing angle ranges from $\psi_g = 51.21°$ to $\psi_g = 53.34°$. These values are below the grazing angle limit as discussed in Section 4.3.1: for a bandwidth of B = 150 MHz, the grazing angle may not exceed 60.00°, otherwise a ground range resolution better than ρ_{gr} = 2.00 m can not be obtained. The squint angle gradually increases from its initial value of θ_{sq} = 45.00° to θ_{sq} = 55.78° at the start of the SAR phase. During the SAR phase, the squint angle shows an increase to θ_{sq} = 73.40°. Due to this increasement, a larger horizontal look angle Ξ can be achieved that improves the crossrange resolution as shown in Figure 7.5. This allows the required dwell time DT to be minimised, as discussed in Section 3.3.1.

The flight path angle γ and heading angle χ are shown in Figure 7.6. As discussed in Section 3.3.1, the crossrange resolution can be improved for negative flight path angles, while its optimal value depends on the geometry between the missile and target. Because the flight path angle was already negative during its re-entry, the flight path angle shows a negligible change during the SAR phase. The final flight path angle, that corresponds to the impact angle that directly relates to the vertical end velocity $V_{\text{D,end}}$, has a value of γ = -85.43°. In contrast to the squint angle that gradually increases, the heading angle gradually decreases from its initial value of χ_0 = 45.00° to χ = 28.60° at the start of the SAR phase. This allows the horizontal look angle Ξ to become even larger, that allows the dwell time to be even shorter to obtain the same crossrange resolution. During the SAR phase, the heading angle changes back to a larger value, namely χ = 45.27°, to eventually manoeuvre the missile towards the target.

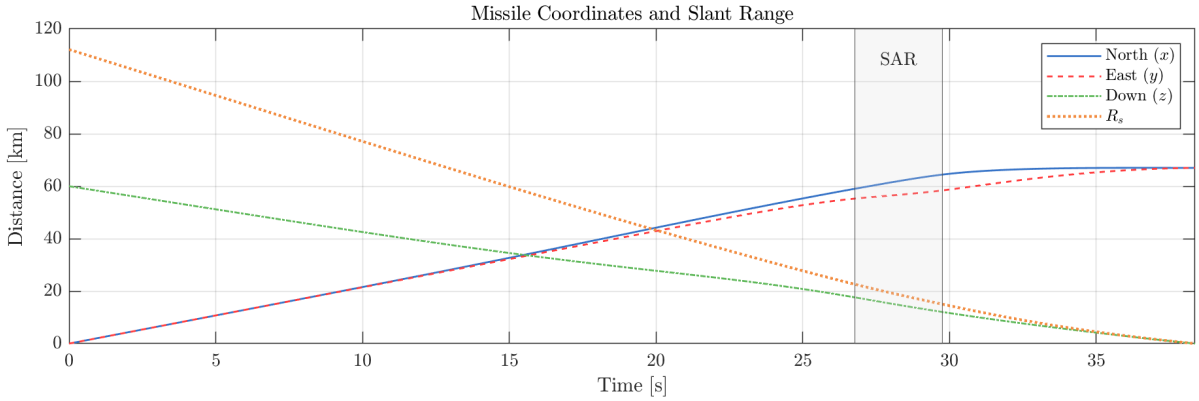

Figure 7.3: The missile coordinates in the North- (x), East- (y) and Down-directions (z) and slant range R_s.

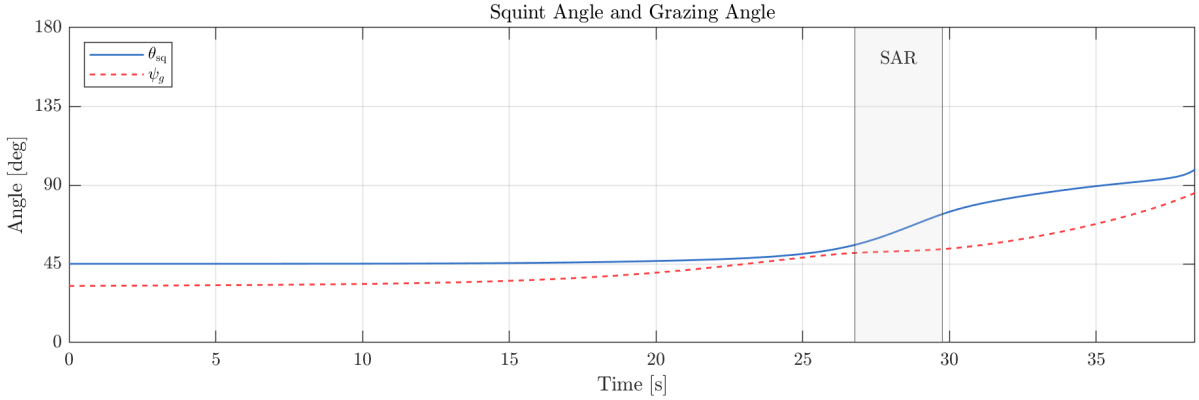

Figure 7.4: The squint angle θ_{sq} and grazing angle ψ_g.

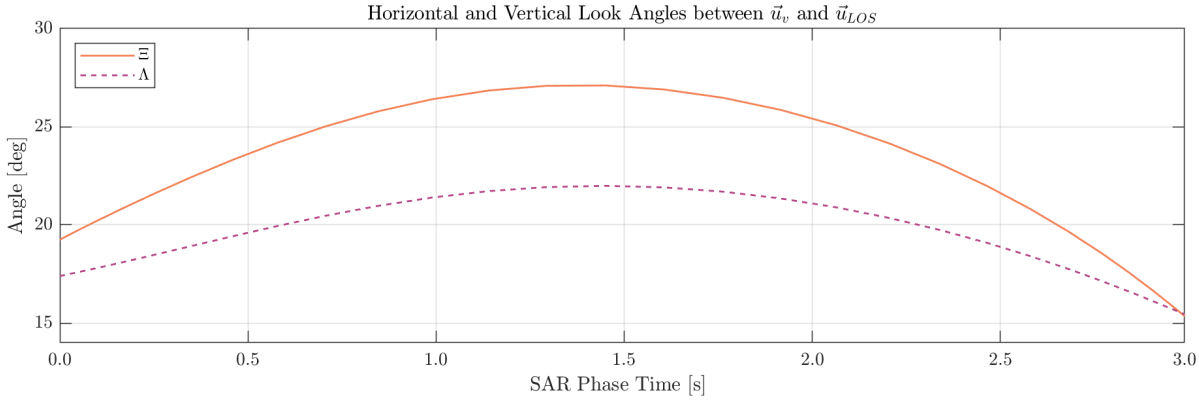

Figure 7.5: The horizontal Ξ and vertical Λ angles between $\vec{u}_v$ and $\vec{u}_{LOS}$ during the SAR phase.

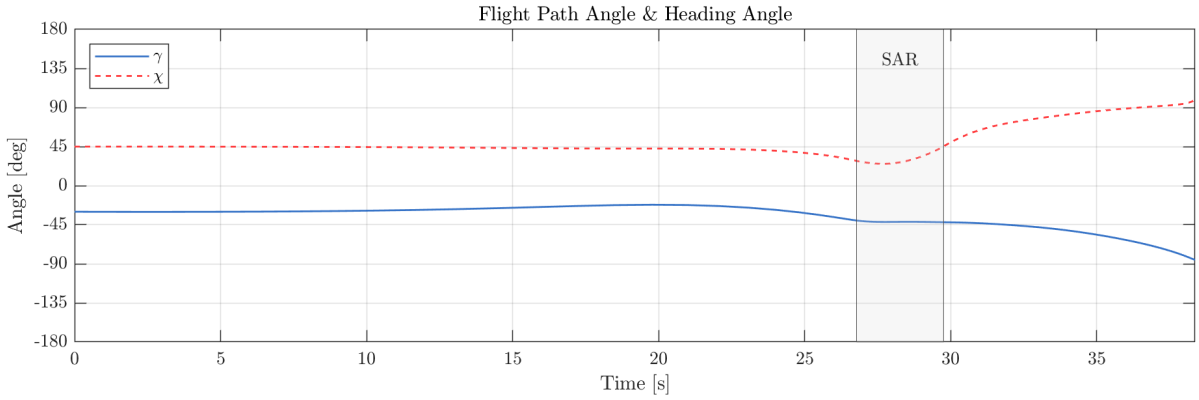

Figure 7.6: The flight path angle γ and heading angle χ.

The velocities in the North-direction V_N, East-direction V_E, Down-direction V_D and the absolute velocity V are shown in Figure 7.7. Compared to the ballistic trajectory, the missile flies longer at higher altitudes before the start of the SAR phase. This prevents the velocity of the missile to decrease less quickly, because the drag forces are lower due to the lower densities at higher altitudes. This results in that the missile has a higher velocity at the start of the SAR phase. Subsequently, higher velocities requires shorter dwell time to obtain the same crossrange resolution. The absolute end velocity is V = 1114.14 m/s. With an impact angle of γ = -85.43°, the vertical end velocity is V_D = 1110.60 m/s. This value corresponds to the actual value of V_D in the Figure.

The optimised angular velocities p, q and r are shown in Figure 7.8. The graphs of these variables are smooth and contain no jitter, resulting from the selected scaling factor Γ_{pqr}. The positive roll rate p in combination with the negative pitch rate q, manoeuvre the missile more into the North-direction before the start of the SAR phase. This results in the higher squint angle as discussed before. The Euler Angles are shown in Figure 7.9. The initial pitch angle of θ_0 = -30.00° increases to approximately θ = -15.50° during the first seconds of the re-entry phase. This is the results of the pitch rate starting at approximately 0.2 rad/s, indicating that the initial pitch angle of the missile was not optimal. This also applies to the roll rate that shows a direct change of its value. However, because the flight path angle stays constant during the first 10 seconds of flight, the increased pitch angle results in an increased angle-of-attack α as shown in Figure 7.10. The graph shows that the constraint of -25° < α < 25° is satisfied.

Figure 7.11 shows a close-up of the SAR phase and terminal guidance phase of the trajectory. The 0dB and 3dB beam footprints at the start of the SAR phase are also shown. In addition, the search area with the ground range and crossrange resolutions distributions are illustrated in Figure 7.11a and Figure 7.11b respectively. The colors show the distributions of the ground range and crossrange resolutions within the search area. A close-up of these beam footprints and search areas are shown in Figure 7.11c and 7.11d respectively.

These latter two Figures show that the 3dB beam footprint does not completely overlay the search area. To avoid this, the radar should scan the complete search area by mechanically or electronically steer the beam during the SAR phase. This would require additional time, but this scenario was already taken into account during the selection of the constraint of 3.00 s for the acquisition phase. The Figures also show that the approximated worst and best ground range and crossrange resolutions are at the expected locations of $\rho_{gr}^{180^\circ}$, $\rho_{gr}^{0^\circ}$, $\rho_{cr}^{270^\circ}$ and $\rho_{cr}^{90^\circ}$. Note that these Figures only shows the beam footprints and resolution distributions at the start of the SAR phase. These values change over time, as shown in Figure 7.12 and 7.13 respectively.

Figure 7.12 shows the ground range resolutions at the nearest, center and furthest locations of the search area relative to the SAR seeker. These locations correspond to the maximum $\rho_{gr}^{180^\circ}$, boresight ρ_{gr}^{BS} and minimum $\rho_{gr}^{0^\circ}$ ground range resolution values, as discussed in Section 3.3.1. The Figure also shows that the ground range resolution at $\rho_{gr}^{180^\circ}$ is always worse (has a higher value) compared to ρ_{gr}^{BS} and $\rho_{gr}^{0^\circ}$. The average values of these locations are: $\rho_{gr}^{180^\circ}$ = 1.85 m, ρ_{gr}^{BS} = 1.63 m and $\rho_{gr}^{0^\circ}$ = 1.30 m. Therefore, the constraint of the minimum ground range resolution of 2.00 m, everywhere within the search, is satisfied.

Figure 7.13 shows the crossrange resolutions at the right, center and left locations of the search area relative to the SAR seeker. These locations correspond to the minimum $\rho_{cr}^{90^\circ}$, boresight ρ_{cr}^{BS} and maximum $\rho_{cr}^{270^\circ}$ crossrange resolution values, as discussed in Section 3.3.1. The crossrange resolution $\rho_{cr}^{270^\circ}$ is always worse (has a higher value) compared to ρ_{cr}^{BS} and $\rho_{cr}^{90^\circ}$. The average values of these locations are: $\rho_{cr}^{270^\circ}$ = 2.00 m, ρ_{cr}^{BS} = 1.52 m and $\rho_{cr}^{0^\circ}$ = 1.25 m. Therefore, the constraint of the minimum crossrange resolution of 2.00 m, everywhere within the search, is satisfied.

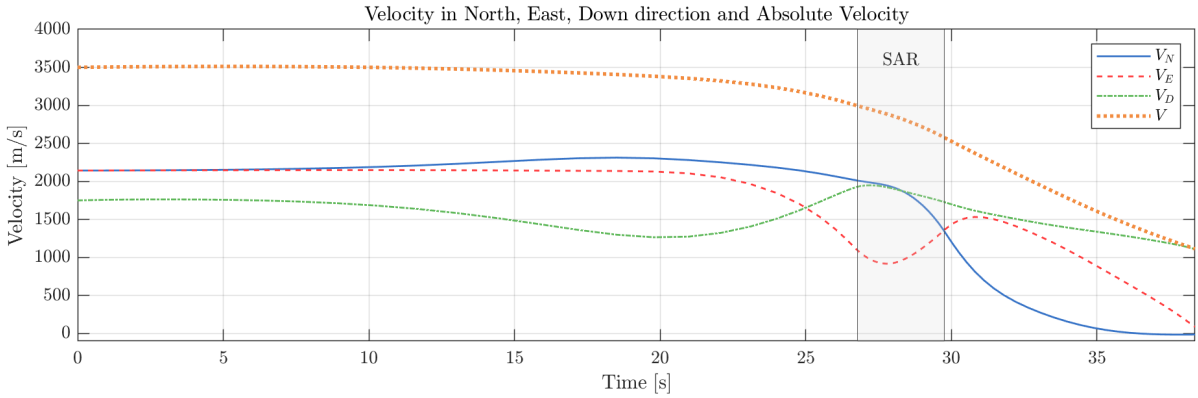

Figure 7.7: The absolute velocity V and velocities in the North- V_N, East- V_E and Down-directions V_D.

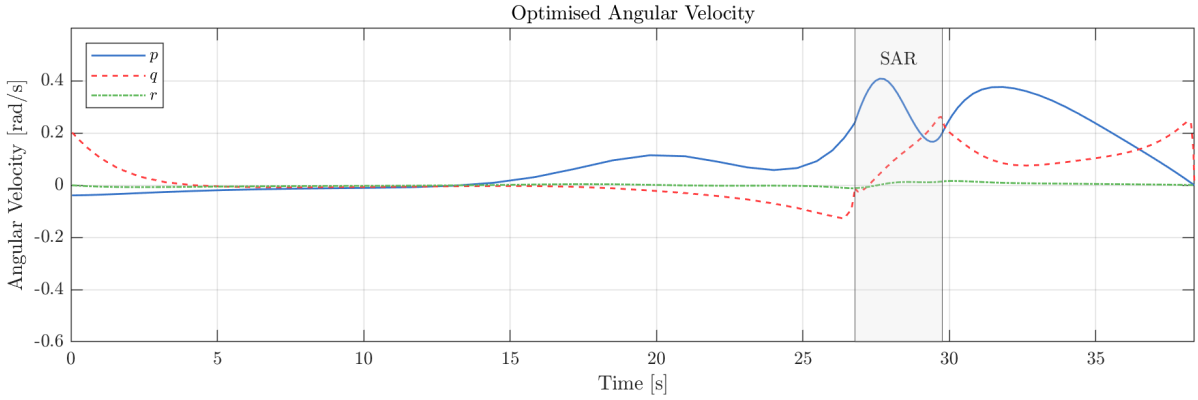

Figure 7.8: The optimised angular velocities p, q and r.

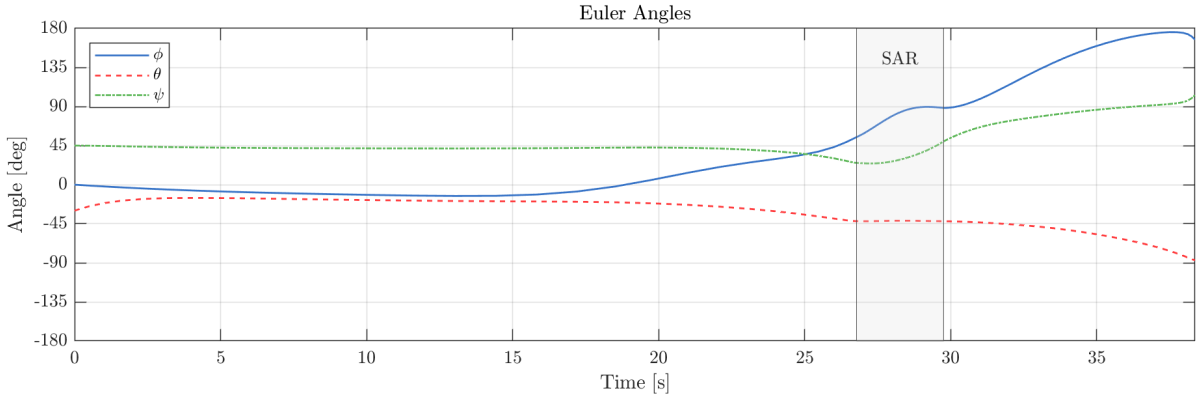

Figure 7.9: The Euler Angles ϕ, θ and ψ.

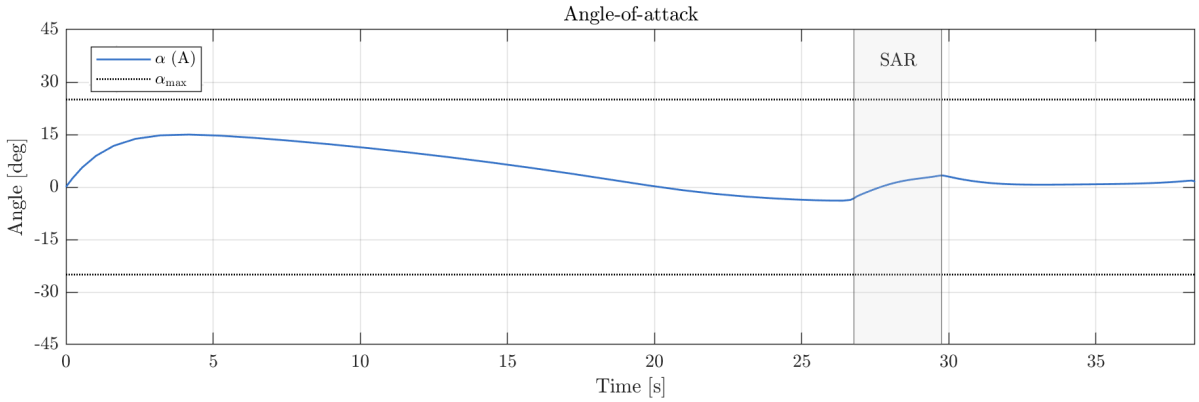

Figure 7.10: The Angle-Of-Attack α and its constraint limit α_{max}.

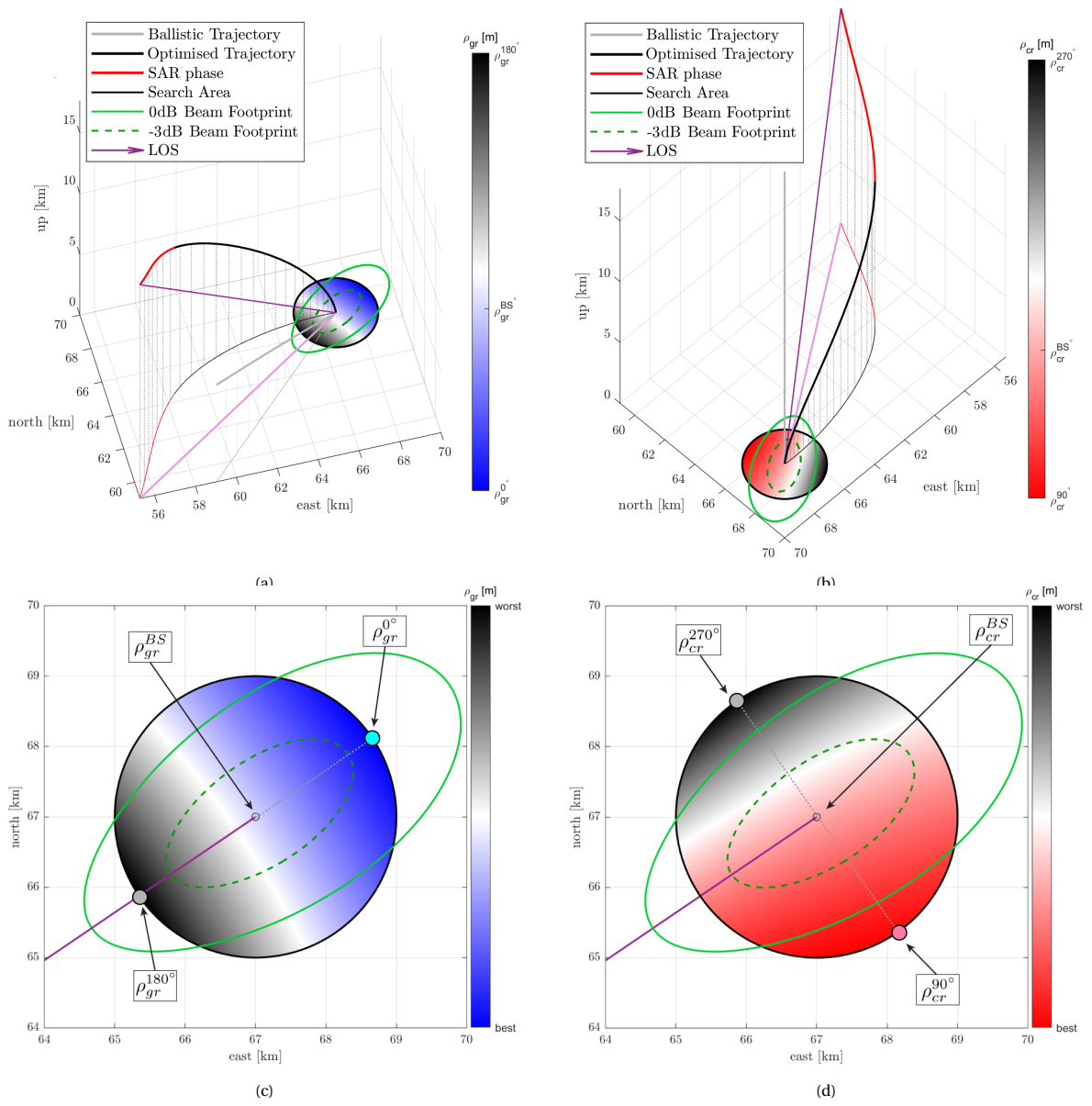

Figure 7.11: The SAR and terminal guidance phase including the beam footprints and (a) ground range and (b) crossrange resolution distributions over the search area. Close-up of the (c) ground range and (d) crossrange resolution distributions and beam footprints over the search area.

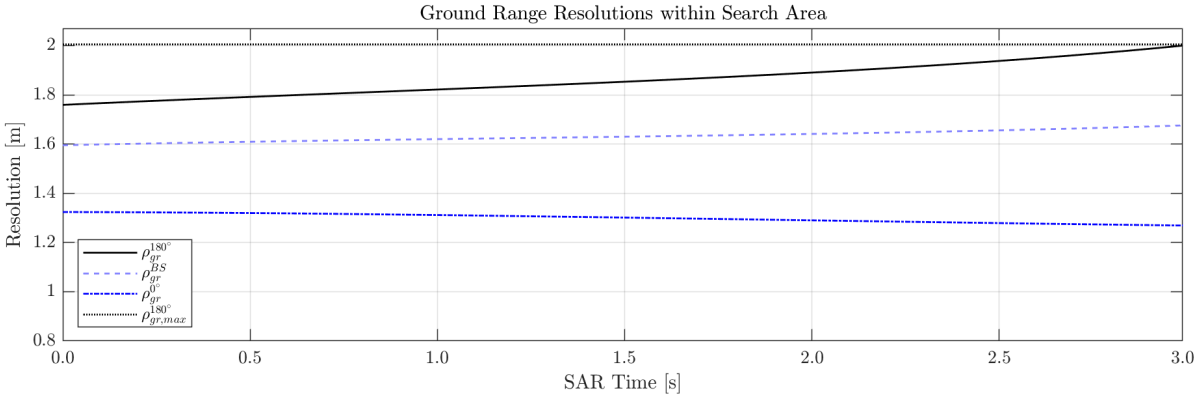

Figure 7.12: The minimum $\rho_{gr}^{180^\circ}$, maximum $\rho_{gr}^{0^\circ}$ and boresight ρ_{gr}^{BS} ground range resolutions during the SAR phase.

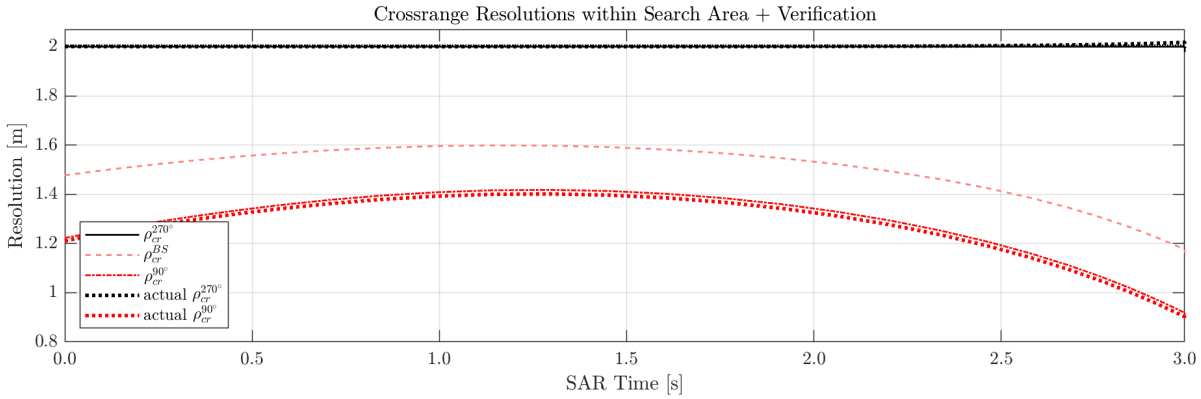

Figure 7.13: The minimum $\rho_{cr}^{90°}$, maximum $\rho_{cr}^{270°}$ and boresight ρ_{cr}^{BS} crossrange resolutions during the SAR phase + verification of the approximated best and worst crossrange resolutions within the search area by the actual analytical calculated values.

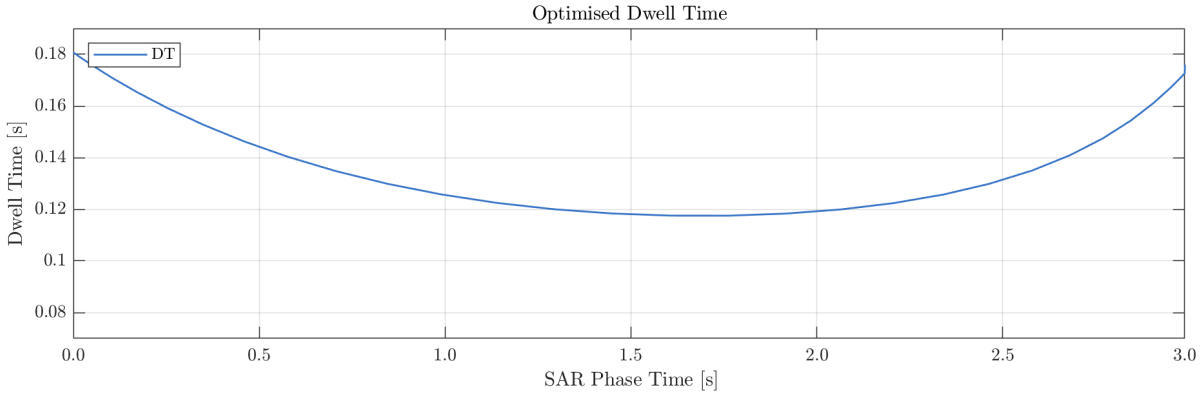

Figure 7.14: The optimised dwell time DT during the SAR phase.

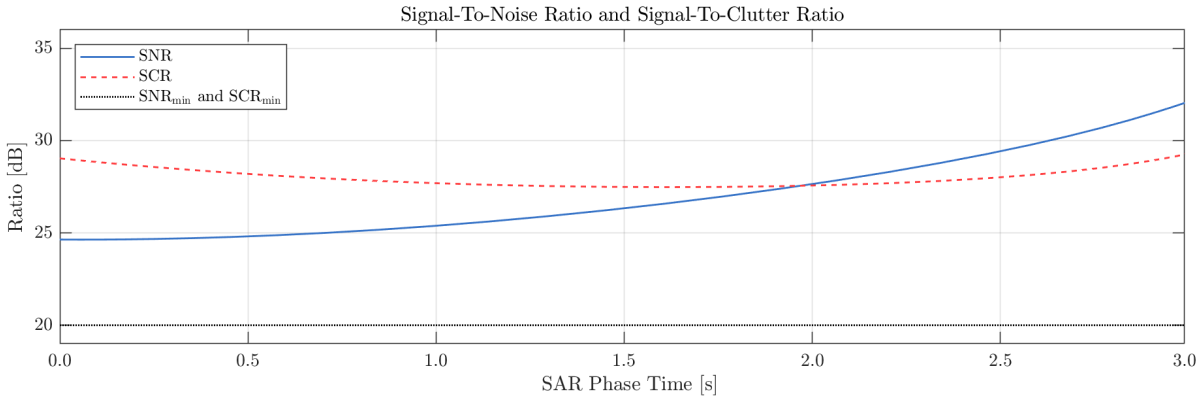

Figure 7.15: The Signal-To-Noise Ratio (SNR) and Signal-To-Clutter Ratio (SCR) during the SAR phase.

However, the locations of the worst and best crossrange resolutions were approximated because GIANT did not have the option to analytically calculate these locations, as discussed in Section 3.3.1. Therefore, these locations have been calculated after the optimisation process and used as verification for the found values as also shown in Figure 7.13 by 'actual $\rho_{cr}^{270°}$' and 'actual $\rho_{cr}^{90°}$'. According to the Figure, the approximations are similar to their actual values. The worst and best crossrange resolutions, $\rho_{cr}^{90°}$ and $\rho_{cr}^{270°}$, had an average difference of 0.17% and 1.23% compared to their actual values.

The optimised dwell time DT is shown in Figure 7.14. As mentioned before, the average dwell time is DT_{avg} = 0.1441 s. Figure 7.15 shows the SNR, SCR and their constraint of 20.00 dB. Both constraints were easily satisfied in this optimised trajectory, indicating that, for example, fainter targets with a lower RCS can be

seen. Or, parameters of the SAR seeker that are directly related to the SNR and SCR, could be decreased or increased if desired. Examples of these parameters that could be decreased are the peak power P_p, antenna gain G, pulse width τ or duty cycle d_c. Examples of parameters that could be increased are the loss factors for the range G_r and crossrange gains G_a, radar loss L_{radar} and atmospheric loss L_{atmos}, or other losses that have not been accounted for in this research.

The optimised PRF is shown in Figure 7.16. Its value equals PRF = 38734 Hz, which is greater than PRF_{min} and smaller than PRF_{max} during the entire SAR phase. Therefore, the constraint of PRF_{min} < PRF < PRF_{max} is satisfied. The PRF_{nadir} is given as additional information as explained in Section 4.5.

The SAR look angle ζ and total angle Ω between $\vec{u}_v$ and $\vec{u}_{LOS}$ are shown in Figure 7.17. During the SAR phase, the minimal and maximum value of the SAR look angle are ζ = 19.35° and ζ = 26.06° respectively. These values are well below the constraint of ζ_{max} = 45.00°, indicating that a higher horizontal seeker look angle Ξ, that improves the crossrange resolution and lowers the required dwell time, could be achieved. However, since the crossrange resolution of 2.00 m was already satisfied in this optimised trajectory, there was no need to maximise this SAR look angle. A larger SAR look angle increases the duration of the trajectory, because with a higher angle at the end of the SAR phase, the curve the missile requires to guide itself towards the target would be larger in that case. This would increase the total exposure time and lower the missile's velocity because the missile is exposed to drag forces for a longer period of time.

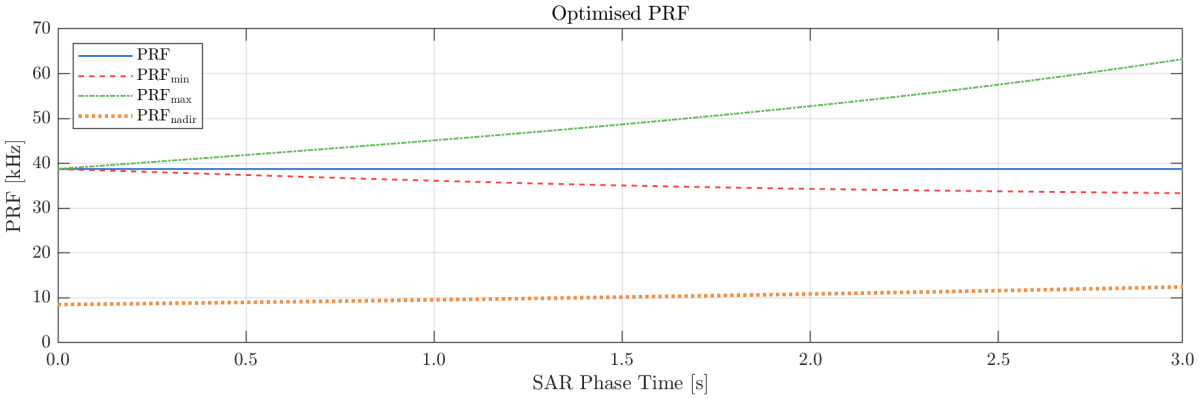

Figure 7.16: The minimum PRF, maximum PRF, and optimised PRF during the SAR phase. The $\text{PRF}_{\text{nadir}}$ is given as additional information.

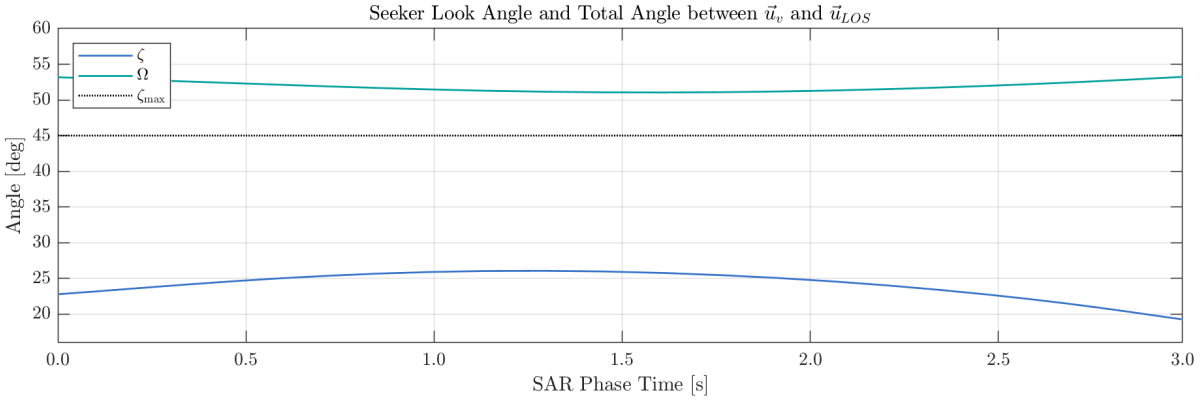

Figure 7.17: The seeker look angle ζ during the SAR phase.

7.5. Optimal Trajectory for Non-Fixed Initial Conditions

GIANT also has the ability to optimise an trajectory using non-fixed initial conditions. This will provide the optimal re-entry position and the corresponding initial Euler Angles. For this simulation, a new Pareto plot

Summary Scaling Factors		
Γ_{pqr}	Scaling factor for p, q and r	1000
$\Gamma_{V_{\text{D,end}}}$	Scaling factor for $V_{\text{D,end}}$	50
$\Gamma_{t_{\text{end}}}$	Scaling factor for t_{end}	250
Γ_{DT}	Scaling factor for DT	20000

Table 7.7: Used scaling factors used in the optimisation for non-fixed initial conditions.

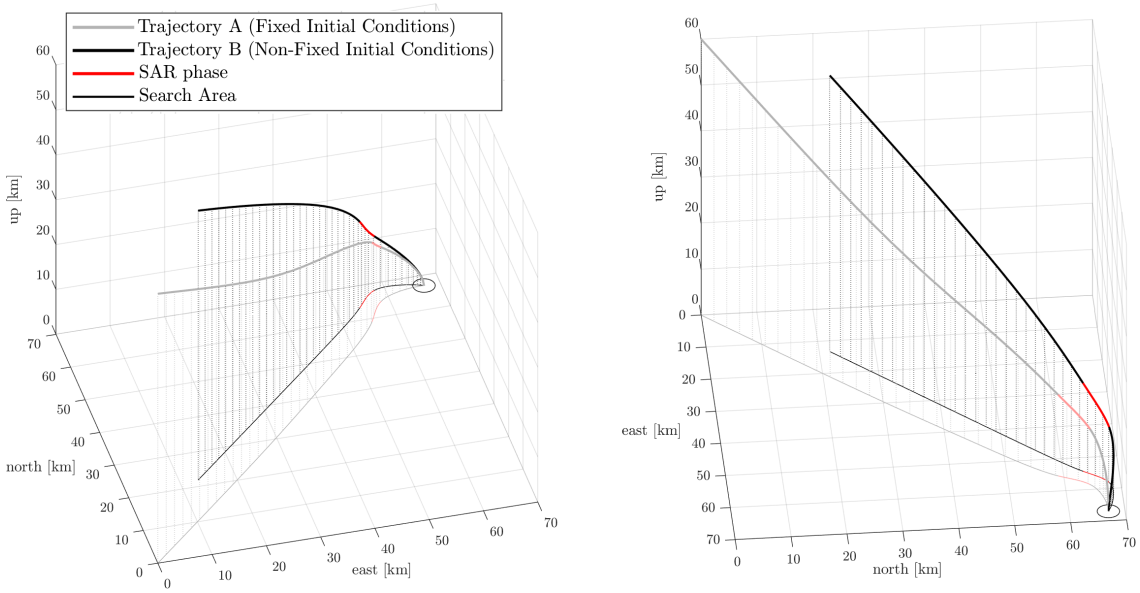

Figure 7.18: The optimised trajectory for the parameters from Tables 7.1-7.5. The ballistic trajectory as shown as reference. The SAR phase is indicated in red.

had to be generated. The found optimal scaling factors, based on the same precedence between the performance indicators, are given in Table 7.7. These scaling factors were used for the remaining of this thesis. The trajectory with the optimised initial conditions will now be compared to the trajectory of the previous Section.

Figure 7.18 shows the entire trajectory in 3D for the optimised trajectory for optimal initial conditions (trajectory B) with the trajectory for fixed initial conditions (trajectory A) as discussed in the previous Section. Compared to trajectory A, trajectory B has an initial re-entry position closer the to the target. Therefore, comparisons of the total exposure time performance between trajectory A and B can not be made. Trajectory B also shows that the missile not requires a 'pull-up' manoeuvre and has a less sharper turn to the target. However, the shape of the trajectories seem to be similar until the SAR phase.

Figure 7.19 shows the slant range R_s and missile's coordinates in the North- (x), East- (y) and Down-directions (z) for trajectories A and B. Compared to trajectory A, that has an initial slant range of R_{s0} = 112.15 km, trajectory B starts at an initial slant range of R_{s0} = 92.31 km. This corresponds to the initial x-, y- and z-coordinates of [x_0, y_0, z_0] = [21.87, 13.29, 60.00] km. Hence, the initial distance-to-go coordinates to the target are [R_{x0}, R_{y0}, R_{z0}] = [45.13, 53.71, 60.00]. Therefore, a re-entry position that is located closer, but more specifically, located more in the North-direction relative to the target, seems to be optimal.

Due to this initial re-entry position located more in the North-direction, the missile requires less manoeuvres to obtain a larger squint angle with the target at the start of the SAR phase. A larger squint angle is desired since it shortens the required dwell time to obtain the same crossrange resolution. In addition, because the initial squint angle is larger, the missile requires a less sharper turn after the SAR phase to guide itself towards

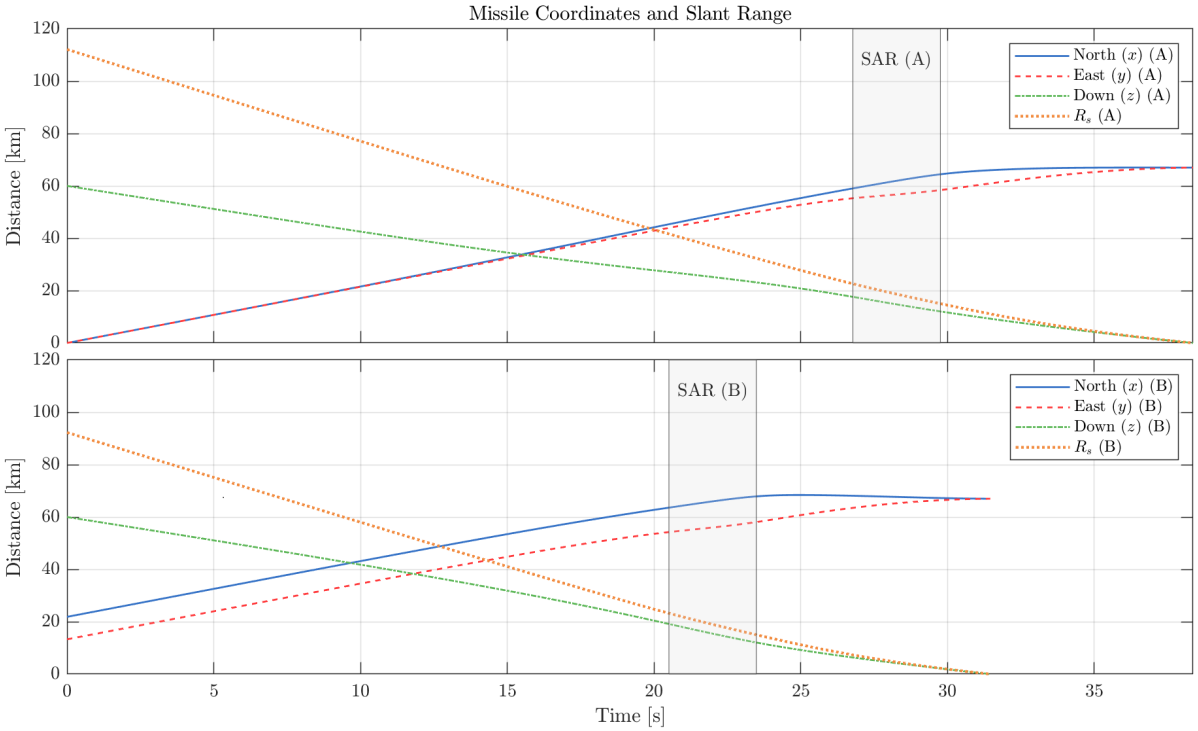

Figure 7.19: (a) The slant range R_s and distance between the missile and target in the North- (x), East- (y) and Down-directions (z) for trajectories A (fixed initial conditions) and B (optimal initial positions).

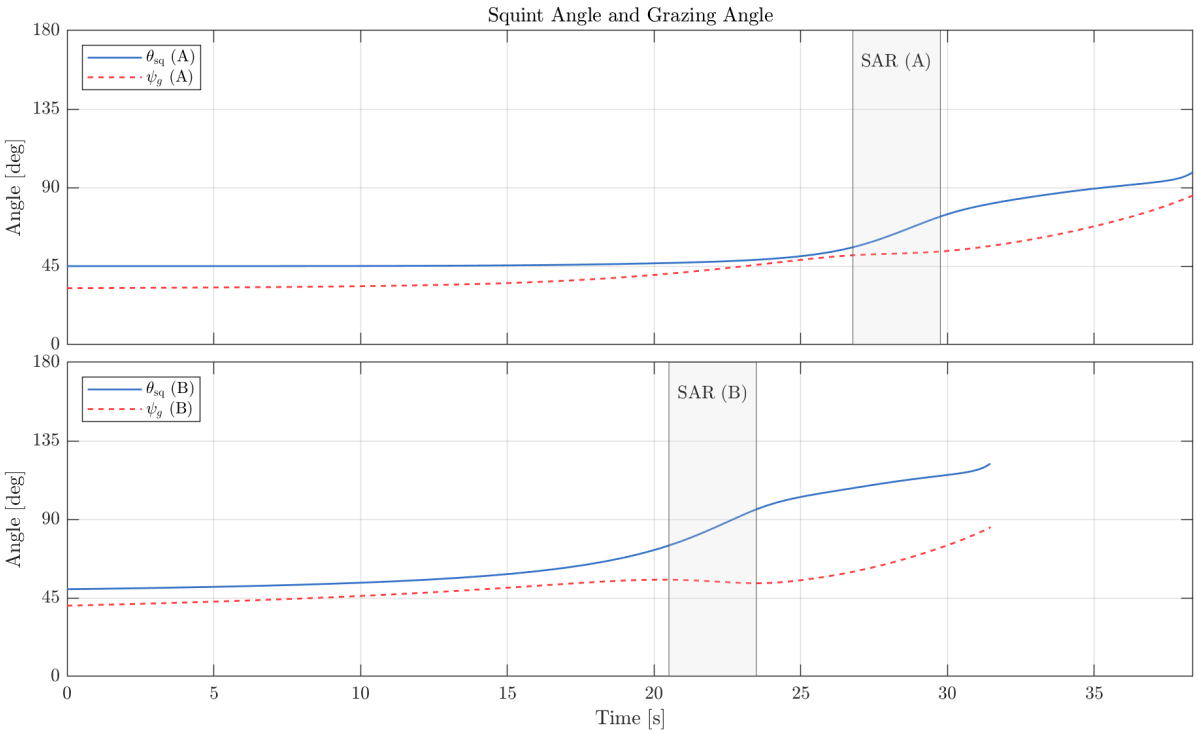

Figure 7.20: The squint angle θ_{sq} and grazing angle ψ_g for trajectories A (fixed initial conditions) and B (optimal initial positions).

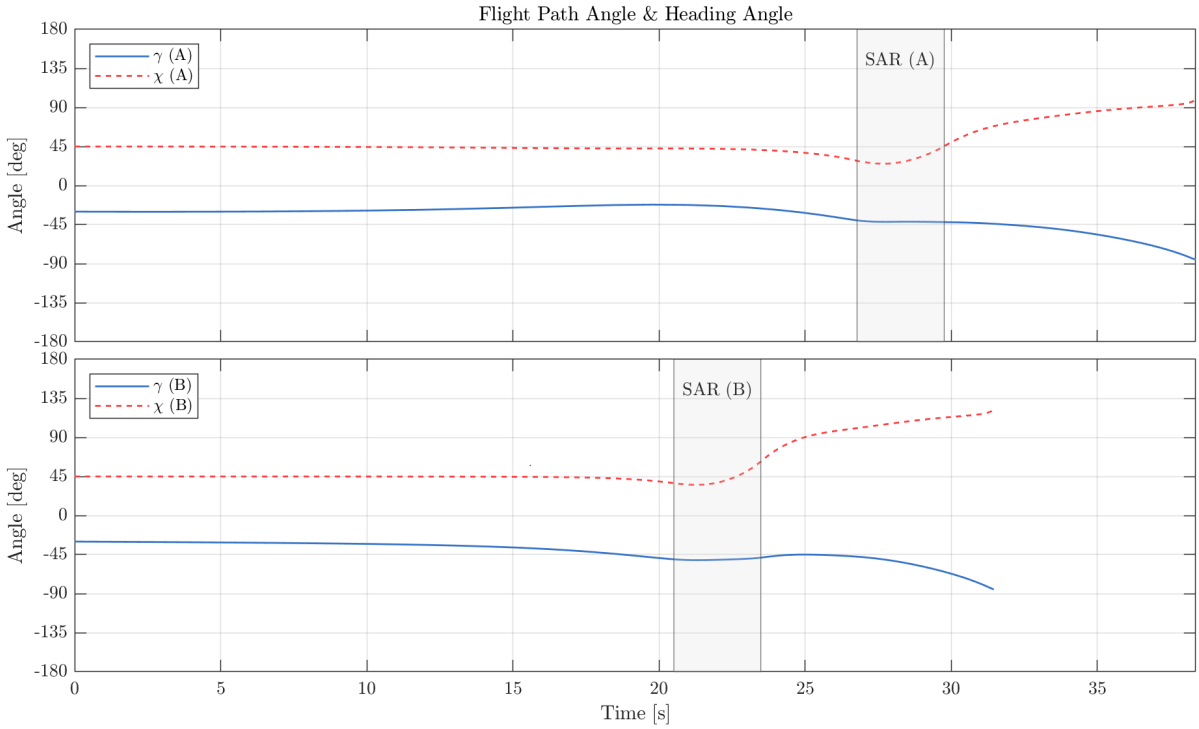

Figure 7.21: The flight path angle γ and heading angle χ for trajectories A (fixed initial conditions) and B (optimal initial positions).

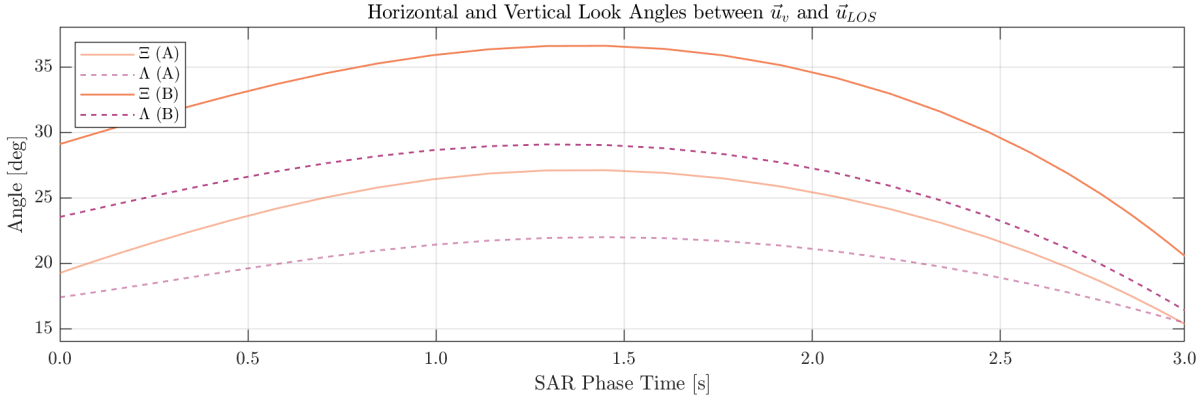

Figure 7.22: The squint angle θ_{sq} and grazing angle ψ_g for trajectories A (fixed initial conditions) and B (optimal initial positions).

the target. A comparison of the squint angles and grazing angles of trajectories A and B are shown in Figure 7.20. The initial (optimal) squint angle of trajectory B is $\theta_{sq0} = 49.96°$. While the squint angle at the start of the SAR phase is $\theta_{sq} = 74.96°$. This is significantly larger compared to trajectory A, that has a squint angle of $\theta_{sq} = 55.78°$ at the start of the SAR phase. According to the Figure, the grazing angles are similar for trajectories A and B. Since flying at higher altitudes is desired, i.e. larger grazing angles, and the ground range resolution constraint can already be satisfied at these altitudes, no major changes in the grazing angles are observed.

As shown in Figure 7.18, where trajectories A and B were compared in 3D, trajectory A showed that it had a less steeper re-entry phase compared to trajectory B. This is the result of its smaller flight path angle causing the missile to 'cruise' longer at higher altitudes before the start of the SAR phase to compensate for its re-entry position being located too far from the target. A comparison of the flight path angles γ and heading angles χ of trajectories A and B are shown in Figure 7.21. Unlike the flight path angle of trajectory A, that increases during a part of re-entry phase, the flight path angle of trajectory B gradually decreases from its initial value to $\gamma = -50.41°$ until the start of the SAR phase. The heading angle χ at the start of the SAR phase of trajectory B is $\chi = 37.33°$, while for trajectory A it is $\chi = 28.57°$. While lower heading angles are desired for improving the

dwell time performance indicator, as discussed in Section 3.3.1, the heading angle of trajectory B seems to be optimal for the overall performance of the system. Because a larger squint angle could already be achieved by a different re-entry position, a lower heading angle was not required to improve the horizontal look angle Ξ as shown in Figure 7.22. The larger vertical look angle Λ in this Figure is mainly caused by the larger flight path angle of trajectory B. However, the increase of the vertical look angle has a less impact on the dwell time performance indicator value compared to the horizontal look angle Ξ according to Equation 4.19. The final flight path angle of trajectory B has a value of γ = -85.21°, that corresponds to the impact angle of the missile.

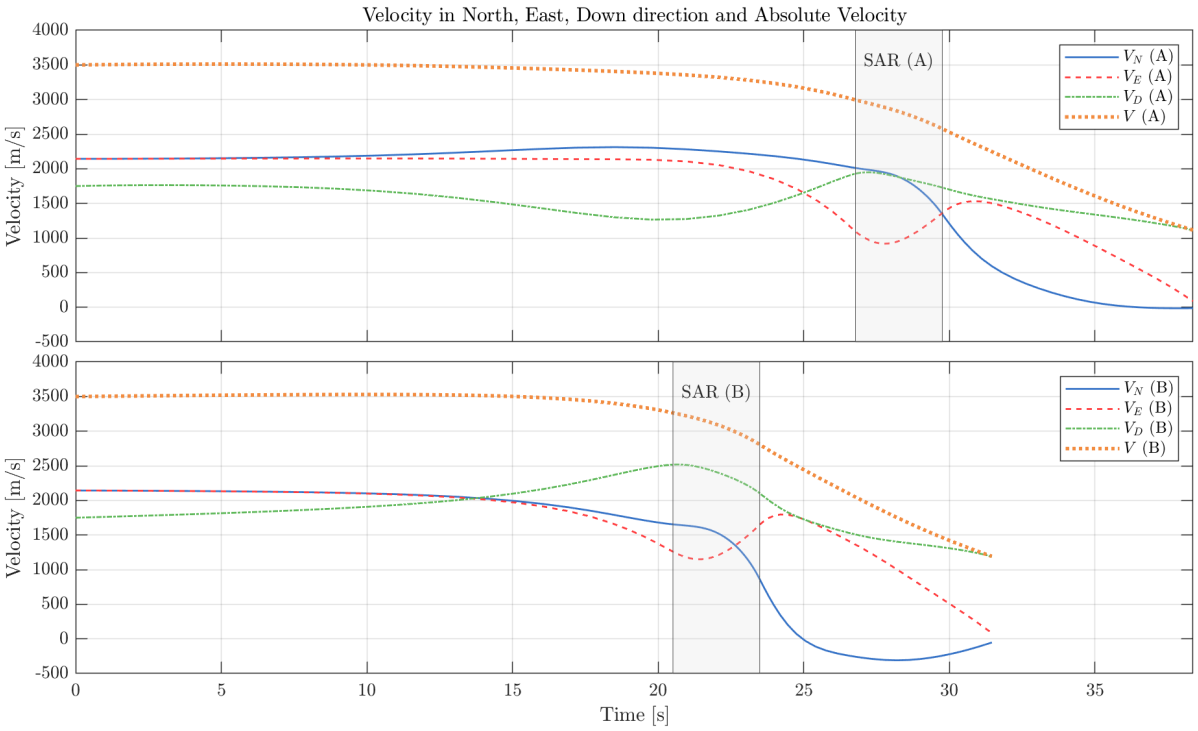

Figure 7.23: The velocities in the North- V_N, East- V_E and Down-directions V_D and absolute velocity V for trajectories A (fixed initial conditions) and B (optimal initial positions).

A comparison of velocities of trajectories A and B in the North-direction (V_N), East-direction (V_N), Down-direction (V_D) and the absolute velocity (V) are shown in Figure 7.23. Because the missile in trajectory A has a positively increasing flight path angle during its re-entry phase, the velocity in the Down-direction decreases accordingly. This is in contrast to the Down-direction velocity of trajectory B, that increases during the re-entry phase. Therefore, the absolute velocity of trajectory B at the start of the SAR phase is V = 3265.71 m/s, while the absolute velocity of trajectory A is V = 2995.32 m/s. A higher absolute velocity is desired for improving the dwell time performance indicator as discussed in Section 3.3.1. The absolute end velocity of trajectory B is V_{end} = 1192.37 m/s. With an impact angle of γ = -85.21°, the vertical end velocity is $V_{\text{D,end}}$ = 1188.21 m/s. Compared to trajectory A, that has a vertical end velocity of $V_{\text{D,end}}$ = 1110.60 m/s, this performance indicator value is also improved for the trajectory with the optimal initial conditions.

The optimised angular velocities p, q and r for trajectories A and B are shown in Figure 7.24. The graphs of the individual angular velocities are similar for trajectory A and B. These variables manoeuvre the missile to the North-direction relative to the target to obtain a larger squint angle before the SAR phase. The angular velocities of trajectory B are constant over the first 10 seconds of the re-entry phase, indicating that the initial Euler angles are optimal for this trajectory. These Euler angles, and the Euler angles of trajectory A, are shown in Figure 7.25. The found optimal initial Euler Angles for trajectory B are $[\phi_0, \theta_0, \psi_0]$ = [1.45°, -37.30°, 44.79°].

Figure 7.26 shows the angles-of-attack for trajectories A and B. The angle-of-attack for trajectory B shows less variation during the re-entry phase compared to trajectory A. This is due to its relatively constant pitch angle as shown in Figure 7.25. The shape of the graphs are similar from the start of the SAR phase until the end of the terminal guidance phase for both trajectories, explaining the similar shapes of their trajectories.

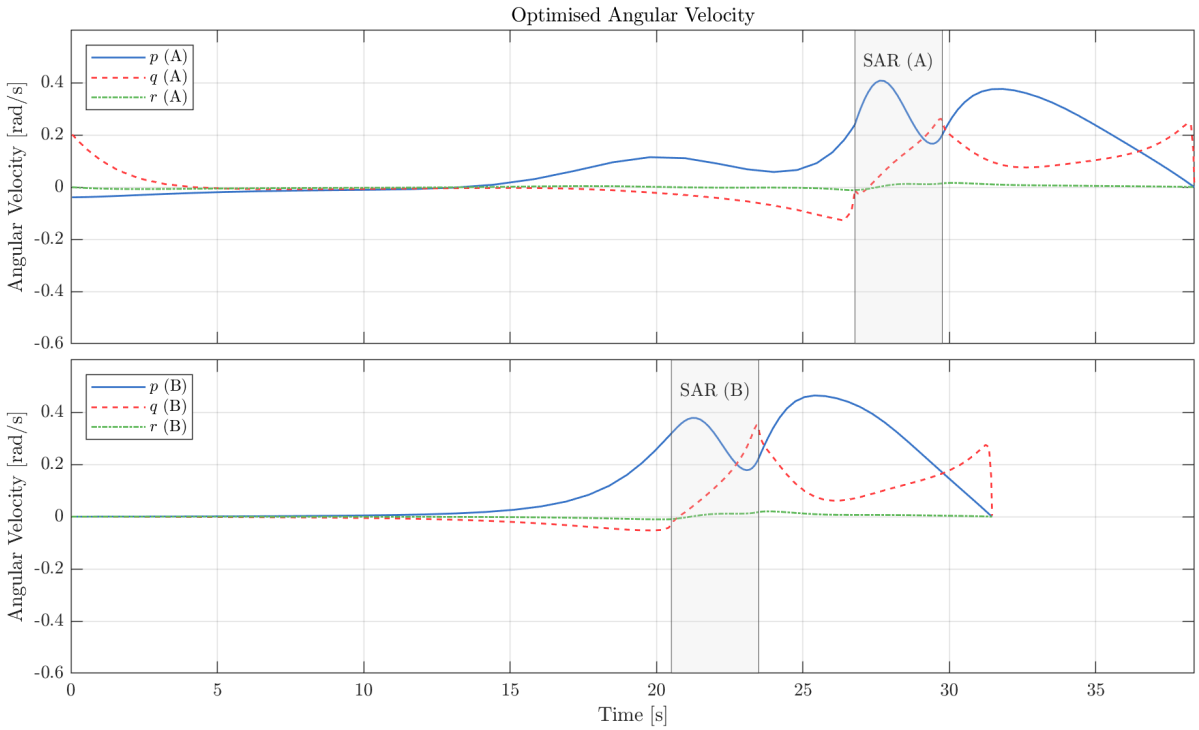

Figure 7.24: The optimised angular velocities p, q and r for trajectories A (fixed initial conditions) and B (optimal initial positions).

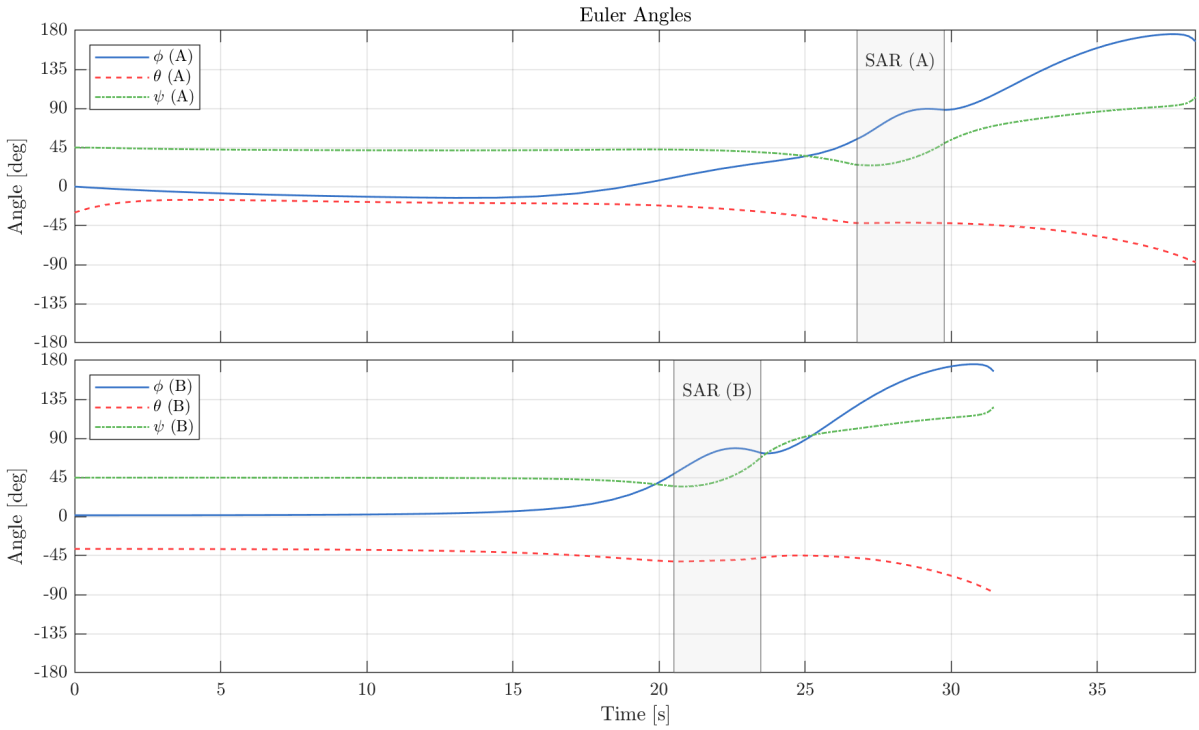

Figure 7.25: The Euler Angles ϕ, θ and ψ for trajectories A (fixed initial conditions) and B (optimal initial positions).

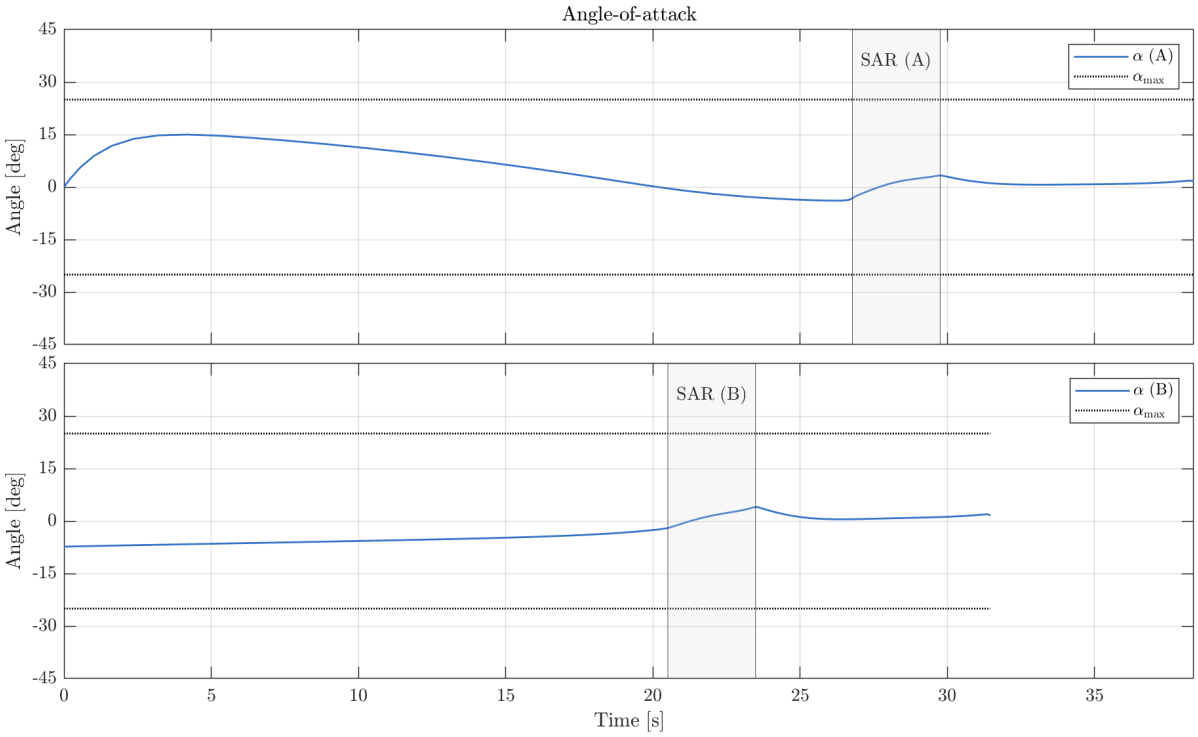

Figure 7.26: The angle-of-attack α and its constraint α_{max} for trajectories A (fixed initial conditions) and B (optimal initial positions).

Figure 7.27 shows the close-up of the SAR phase and terminal guidance phase of the trajectory B. The 0dB and -3dB beam footprints at the start of the SAR phase are also shown. In addition, the search area with the ground range and crossrange resolutions distributions are illustrated in Figure 7.27a and Figure 7.27b respectively. A close-up of these beam footprints and search areas are shown in 7.27c and 7.27d respectively.

The Figures show that the approximated worst and best ground range and crossrange resolutions for trajectory B are also at the expected locations. A comparison of the ground range resolutions of trajectories A and B are shown in Figure 7.28. The average values of the ground range resolutions of trajectory B are $\rho_{gr}^{180^\circ}$ = 1.98 m, ρ_{gr}^{BS} = 1.72 m and $\rho_{gr}^{0^\circ}$ = 1.36 m. While these average values are worse compared to trajectory A, the ground range resolution constraint of 2.00 m, everywhere in the search area, is still satisfied. These lower values are the results of the larger grazing angles as shown in Figure 7.20 before.

A comparison of the crossrange resolutions of trajectories A and B are shown in Figure 7.29. The average values of these resolutions for trajectory B are $\rho_{cr}^{270^\circ}$ = 2.00 m, ρ_{cr}^{BS} = 1.69 m and $\rho_{cr}^{90^\circ}$ = 1.60 m. Therefore, the crossrange resolution constraint of 2.00 m, everywhere in the search area, is also satisfied for trajectory B.

The optimised dwell time DT for trajectories A and B are shown in Figure 7.30. While trajectory A had an average dwell time of DT_{avg} = 0.1441 s, trajectory B optimised the average dwell time to DT_{avg} = 0.1023 s. Therefore, the optimal re-entry conditions increased this performance by approximately 29%. While the vertical look angle Λ for trajectory B is larger compared to trajectory A during the SAR phase (making the crossrange resolution worse), as shown in Figure 7.22, the lower dwell time could mainly be achieved by a combination of the higher absolute velocity V and larger horizontal look angle Ξ.

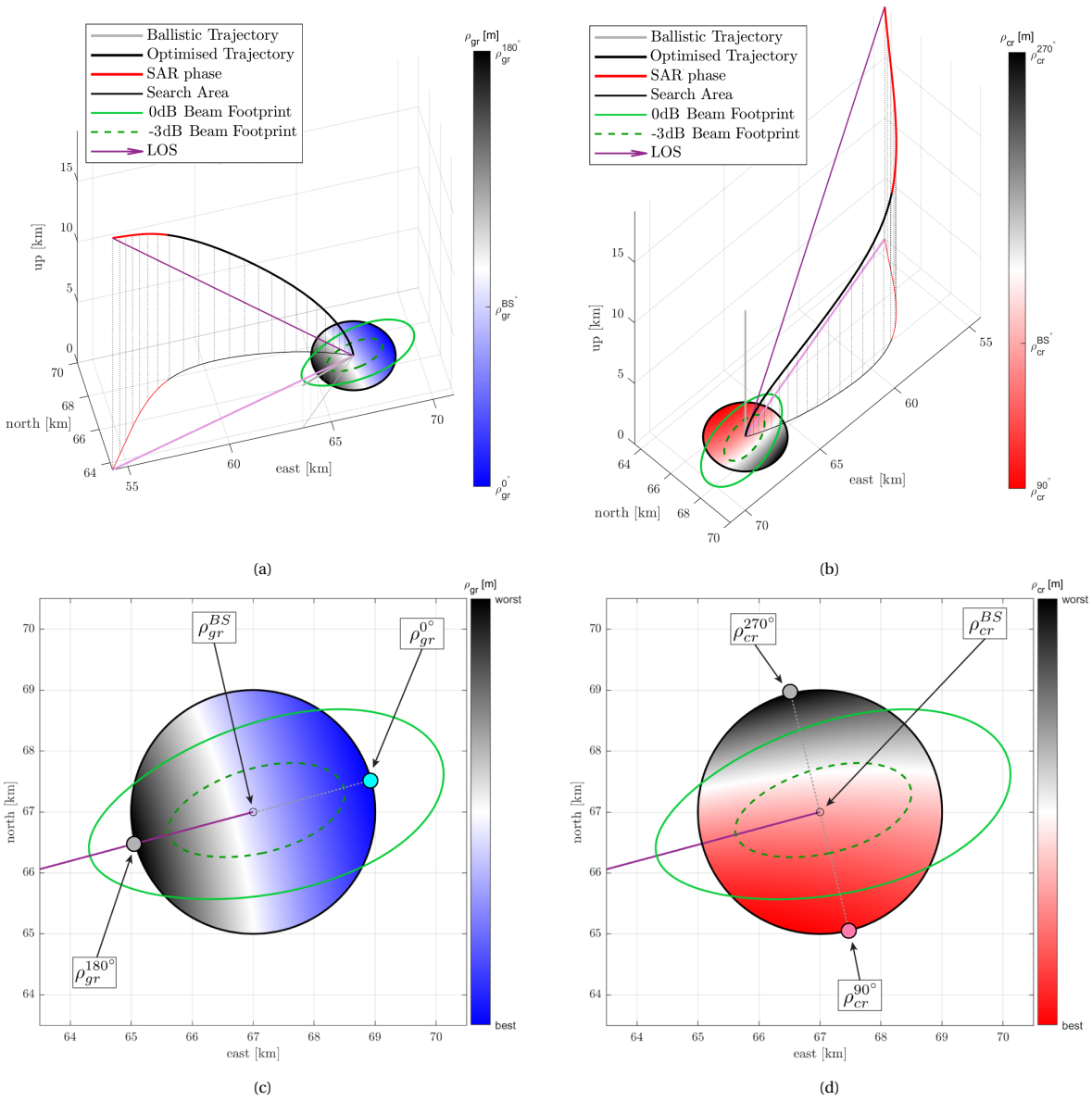

Figure 7.27: The SAR and terminal guidance phase including the beam footprints and (a) ground range and (b) crossrange resolution distributions over the search area. Close-up of the (c) ground range and (d) crossrange resolution distributions and beam footprints over the search area of trajectory B.

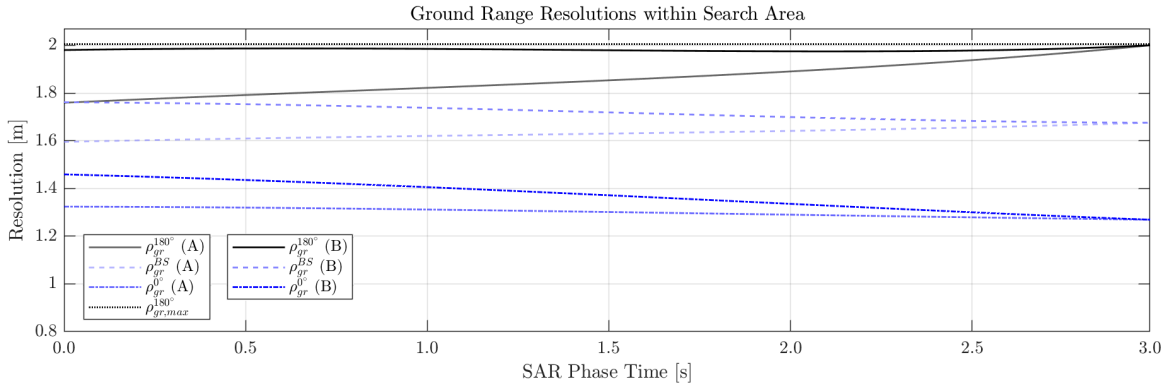

Figure 7.28: The minimum $\rho_{gr}^{0^\circ}$, maximum $\rho_{gr}^{180^\circ}$ and boresight ρ_{gr}^{BS} ground range resolution for trajectory A (fixed initial conditions) and B (optimal initial positions).

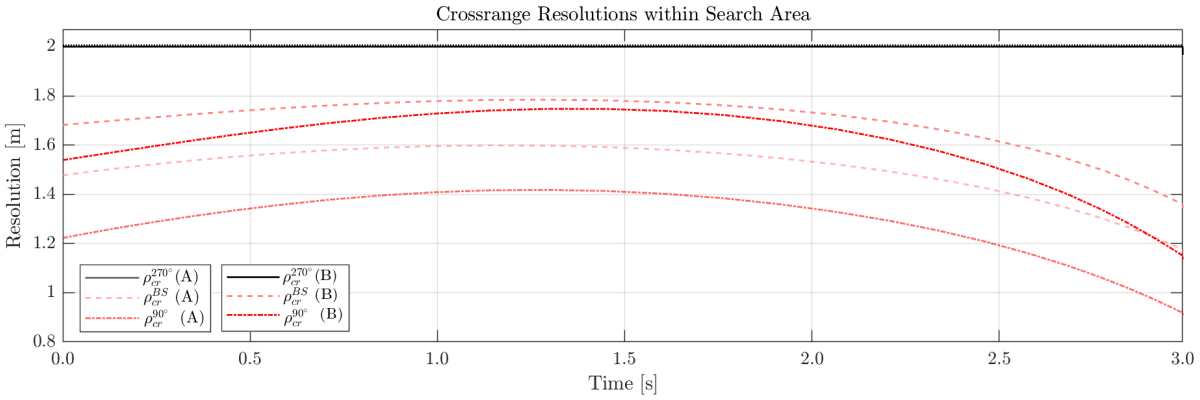

Figure 7.29: The minimum $\rho_{cr}^{90°}$, maximum $\rho_{cr}^{270°}$ and boresight ρ_{cr}^{BS} crossrange resolution for trajectories A (fixed initial conditions) and B (optimal initial positions).

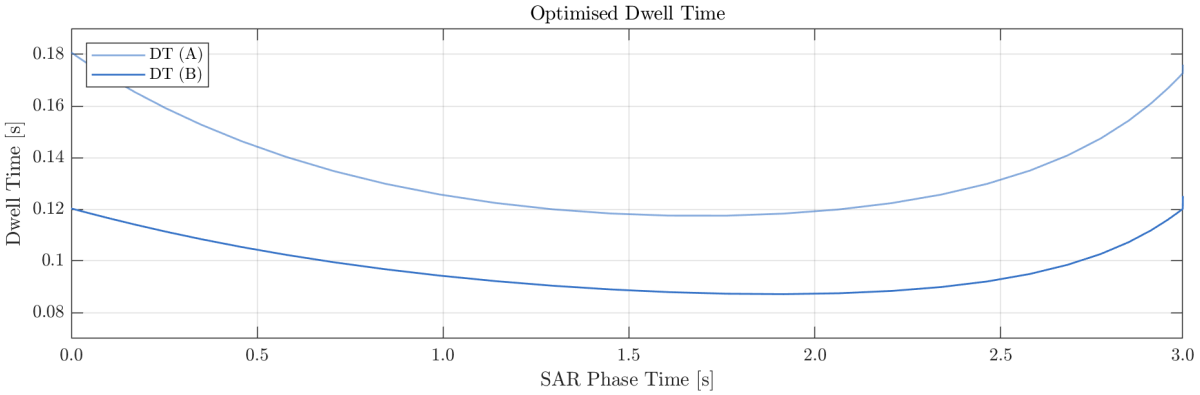

Figure 7.30: The optimised dwell time DT for trajectories A (fixed initial conditions) and B (optimal initial positions).

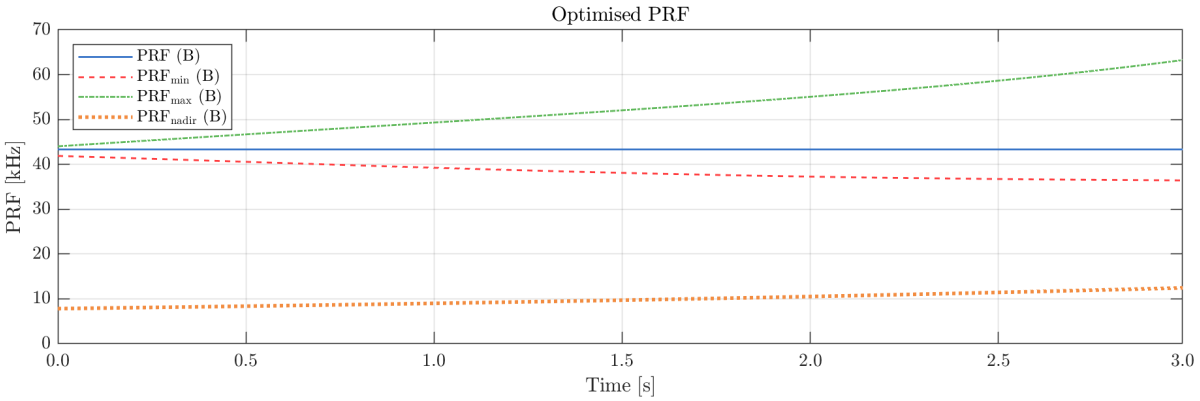

Figure 7.31: The minimum PRF, maximum PRF and optimised PRF during the SAR phase for trajectories A (fixed initial conditions) and B (optimal initial positions). The $\text{PRF}_{\text{nadir}}$ is given as additional information.

The optimised PRF of trajectory B is shown in Figure 7.31. Its value equals PRF = 43335 Hz, that also satisfy its constraints. This value is higher compared to trajectory A, that has a PRF = 38734 Hz. This is due to the greater absolute velocity V and the total angle between $\vec{u}_v$ and $\vec{u}_{LOS}$, Ω, (that increases the Doppler bandwidth B_D and thus the PRF_{min}) as shown in Figure 7.32. The seeker look angle of trajectory B shows almost no difference compared to trajectory A, indicating that about this angle, the seeker look angle is optimal for the minimisation of the dwell time without worsen the other two performance indicators.

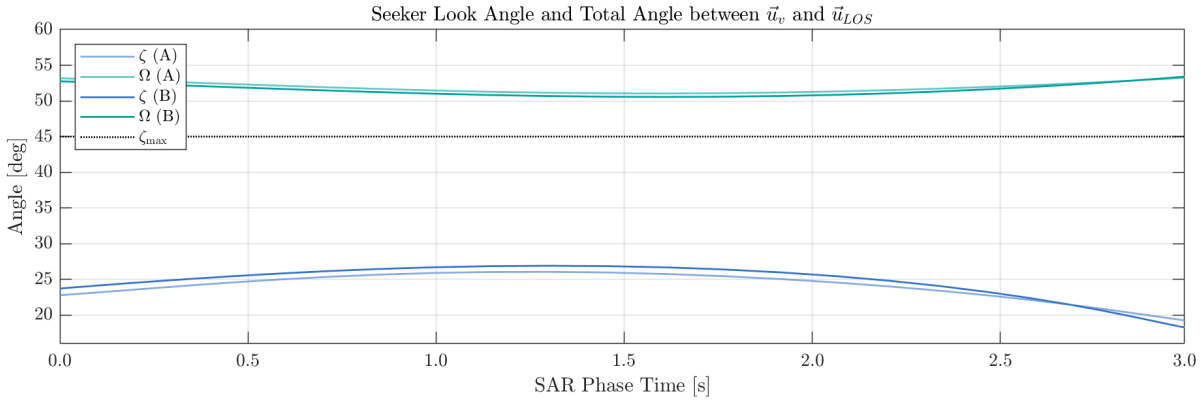

Figure 7.32: The seeker look angles ζ and the total angle between $\vec{u}_v$ and $\vec{u}_{LOS}$, Ω, for trajectories A (fixed initial conditions) and B (optimal initial positions).

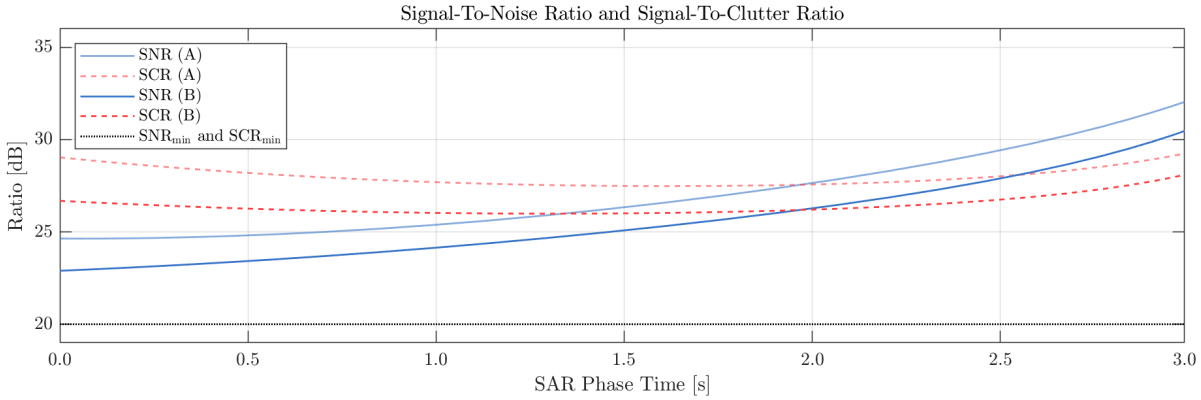

Figure 7.33: The Signal-To-Noise Ratio (SNR) and Signal-To-Clutter Ratio (SCR) for trajectory A (fixed initial conditions) and B (optimal initial positions).

Finally, Figure 7.33 shows the SNR and SCR for trajectories A and B. The obtained SNR and CNR were lower for trajectory B compared to trajectory A, while still satisfying the constraint of 20.00 dB. The lower SNR is due to a combination of the greater slant range at the start of the SAR phase and a higher absolute velocity and larger horizontal and vertical look angle at the end of the SAR phase according to Equation (4.30). The slant range at the start of the SAR phase of trajectory B is R_s = 23.29 km, while for trajectory A it is R_s = 22.63 km. Because the SNR is inversely proportional to the third power of the range, the SNR is lower for trajectory B. At the end of the SAR phase, the slant ranges for both trajectories are identical. However, the absolute velocity V, horizontal Ξ and vertical Λ look angle have greater values for trajectory B at the end of the SAR phase. A combination of these variables cause the SNR to be lower according to Equation 4.30. The lower SCR of trajectory B is due to a combination of the lower obtained dwell time and the higher normalised sea clutter RCS due to the larger grazing angles.

In summary, trajectory B with the optimal initial conditions performed better than trajectory A in terms of the performance indicators for the average dwell time DT_{avg}, exposure time t_{end} and the vertical end velocity $V_{\text{D,end}}$ as summarised in Table 7.8. However, the difference of the exposure time is mainly due to closer optimised initial position of the missile. Therefore, no conclusions about this performance improvement can be made. Also, because the initial shorter distance-to-go, the missile flies through the atmosphere for a shorter amount of time, reducing the time of the drag forces acting on the missile. As a consequence, the vertical end velocity improvement can also not be compared one to one.

The average dwell time could be improved in trajectory B because the initial re-entry position of the missile was located more to the North-direction relative to the target. As a result, the missile required less manoeuvres to increase its squint angle θ_{sq} during the the SAR phase. This larger squint angle increases the horizontal

Performance indicator values comparison

	Trajectory A	Trajectory B	Unit	Improvement
Average dwell time DT_{avg}	0.1441	0.1023	s	+29%
Exposure time t_{end}	38.37	31.46	s	+18%
Vertical end velocity $V_{\text{D,end}}$	1110.60	1188.21	m/s	+7%

Table 7.8: Performance indicator values comparison of trajectories A (fixed initial conditions) and B (optimal initial positions).

SAR phase values comparison

	Trajectory A	Trajectory B	Unit
Start/End Altitude	17.63/12.06	19.18/12.22	km
Start/End Slant Range	22.63/15.00	23.29/15.00	km
Start/End Absolute Velocity	2995.32/2575.50	3265.71/2807.71	ms^{-1}
Min./Max. SNR	24.64/31.96	22.91/30.38	dB
Min./Max. CNR	27.48/29.20	25.99/28.04	dB
Min./Max. Seeker Look Angle	19.35/26.06	18.40/26.91	deg
Optimised PRF	38734	43335	Hz

Table 7.9: Various variables during the SAR phase of trajectories A (fixed initial conditions) and B (optimal initial positions).

look angle Ξ that allows the dwell time DT to be reduced in order to obtain the same crossrange resolution ρ_{cr}. Furthermore, because of the closer initial re-entry position, the missile did not require to cruise through the atmosphere that lead to the limitation of the duration of the drag forces. Hence, the absolute velocity during the SAR phase, that also allows to reduce the required dwell time, and the vertical end velocity could be improved. A summary of various variables of trajectories A and B during the SAR phase are given in Table 7.9.

7.6. Resolution Limitation Analysis

As discussed in Section 3.3.3, the target acquisition performance can be improved for better resolutions, SNR and SCR values. Trajectory B achieved a minimum SNR and SCR of 22.91 dB and 25.99 dB respectively, while their constraints were set to 20.00 dB. The maximum ground range and crossrange resolution were both 2.00 m, while their constraints were set to 2.00 m as well. Therefore, the ground range and crossrange resolutions were the only variables limited by their constraints related to the target acquisition performance. The seeker look angle showed that it was not yet limited by its constraint, since its maximum value was $\zeta = 26.91°$ for trajectory B, while its constraint was $\zeta_{max} = 45.00°$. Larger seeker look angles indirectly allow to obtain larger the horizontal look angles Ξ that improve the obtainable crossrange resolutions. Therefore, since there is room for larger seeker look angles, a better crossrange resolution could be obtained for the set of parameters in this research. An interesting analysis would be to investigate what resolutions can be obtained for the chosen parameters until the seeker look angle is limited is reached. This will show the resolution limitations of the overall system. The ground range and crossrange resolutions constraints used for this analysis are summarised in Table 7.10, where trajectory B is identical to the one used in Section 7.5. All five trajectories will be optimised with non-fixed initial conditions to obtain the optimal trajectory.

Trajectories for the limitation analysis		
Trajectory	ρ_{gr} [m]	ρ_{cr} [m]
B	< 2.00	< 2.00
C	< 1.80	< 1.80
D	< 1.60	< 1.60
E	< 1.40	< 1.40
F	< 1.20	< 1.20

Table 7.10: Setup of trajectories with non-fixed initial conditions for different ground range and crossrange constraints values for the resolution limitation analysis. Lower resolution values equal better resolutions.

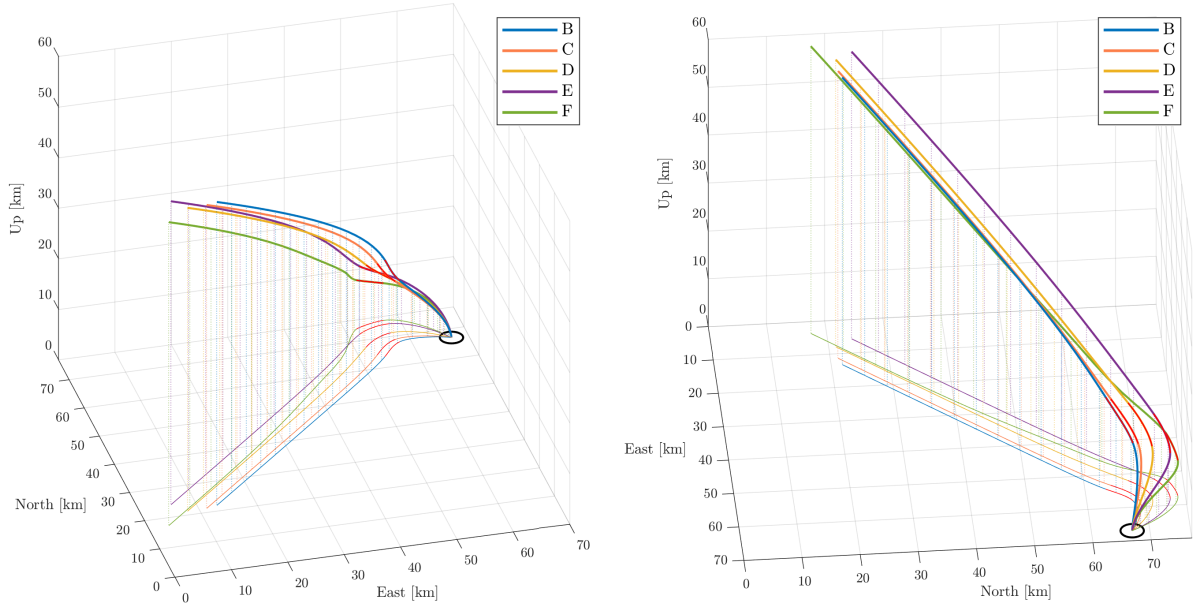

Figure 7.34: 3D view of the entire trajectories B-F from two different view angles.

Optimised Initial Position and Euler Angles		
Trajectory	Initial Position [km]	Initial Euler Angle [deg]
B	[21.87, 13.29, 60.00]	[1.45, -37.30, 44.79]
C	[21.33, 11.34, 60.00]	[3.41, -37.28, 44.50]
D	[21.24, 7.92, 60.00]	[9.89, -36.95, 43.61]
E	[24.13, 5.76, 60.00]	[7.29, -37.31, 43.92]
F	[17.31, 3.54, 60.00]	[45.29, -39.66, 34.37]

Table 7.11: The optimised initial re-entry position and Euler angles for trajectories B-F.

Figure 7.34 shows the 3D of trajectories B-F. All trajectories have different optimised initial re-entry positions and Euler angles that are summarised in Table 7.11. In general, for lower resolution constraints, the ratio between the initial position in the North-direction relative to the East-direction becomes larger, except for trajectory F. Hence, the initial squint angle at re-entry becomes larger for trajectories B to E. As discussed before, due to this larger initial squint angle, the missile requires less manoeuvres to obtain a larger squint angle with the target at the start of the SAR phase. This larger squint angle results in an increased horizontal look angle Ξ that improves the crossrange resolution.

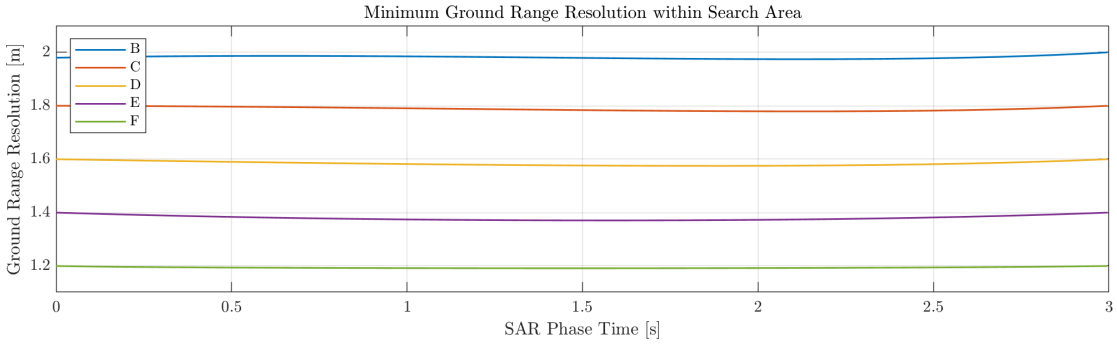

Figure 7.35: The minimum ground range resolution ρ_{gr} within the search area for trajectories B-F.

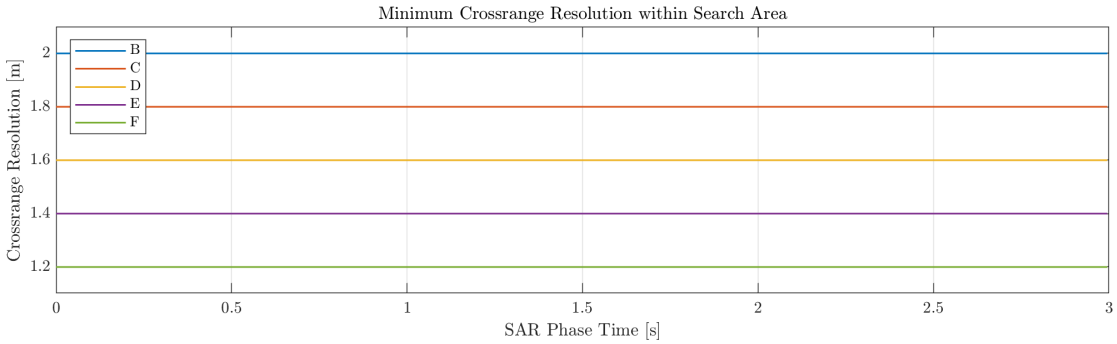

Figure 7.36: The minimum crossrange resolution ρ_{cr} within the search area for trajectories B-F.

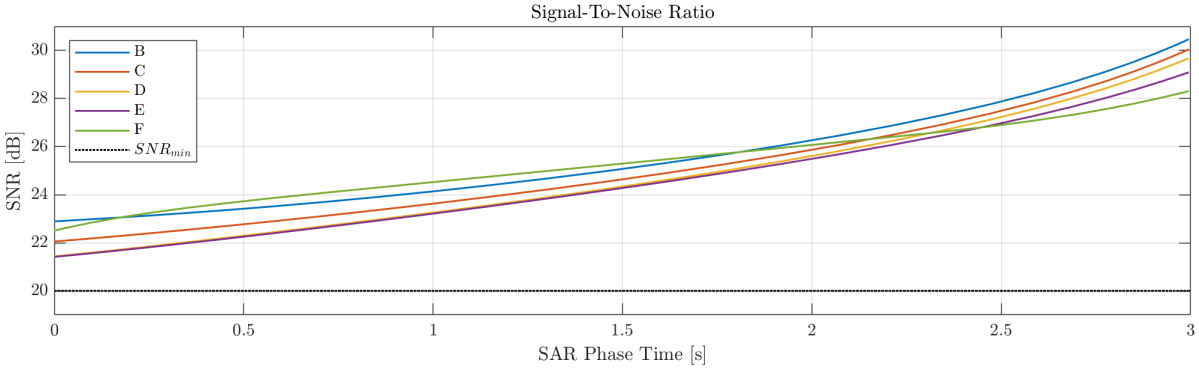

Figure 7.37: The Signal-To-Noise Ratio for trajectories B-F.

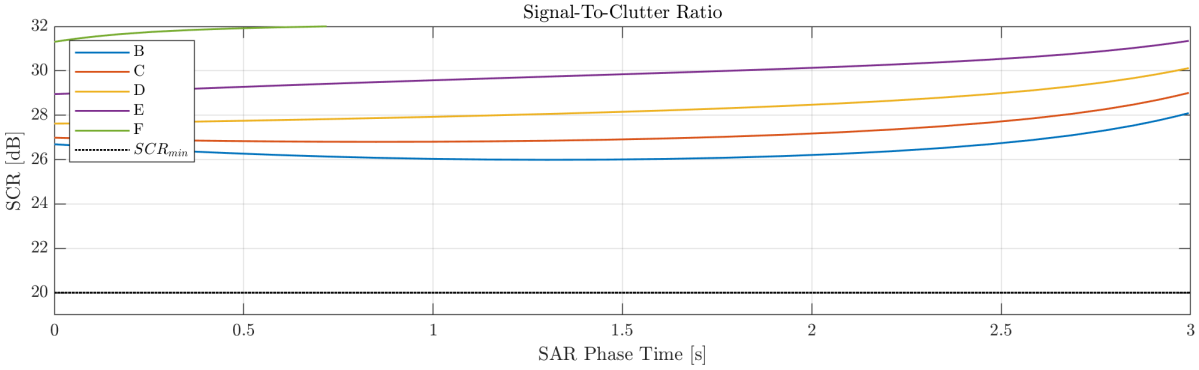

Figure 7.38: The Signal-To-Clutter Ratio for trajectories B-F.

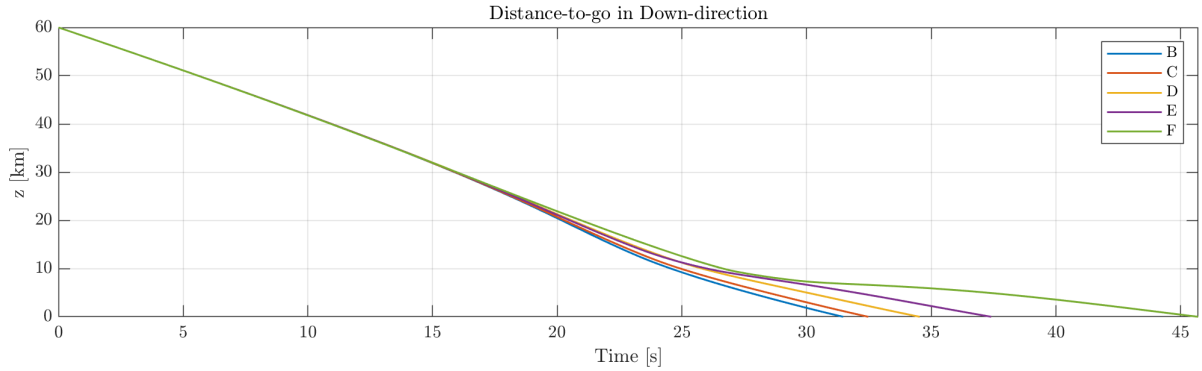

Figure 7.39: The altitude z for trajectories B-F.

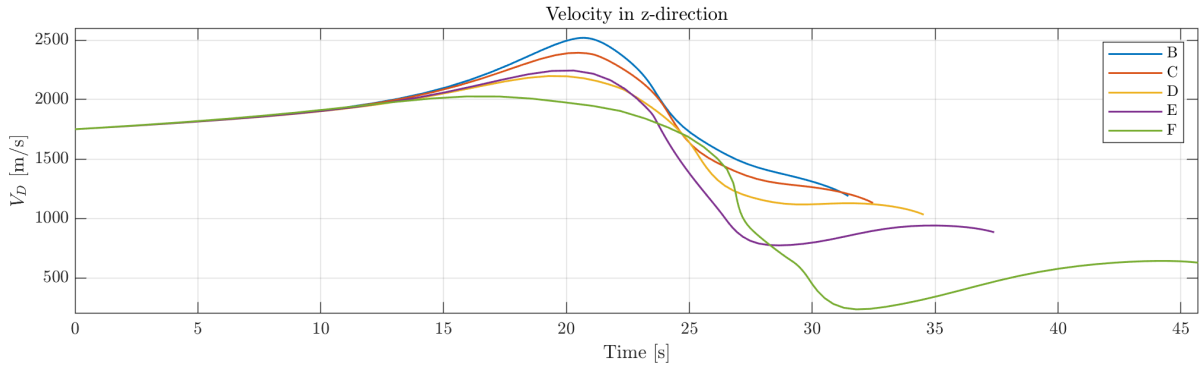

Figure 7.40: The vertical velocity V_D for trajectories B-F.

Trajectory F behaves notable different compared to the other trajectories, indicating that one of the variables is limited by its constraint. However, the constraint for ground range and crossrange resolutions are satisfied as shown in Figure 7.35 and 7.36 respectively. In addition, Figures 7.37 and 7.38 show the SNR and SCR of trajectories B-F. The graphs have similar shapes and the constraints of 20.00 dB were satisfied for all trajectories. Therefore, lowering the resolution constraints did not have major influence on the achievable SNR and SCR.

A significant difference of trajectory F compared to the other trajectories is its lower altitude z and vertical velocity V_D as shown in Figure 7.39 and 7.40 respectively. In line with lower resolution constraints (trajectories B to F), the missile flies at lower altitudes for a longer duration, that decrease its velocity due to the drag forces. Therefore, the total exposure time and its vertical end velocity performance indicators becomes worse.

Figure 7.41 shows the close-up of the SAR phases and terminal guidance phases of trajectories B-F. The seeker look angles increase for trajectories B-F as shown in Figure 7.42. The maximum seeker look angle of trajectories B-E are below the constraint of $\zeta_{max} = 45°$, while trajectory F shows that it is limited by this constraint. This would suggest the longer required dwell time of trajectory F that compensates for this limited angle for satisfying the crossrange resolution constraint. The optimised average dwell time and the other two performance indicator values for trajectories B-F are given in Table 7.12.

While the seeker look angle for trajectory F seems to be the limiting factor, this would not explain the low performance indicator values of the exposure time t_{end} and vertical end velocity $V_{\text{D,end}}$. These lower values are the result of the relatively long flight time of trajectory F at low altitudes, that drastically decrease the velocity of the missile. Due to this decreased velocity, the crossrange resolution also becomes worse according to Equation (4.19). This is compensated by a higher dwell time and larger seeker look angle, that directly is related to the horizontal look angle Ξ. A reason for the missile to fly at these low altitudes is the result of the

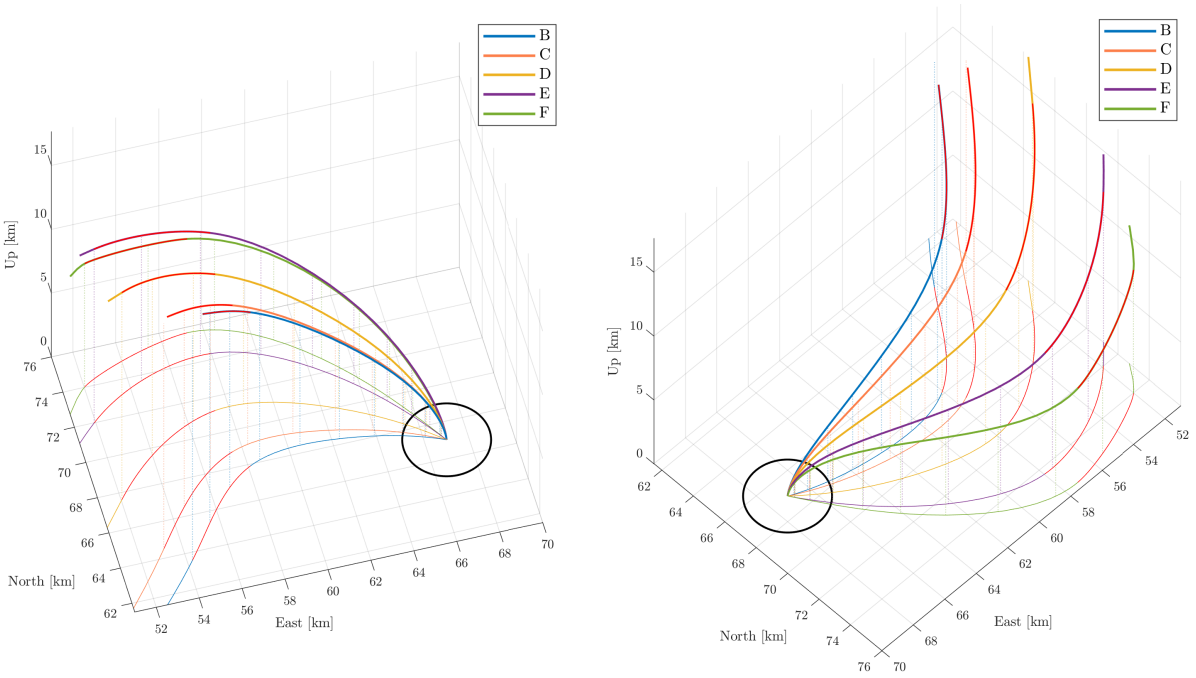

Figure 7.41: Close-up of the SAR and terminal guidance phases of trajectories B-F from two different view angles. The black circle represents the search area with r_{search} = 2.00 km.

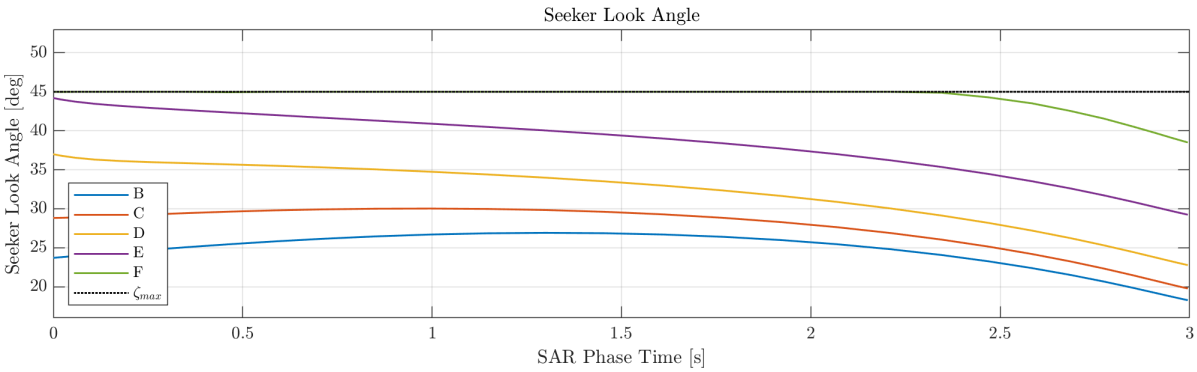

Figure 7.42: The seeker look angles ζ for trajectories B-F.

lower ground range resolution constraint. The ground range resolution only depends on the grazing angle ψ_g (which is directly related to the altitude of the missile) and the bandwidth B of the radar, according to Equation 4.14. Because the bandwidth was not changed during this analysis, it indicates that the missile is flying at lower altitudes to obtain lower grazing angles to satisfy the ground range resolution constraint.

Therefore, if the bandwidth would have been wider, the missile would not have been forced to decrease its grazing angle during its SAR phase. This would decrease the reduction of the velocity, that then again improves the exposure time and vertical end velocity performance indicators. In addition, if the velocity would be higher, a longer dwell time and maximum seeker look angle might not be required for obtaining the cross-range resolution constraint of 1.20 m, because no compensation of these values would be required. Therefore, the bandwidth of B = 150 MHz seem to be the limiting factor for obtaining resolutions below 1.20 m for the SAR seeker parameters given in Tables 7.1 and 7.2.

Summary Resolution Limitation Analysis

Trajectory	ρ_{gr} [m]	ρ_{cr} [m]	DT_{avg} [s]	$V_{\text{D,end}}$ [ms^{-1}]	t_{end} [s]	PRF [Hz]
B	2.00	2.00	0.1023	1188.20	31.46	43335
C	1.80	1.80	0.1075	1129.34	32.47	39586
D	1.60	1.60	0.1170	1031.51	34.53	34467
E	1.40	1.40	0.1319	882.97	37.40	28627
F	1.20	1.20	0.1685	627.28	45.70	20937

Table 7.12: Summary of the performance indicators of trajectory B-F.

8

Conclusion and Recommendations

In this chapter, the conclusions based on the results are given in Section 8.1. In Section 8.2, the recommendations for future research are given.

8.1. Conclusion

The main research question is answered by answering the four research sub-questions:

1. What are the requirements for the acquisition of a maritime surface target?

   As discussed in Chapter 3, the resolution, Signal-To-Noise Ratio (SNR), Signal-To-Clutter Ratio (SCR) and search area were used for the acquisition a maritime surface target. The ground range resolution was used to distinguish points in the ground range direction, while the crossrange resolution was used to distinguish points in the crossrange direction. A minimum SNR was used to ensure that the power of the target's reflected energy was sufficiently high enough to distinguish it from the background noise. Whereas a minimum SCR was used to overcome the reflected signals originating from the sea surrounding the target. Furthermore, a search area was used to take into account any unexpected movements of the target during the time of the last provided coordinates of the target and the start of the acquisition phase. Within the search area, all of the above requirements had to be satisfied. The size and shape of this area depends on the characteristics and manoeuvrability of the target.

2. How can these requirements be obtained by a SAR seeker?

   As discussed in Section 4.3.1, the ground range resolution can be obtained by transmitting a signal and measuring the period between the reflected signals. Because the signals travel at a constant speed through the atmosphere, the range between the radar and a point target can be calculated. For obtaining fine ground resolutions, SAR systems generally use pulse compression modulation techniques. The most commonly used type of modulation is the Linear Frequency Modulation (LFM), that applies a linear increase or decrease to the frequency of the transmitted signal. By using this type of modulation, wider bandwidths can be transmitted while maintaining the original uncompressed pulse width. The ground range resolution also depends on the grazing angle of the incoming signal, where lower grazing angle improve this resolution. To obtain lower grazing angles, the SAR seeker has to be positioned at lower altitudes. However, at these lower altitudes, the density of the atmosphere is higher that increases the drag forces acting on the missile. Because higher drag forces slow down the missile and a higher velocity is desired, lower altitudes during the acquisition phase should be avoided.

The crossrange resolution can be obtained by measuring the Doppler shifts of the incoming signals. These Doppler shifts can be transformed to the an actual resolution in the crossrange direction. As discussed in Section 4.3.2, this resolution is proportional to the wavelength of the transmitted signal and the range between the missile and target, while being inversely proportional to the velocity of the missile and the dwell time. In addition, the crossrange resolution also depends on the horizontal and vertical look angles between the velocity vector and Line-Of-Sight vector. The best crossrange resolution can be obtained for a horizontal and vertical look angle of 90° and 0° respectively. However, the SAR seeker look angle, i.e. the angle between the antenna and the longitudinal axis of the missile's body, was limited by a constraint to avoid the antenna to operate behind its physical limit.

The SNR can be obtained by coherently integrating the pulses during the CPI. The SNR depends on various parameters and variables as shown in Section 4.4.1. Its value is mainly determined by the range between the SAR seeker and target, because the SNR is inversely proportional to the third power of this range. Therefore, to obtain higher SNR values, it is desired to minimise this range. However, this range could be minimised down to a certain limit, because the acquisition phase has to be completed before the terminal guidance phase. As discussed in Section 4.4.2, the SCR can be obtained by dividing the power of the received signals from the target by the power received by from clutter. In this research, it was assumed that the clutter only originated from the sea surface and is not coherently integrated during the CPI. Therefore, this value is proportional to the squared root of the dwell time and Pulse Repetition Frequency. However, the Pulse Repetition Frequency is bounded to an upper and lower limit to avoid ambiguities in range and Doppler.

3. How is the performance of the SAR seeker on an ASBM defined?

   The minimisation of the dwell time was used to describe the performance of the SAR seeker, as discussed in Chapter 4. The minimisation of the exposure time (t_{end}) and the maximisation of the vertical end velocity ($V_{D,end}$) were used to describe the performance of the ASBM. All of these performances described the overall system performance. While the actual motion of a target was not taken into account in this research, the minimisation of the DT was chosen as performance indicator because in real-world applications, moving targets become defocused in the SAR images. To limit this amount of defocus, a lower dwell time is desired. The exposure time was chosen as performance indicator since shorter times would reduce the chances of the missile being intercepted by anti-missile defense systems. The vertical end velocity $V_{D,end}$ variable relates to the effectiveness of the ASBM on the target and therefore was required to be as high as possible.

4. How can this performance be improved?

   As discussed in Chapter 7, the overall performance of the system could be improved for an optimal initial re-entry position that has a larger squint angle relative to the target. This larger squint angle allowed to missile to obtain a larger seeker look angle during the SAR phase by performing minimal manoeuvres before and after this phase. The larger seeker look angle reduced the required dwell time to obtain the constraint of the crossrange resolution. In addition, due to these limited manoeuvres, the exposure time and the duration of the missile flying through lower atmospheric layers could be minimised as well. This latter reduced the duration of the drag forces acting on the missile that limited the velocity reduction of the missile. Hence, the vertical end velocity could also be improved.

   The resolution limitation analysis in Section 7.6 showed that a ground range and crossrange resolution of 1.60 m could be achieved for DT_{avg} = 0.1170 s for the chosen SAR seeker parameters and the other constraints in this research. All of the performance indicators drastically decreased for a resolution

constraints below 1.40 m. The analysis showed that a wider bandwidth is required for obtaining better resolution performance for the current system.

8.2. Recommendations

A lot of simplifications and assumptions were being made as provided in Section 7.1. Therefore, the model does not entirely match real world applications. Assumptions related to environmental circumstances have to be investigated in future research since these could influence the performance. Examples are the influences of the curvature, rotation and non-constant gravitational acceleration of the Earth. In addition, it was assumed that a target did not induce an additional Doppler shift on its reflected signals. However, in real world applications, targets do have a motion that cause the reflected signals to be Doppler shifted. These effects can have an influence on the localisation of maritime surface targets, and so, the precision of the guidance system in order to let the missile hit the target.

The characteristics and properties of the CFAV Quest were used in this research. However, military maritime surface targets usually have higher speeds, meaning that the search area size should be increased. The search area was assumed to be circle shaped with its center at the last known coordinates of the target. However, the shape of the search area depends on the characteristics and manoeuvrability of the target. For example, if the heading direction of the target is known, the constraints have not be satisfied in the area behind the target. This shape could influence the trajectory of the ASBM. Furthermore, the Radar-Cross-Section (RCS) signature of military maritime surface targets are different compared to the CFAV Quest, because this value depends on many different characteristics. This RCS signature is generally highly classified, which explains the choice of using the CFAV Quest for this thesis. Future research should investigate what RCS signatures can represent actual maritime surface targets and how this would influence the trajectory of an ASBM.

The side lobes of the radar antenna were not taken into account. However, in real world applications, signals measured by these lobes could interfere with the reflected signals of a target. Future research should investigate if post-processing algorithms or other techniques exists to avoid these unwanted reflected signals. Or that the signals from the sidelobes have to be taken into account for this type of application of SAR. In addition, a study should be conducted that investigate any other radar antenna losses that were not taken into account in this thesis.

While the resolution constraints could be satisfied within the search area during the SAR phase, the -3dB beam footprint did not completely overlay the search area. Therefore, in order to illuminate targets outside the -3dB beam footprint, the antenna needs to 'scan' to completely map the search area. This would require additional time during the acquisition phase. Future research should investigate how this influences the overall performance of the system.

The locations of the best and worst crossrange resolutions within the search area where approximated as discussed in Chapter 3.3.1, because no analytical equations for these locations exist. To improve the certainty and accuracy for the obtainable crossrange resolution and their corresponding locations, the 'min()' and 'max()' functions should be implemented in GIANT.

The results indicate that the bandwidth of the radar is the limiting factor for obtaining a higher ground range and crossrange resolutions. The influence of a wider bandwidth on the overall performance should be investigated. In addition, the seeker look angle of the trajectory with a resolution constraint of 1.20 x 1.20 m also appeared to be a limiting factor. Therefore, the influence of a larger maximum seeker look angle constraint

should be investigated as well. Another recommendation for future research is to investigate how other parameters could improve the cost function, this could be achieved by a sensitivity analysis. However, a realistic or optimal fixed initial conditions have to be determined first, in order to compare the results of such analysis.

In the resolution limitation analysis, the ground range and crossrange resolution constrains were decreased at the same time. While this would ensure the resolution cells in the SAR image not to be stretched out in one of these directions, the performance could not be investigated for individual adjustments to these resolution constraint. Therefore, future research should decrease these resolution constraints individually to investigate what parameters of the radar are limiting the best obtainable ground range or crossrange resolution. Furthermore, the scaling factors for trajectory B (that had the resolution constraint of 2.00 m) were used for all the other trajectories during the analysis. Therefore, the performance of these trajectories may not represent their optimal trajectory for the performance indicators having the same precedence. To achieve this, future research should generate new Pareto plots before every new simulation run.

The scaling factors were based on the point closest to the interception of the asymptotes in the Pareto plot. This was done by assuming that the average dwell time, exposure time and vertical end vertical velocity had the same precedence. However, it should be investigated what performance indicator is preferred by an engineer. In addition, a study should be carried out to determine what performance indicator values are feasible and not feasible. This would generate the optimal trajectory for a certain scenario.

The start of the homing phase was set to a range of 15.00 km from the center of the search area. However, this range depends on the size of the search area and the manoeuvrability of the missile. Future research should investigate the relation between the size of the search area, the manoeuvrability of the missile and therefore the minimum initial range of the terminal guidance phase. These results may show that the range of 15.00 km used in this research was reasonable or not reasonable. This would greatly influence the results, because the crossrange resolution, SNR and SCR all dependent on the range between the radar and target.

Lastly, the time for the acquisition phase was set to 3.00 s. This value was based on a combination of found literature values, the possibility that the identification algorithm requires more than one SAR image, the required time to process the received data, the required time to generate one SAR image and the possibility that the search area could not be mapped by the beam footprint at one instant. Future research should investigate what acquisition phase time should be used to represent real-world scenarios for this type of application.

Bibliography

[1] Warren C.E. Nethercote. The CFAV QUEST's Lewex Experience. *John Hopkins APL Technical Digest*, Vol. 11(No. 3 and 4), 1990.

[2] Gregers-Hansen Vilhelm and R. Mital. An improved empirical model for radar sea clutter reflectivity. *IEEE Transactions on Aerospace and Electronic Systems*, Vol. 48(No. 4):pages 3512–3524, 2012.

[3] Allied Naval Engineering Publication. *Standardized Wave and Wind Environments and Shipboard Reporting of Sea Conditions*, number No. 1. NATO STANAG 4194, April 1983. NATO Unclassified.

[4] M. D. Ortiz. *Remote Sensing Of Open Water Fraction And Melt Ponds In The Beaufort Sea Using Machine Learning Algorithms*. PhD thesis, University Of Miami, Florida, USA, August 2017.

[5] MetaSensing Radar Solution. MetaSensing delivers hourly high-resolution X-band airborne SAR images over Rotterdam - available: `https://www.metasensing-group.com/single-post/2020/02/17/metasensing-delivers-hourly-high-resolution-x-band-airborne-sar-images-over-rotterdam`. Online, 2020.

[6] Ji-Wei Zhu, Xiao-Lan Qiu, Zong-Xu Pan, Yue-Ting Zhang, and Bin Lei. An improved shape contexts based ship classification in SAR images. *Remote Sensing*, Vol. 9:page 145, 2017.

[7] M. Mackey. Tugfax - available: `http://tugfaxblogspotcom.blogspot.com/20101101archive.html`. Online, June 2013.

[8] Z.X. Pan Y.T. Zhang B. Lei. J. W. Zhu, X. L. Qiu. An improved shape contexts based ship classification in sar images. *Remote Sensing, 9:145*, Februaryruary 2017.

[9] P. Berens. Introduction to Synthetic Aperture Radar (SAR). Technical report, Research Institute for High-Frequency Physics and Radar Techniques, Germany, 2003.

[10] Eugene L. Fleeman. *Technologies for Future Precision Strike Missile Systems*. North Atlantic Treaty Organization, July 2001.

[11] S. Chandrashekar, R.N. Ganesh, C.R. Raghunath, Rajaram Nagappa, N. Ramni, and Lalitha Sundaresan. *China's Anti-Ship Ballistic Missile Game Changer In The Pacific Ocean*. National Institute of Advanced Studies, November 2011.

[12] Andrew S. Erickson. Chinese Anti-Ship Ballistic Missile Development and Counter-intervention Efforts, February 2017.

[13] National Oceanic and Atmospheric administration, Washington, D.C. *US Standard Atmosphere*, October 1976.

[14] Jacco Hoekstra Junzi Sun and Joost Ellerbroek. Estimating aircraft drag polar using open flight surveillance data and a stochastic total energy model. *Transportation Research Part C Emerging Technologies*, May 2020.

[15] Angelo Miele. *Flight Mechanics - Theory of Flight Paths*, volume 1. Addison-Wesley Publishing Company, Inc., 1962.

[16] D.M. Henderson. Shuttle Program. Euler angles, quaternions, and transformation matrices working relationships. *Technical Memorandum*, July 1977.

[17] Ozgyr Ekinci. *Adaption of a Control System to Varying Missile Configurations*. PhD thesis, Middle East Technical University, December 2009.

[18] M. Bergsma. Nonlinear Trajectory Optimization. *TNO Report 2018 R11113*, 2020.

[19] Tonje Hannevik, Richard Olsen, and Paris Vachon. Polarisation-dependent signatures of ships in envisat ap mode data. January 2004.

[20] David Vaitekunas and W. Davis. Validation of ShipIR (v3.2): methodology and results. pages 17–21, May 2006.

[21] Chen Liu, Lloyd Gallop, and Dave Schlingmeier. QUEST-2003 Polarimetric Signature Trial: Experiment Design, SAR Calibration, Data Acquisition and Initial Results. page 55, November 2004.

[22] Bassem R. Mahafza. *Radar Systems Analysis and Design Using MATLAB*. Chapman and Hall/CRC, 3rd edition.

[23] K. Sun, B. Wen, and R. Wang. Analysis of Ship RCS Detected by Multifrequency HFGWR. *International Journal of Antennas and Propagation*, page 5, 2017.

[24] Zhao Hongzhong, Xie Huaying, and FU Qiang. Azimuth Resolution Acquisition through Trajectory Optimization for a SAR seeker. In *2nd Asian-Pacific Conference on Synthetic Aperture Radar*, pages 55–59, 2009.

[25] Jamal Saeedi and Karim Faez. Synthetic Aperture Radar Imaging using Nonlinear Frequency Modulation Signal. *IEEE Transactions on Aerospace and Electronic Systems*, Vol. 52:pages 99–110, April 2016.

[26] A. Farooq and D. Limebeer. Trajectory optimization for air-to-surface missiles with imaging radars. *Journal of Guidance, Control and Dynamics*, Vol. 25(No. 5), September 2002.

[27] Merrill I. Skolnik. *Radar Handbook*. McGraw-Hill, 2nd edition, 1990.

[28] Domenico Schiavulli, Antonio Sorrentino, and Maurizio Migliaccio. A discussion on the use of X-band SAR images in marine applications. *Atti Della "Fondazione Giorgio Ronchi"*, Vol. 58:pages 601–610, 01 2014.

[29] *Attenuation by atmospheric gases - P Series, Radiowave Propagation*. International Telecommunications Union, September 2016.

[30] Pavithra Nagaraj. Impact of atmospheric impairments on mm wave based outdoor communication. Technical report, Cornell University, June 2018.

[31] Tomoki Kaneko Toshihiro Obata Shinichi Nakasuka Jiro Hirokawa Seiko Shirasaka Hiromi Watanabe Kei-Ichi Hirako Koichi Ijichi Hirobumi Saito, Budhaditya Pyne. Engineering-Model Results of X-band Synthetic Aperture Radar for Small Satellite and Its Application to Constellation Mission. In *32th Annual AIAA/USU Conference on Small Satellites*, 2018.

[32] C. Özdemir. *Inverse Synthetic Aperture Radar Imaging with MATLAB Algorithms*. John Wiley and Sons, Inc., 2012.

[33] Mohamed Mmdouh Ashry, Ahmed S. Mashaly, and Bassem Ibrahim Sheta. Comparative Analysis between SAR Pulse Compression Techniques. In *2020 12th International Conference on Electrical Engineering (ICEENG)*, pages 234–240, 2020.

[34] J.R. Apel and C.R. Jackson. *Synthetic Aperture Radar marine user's manual.* NOAA Environmental Data and Information Service, USA, 2004.

[35] Armin W. Doerry. Performance Limits for Synthetic Aperture Radar - 2nd edition. Technical report, Sandia National Laboratories, 2006.

[36] Peter Hoogeboom, Ad Stoffelen, and Paco Lopez-Dekker. Dopsca, scatterometer-based simultaneous ocean vector current and wind estimation. In *Doppler Oceanography from Space (DOfS)*, pages 1–9, 2018.

[37] Divya Garg. Advances in global pseudospectral methods for optimal controls. 2011.

[38] J. Nocedal and S. Wright. *Numerical Optimization.* Springer, 2nd edition, 2008.

[39] D. Ridzal. *Trust Region SQP Methods With Inexact Linear System Solves For Large-Scale Optimization.* PhD thesis, Rice University, Houston, USA, 2006.

[40] M.T. Crockett. *Target Motion Estimation Techniques for Single-Channel SAR.* PhD thesis, Brigham Young University, Provo, 2014.

[41] S. Hinz, F. Meyer, A. Laika, and R. Bamler. Spaceborne Traffic Monitoring with Dual Channel Synthetic Aperture Radar Theory and Experiments. In *2005 IEEE Computer Society Conference on Computer Vision and Pattern Recognition (CVPR'05) - Workshops*, page 7, 2005.